2016

Self-Assembly of DNA-Coated Particles: Experiment, Simulation and Theory

Minseok Song
Lehigh University

Self-Assembly of DNA-Coated Particles:

Experiment, Simulation and Theory

by

Minseok Song

Presented to the Graduate and Research Committee

of Lehigh University

in Candidacy for the Degree of

Doctor of Philosophy

in

Chemical Engineering

Lehigh University

May, 2016

Certificate of Approval

Approved and recommended for acceptance as a dissertation in partial fulfillment of the requirements of the degree of Doctor of Philosophy.

_____
Date

_____
Jeetain Mittal, Ph.D.
Dissertation Co-Advisor

_____
Mark A. Snyder, Ph.D.
Dissertation Co-Advisor

_____
Accepted Date

Committee Members:

_____
Jeetain Mittal, Ph.D.
Committee Co-Chair

_____
Mark A. Snyder, Ph.D.
Committee Co-Chair

_____
Anand Jagota, Ph.D.
Committee Member

_____
H. Daniel Ou-Yang, Ph.D.
Committee Member

_____
Xuanhong Cheng, Ph.D.
Committee Member

Acknowledgements

I am deeply grateful to my advisor, Prof. Jeetain Mittal and Prof. Mark A. Snyder. Without their patient guidance, discussion, encouragement, and support, my research work would not have been possible. I would like to take this opportunity to thank my committee members, Prof. Anand Jagota, Prof H. Daniel Ou-Yang, and Prof. Xuanhong Cheng, for their insightful discussion and guidance in my research work.

I owe my gratitude to all my colleagues in my groups. Particularly, I shall thank Shih-Chieh Kung for discussion of my experiments. It was another pleasure to talk with you about industrial experience and further career. I am grateful to Yajun Ding for talking the theoretical and experimental knowledge with me in my research. Also, I shall thank Daniel Gregory for his witty talks and supportive discussion, Midhun Joy for his thoughtful suggestion and inspiration, Gül Zerze for her sincere helps and discussion and Hasan Zerze for supporting my research work.

I am very fortunate to have several friends in Lehigh. Hyunho, lots of talks with you made me motivated and dynamic in my Lehigh life. Yuna, thanks for your guidance for my daughters and good luck to your ongoing projects. Dr. Yeun Chul Park: Thanks for your helpful discussion to see new aspects. I am very grateful to Prof. Changwoon Nah for his sincere advice in my research and life. En Hyung Chang: Good luck to your research. Vicky: You are the first and best consultant for my family, thank you very much.

Finally, I really appreciate to my wife, Hye Kyung Lee, for her patient support in my life, and my lovely daughters, Seoyun Song and Chloe A. Song. Furthermore, I would like to convey my gratitude for my parents, Keehyun Song and Kwonja Hah, for their endless supports and everything that can’t put into words.

Table of Contents

List of Tables

List of Figures

Abstract

The bottom-up assembly of material architectures with tunable complexity, function, composition, and structure is a long sought goal in rational materials design. One promising approach aims to harnesses the programmability and specificity of DNA hybridization in order to direct the assembly of oligonucleotide-functionalized nano- and micro-particles by tailoring, in part, interparticle interactions. DNA-programmable assembly into three-dimensionally ordered structures has attracted extensive research interest owing to emergent applications in photonics, plasmonics and catalysis and potentially many other areas. Progress on the rational design of DNA-mediated interactions to create useful two-dimensional structures (e.g., structured films), on the other hand, has been rather slow. In this thesis, we establish strategies to engineer a diversity of 2D crystalline arrangements by designing and exploiting DNA-programmable interparticle interactions. We employ a combination of simulation, theory and experiments to predict and confirm accessibility of 2D structural diversity in an effort to establish a rational approach to 2D DNA-mediated particle assembly.

We start with the experimental realization of 2D DNA-mediated assembly by decorating micron-sized silica particles with covalently attached single-stranded DNA through a two-step reaction. Subsequently, we elucidate sensitivity and ultimate controllability of DNA-mediated assembly—specifically the melting transition from dispersed singlet particles to aggregated or assembled structures—through control of the concentration of commonly employed nonionic surfactants. We relate the observed tunability to an apparent coupling with the critical micelle temperature in these systems.

Also, both square and hexagonal 2D ordered particle arrangements are shown to evolve from disordered aggregates under appropriate annealing conditions defined based upon pre-established melting profiles.

Subsequently, the controlled mixing of complementary ssDNA functionality on individual particles ('multi-flavoring') as opposed to functionalization of particles with the same type of ssDNA ('uni-flavoring') is explored as a possible design handle for tuning interparticle interactions and, thereby, accessing diverse structures. We employ a combination of simulations, theory, and experimental validation toward establishing 'multi-flavoring' as a rational design strategy. Firstly, MD simulations are carried out using effective pair potentials to describe interparticle interactions that are representative of different degrees of ssDNA 'multi-flavoring'. These simulations reveal the template-free assembly of a diversity of 2D crystal polymorphs that is apparently tunable by controlling the relative attractive strengths between like and unlike functionalized particles. The resulting phase diagrams predict conditions (i.e., strengths of relative interparticle interactions) for obtaining crystalline phases with lattice symmetries ranging among square, alternating string hexagonal, random hexagonal, rhombic, honeycomb, and even kagome.

Finally, these model findings are translated to experiments, in which binary microparticles are decorated with a tailored mixture of two different complementary ssDNA strands as a straight-forward means to realize tunable particle interactions. Guided by simple statistical mechanics and the detailed MD simulations, 'multi-flavoring' and control of solution phase particle stoichiometry resulted in experimental realization of structurally diverse 2D microparticle assemblies consistent with predictions, such as square, pentagonal and hexagonal lattices (honeycomb, kagome). The combined simulation, theory,

and experimental findings reveal how control of interparticle interactions via DNA-functionalized particle "multi-flavoring" can lead to an even wider range of accessible colloidal crystal structures. The 2D experiments coupled with the model predictions may be used to provide new fundamental insight into nano- or microparticle assembly in three dimensions.

Chapter 1:

Introduction

1.1 Colloidal Self-Assembly

The thesis at hand deals with the study of two-dimensional colloidal assembly with specific and temperature-dependent interactions. This pertains to the field of physics known as *soft matter*, which is synonymous with "complex fluids" and "colloids" (*1*). Soft matter systems consist of particles, which can range in size between several nm to μm, suspended in molecular solvent. Colloidal particles undergo Brownian motion in progress towards the lowest free energy state (*2*). Due to their accessible time and length scales, colloidal dispersions are a simple model system to study fundamental processes in nature such as first-order transitions that are unparalleled in molecular systems (*3*, *4*). Furthermore, the formation of crystals with precise particle arrangements and periodic structures using these colloidal particles is of interest for developing novel materials such as photonics, sensors, catalytic supports, scaffold structures and lightweight structural materials that form by self-assembly (*5*, *6*).

Self-assembly, which refers to the process by which discrete components spontaneously organize into ordered structures, takes place at all scales from atoms and molecules up to meso- and macroscopic objects (*7*). Colloidal crystallization using nanoparticles or microparticles is one common representation of self-assembly beyond molecules. Colloidal crystallization is driven by various interactions such as van der Waals, repulsive, depletion and attractive electrostatic interactions. For hard sphere models where

interparticle potential is infinitely repulsive at contact but zero elsewhere, their spontaneous crystallization is mostly driven by entropy (or free volume) maximization, which results in limited selection of attainable closed packed crystalline phases: mostly the face-centered cubic (fcc) or hexagonal close-packed (hcp) structures (*8*).

More complexity of crystalline phases can be achieved by simultaneous assembly of particles of different particle type, particle shape, and particle size in the hard sphere models. Depending on the size ratio, the binary mixing of hard spheres leads to three types of crystal phases: AB, AB_2 and AB_{13} (*9*), for instance. In addition to entropy-driven crystals of hard spheres, depletion forces (*10*) can drive the self-assembly of colloids even in absence of any attractive potentials. This depletion interaction is driven by entropy in binary systems with two differently sized particles, which can be tuned by varying the size and concentration of the small particles. The incorporation of attractive interactions also leads to more diverse crystal phases such as body-centered cubic (bcc), fcc and other exotic crystals (*11*, *12*). However, these assembly mechanisms rely on colloidal stabilization aimed at avoiding aggregation and flocculation. Furthermore, these are dependent largely on particle chemistry and appear challenging to control.

One route to achieving complex, functional and integrated architectures similar to those that have been observed in Nature, such as protein synthesis within the living cell (*13*), is the exploitation of rational synthesis and design of functionalized colloidal particles as building blocks for assembly driven by rather weak and specific interaction forces (*14*). Yet, predictive "programming" of the correct interactions into constituent self-assembling particles in order to achieve specific macroscopic assemblies has proven quite challenging (*15*). In this sense, biomolecules such as proteins and nucleic acids offer attractive and

specific programmable assembly. By tethering these moieties to the surface of particles, intrinsic biomolecular recognition can be used to drive assembly of colloidal particles in order to construct complex, functional and integrated architectures (*16–18*). Specifically, nucleic acids have been widely shown to be quite beneficial for directed self-assembly, as prominent directionality between complementary DNA base pairs known as Watson-Crick paring (between Adenine-Tymine (A-T) and Guanine-Cytosine (G-C)) (*19*) permits endless combinations of tunable, reversible and orthogonal interactions.

1.2 DNA-coated Particles

Deoxyribonucleic acid (DNA) has been adopted as remarkable building blocks for self-assembly in nature as well as material science. In nature, DNA carries and stores life's genetic code as an informational component driving function in all known living organisms. Directed by Watson-Crick base pairing rules, the translation of information is determined by the complementary nature of based-paired structures through hydrogen bonding, π-stacking, electrostatic and hydrophobic interactions (*20*).

In material science, DNA holds great promise as a functional material that is capable of directing the assembly of materials into many complex, functional and integrated architectures. The reversible and sequence-specific binding of DNA has been exploited to construct direct assembly of structural motifs by DNA itself and crystalline structures by particle-based systems (*21*). 'DNA nanotechnology' has been used extensively in the creation of dynamic nanostructures such as DNA machines (*22*), walkers (*23*), a nanoscale assembly line (*24*), and complex hybridization-based amplification or reaction networks (*25*). On the other hands, despite the initial promise of utilizing DNA-based particle assembly for the new self-assembly frontier (*26*), very little has been done in terms of DNA-mediated assembly to actually extend the promise of creating complex tunable structures. In fact, the very initial goal of creating diamond-like crystal symmetry for photonic applications has not been realized with even gold nanoparticles.

1.2.1 Overview of DNA-coated Particles

Generally, in cases of DNA-mediated particle assembly, the DNA tethered to the particle surface is typically composed of three parts (**Figure 1.1**), 'a binding group' that is used to connect DNA with particles (e.g., thiol group, amine and avidin-biotin, etc.), a

complementary ‘sticky end’ that is an active single stranded DNA (ssDNA), and an ‘inert’ ‘spacer’ sequence that is used to separate this ‘sticky end’ from the particle surface in order to facilitate the interaction/hybridization of complementary ‘sticky ends’ on different particles. DNA-mediated assembly can either be initiated by the addition of a third free ssDNA linker (3 strand system, **Figure 1.1-right**) or particles can be coated with partially complementary ssDNA directly (2 strand system, **Figure 1.1-left**). While it has yet to be established which of these systems favor crystallization, the current paradigm for DNA-mediated particle assembly uses the 2-stranded system since the 3-stranded linker system could be kinetically unfavorable due to the two-step reaction required for the linker to hybridize with ssDNA on two different particles. Assembly in the 3-stranded linker system also complicates comparison between theoretical predictions and experimental results (*27*).

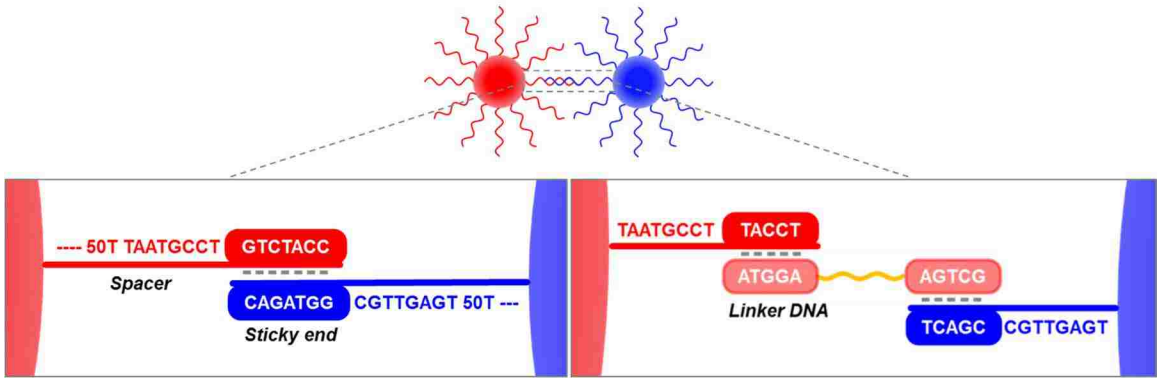

Figure 1.1. Schematic representations of DNA-coated particles system: 2 strand system (left) and 3 strand system (right).

Several factors can have influence on DNA-mediated interactions and assembly: (a) factors related to the DNA molecules such as DNA strand length, sequence, rigidity, and single-stranded spacer vs double-stranded spacer; (b) factors related to the colloidal particles such as grafting density, particle size, grafting topology; (c) factors related to the

assembly conditions such as temperature, pH, and ionic strength; and (d) factors related to the applied external potential and particle-surface interactions. These are discussed in the context of the literature below.

DNA spacers have been shown to have direct influence on the coverage of oligonucleotides and hybridization due to the secondary interaction between the particles and the spacer (*28–30*). The coverage of oligonucleotides with poly(T) spacers exhibit significantly higher surface density than oligonucleotides with poly(A) spacers due to the weaker affinity of the former to the surface of the particles (*31*). Also, the melting temperature shows a linear dependence on the length of the spacer. Importantly, with respect to the formation of the crystal structures, Nykypanchuk *et al*.(*32*) showed that for DNA-functionalized nanoparticles, the longest flexible spacers produced spontaneous crystalline formation with long-range order, but the shorter or more rigid spacers led to amorphous structures. Very recently, additional research maintains that a flexible spacer is more desirable to induce crystallization in nanoparticles (*33*) as well as microparticles (*34*).

Various studies show that DNA-mediated interactions can be controlled in terms of their range and magnitude. Valignat *et al*. showed that increasing length of block copolymer adsorbed onto the particle surface (in that case) reduces the number of effective linkages.(*35*) Also, Leunissen *et al*.(*36*) reported that palindromic sequences can be used to control the interparticle interaction. However, the direct and effective ways to tune the attractive interaction for DNA-mediated particles could be made by changing the DNA grafting-density. Dreyfus *et al*.(*37*, *38*) and Nykypanchuk *et al*.(*39*) introduced inert or non-hybridizing oligonucleotides to help sterically stabilize the particles while allowing for control over the attractive interaction. Alternatively, Casey *et al*. showed that control

of the hybridization can be achieved by mixing two different DNA strands, which are complementary pairs, on each particle surface.(*40*). Simply, interparticle interactions can be tuned with the number and type of base-pairing with particles coated with complementary DNAs (*41*). However, Wang et al. (*34*), recently, reports short sticky ends with as few as four bases is favorable to form crystalline structures. Additionally, smooth surfaces achieved effectively through considerably high surface coverage of ssDNA has been shown to be critical to facilitate critical rolling and rearrangement of bound particles near the melting temperature of the complementary DNA strands, a process believed to be important in the eventual crystallization of micron-sized particles. Very recently, the very narrow temperature window of DNA-coated particles, which makes long-range crystallization notoriously difficulty, can be controlled by applying new concepts such as mobile DNA linkers (*42*) and DNA displacement (*43*).

Despite the significant advancement in recent years in our understanding of DNA-mediated particle assembly, the assembly of microparticles into crystalline structures is generally poorly understood relative to the extensively studied crystallization of gold nanoparticles *via* DNA-mediated interactions (*32*, *44*, *45*). Moreover, while progress toward 'open' lattices (eg., diamond) has been limited, it is these elusive structures that are some of the most sought after microparticle arrangements for applications. To better understand this challenge, it is insightful to consider the differences between nanoscale and microscale particles and to understand the factors that play a role (either positive or negative) in DNA-mediated self-assembly (*27*).

1.2.2 Self-Assembly of DNA-coated Nanoparticles

The seminal reports in the area of DNA-mediated particle assembly were first achieved by Alivisatos *et al*.(*46*) and Mirkin *et al*.(*47*) through treatment of gold nanoparticles (1~14 nm) with thiol-capped oligonucleotides. These studies underlined the potential role of biomolecules in complex self-assembly, and opened the prospect of designing useful and varied structures that would self-assemble in a *selective* and *reversible* way. Several research groups have contributed to accomplishing this conceptually simple yet powerful idea. Early demonstrations focused mainly on the formation of amorphous polymer, where coarse placement and periodicity of particles was controllable (*39*, *48*–*56*). The results were attributed to unusual physical properties of highly polyvalent DNA-coated particles that are different from free DNA in solution. Interestingly, the melting transition of the DNA-coated particles becomes shaper than that of the free DNA due to the cooperativity induced by the close proximity of the charged DNA or the entropy loss induced by the reduced configurational freedom of attached DNA (*29*, *37*, *57*, *58*). The very narrow window of temperature over which association/dissociation of DNA-coated particles occurs, makes it difficult to find the correct conditions for achieving ordering of the particles as equilibrium states. Still, there is relatively little information on what factors are responsible for the existence of substantial kinetic barriers in this system. This challenge has partly been overcome using carefully designed DNA-particle systems with careful temperature control or thermal cycling (*32*).

The first successful experiments for the formation of three-dimensional crystal structures have been performed by both and Gang *et al*.(*32*) and Mirkin *et al*.(*45*) using binary mixtures of gold nanoparticles functionalized by complementary sticky ends or by

linker duplexes. The crystallization based on careful annealing and designing of DNA was monitored *via* synchrotron based small-angle X-ray scattering (SAXS), and showed the reversible formation of body-centered cubic lattices, structures of lower density than close-packed (e.g. fcc, hcp) structures that are thermodynamically favored for simple hard sphere assembly. That work and others has established that the determination of DNA sequence, DNA length, and DNA flexibility are significant to create micrometer-sized crystal structures. Subsequent works have been conducted to understand diverse factors in the formation of DNA-programmable superlattices, including various particle shape and particle compositions (*59*, *60*), DNA length to control the lattice parameter (*61–64*), and environment (*65*). Recently, Macfarlane *et al*. (*44*) proposed six empirical design rules governing the structure and lattice parameters of the crystal structures as a function of the particle size and the length and the number of DNA tethers. They observed nine distinct colloidal crystal structures under different conditions (**Figure 1.2**). Despite the extensive work in the area of DNA-mediated nanoparticle assembly, nanoparticle composition has rarely been extended beyond gold, and novel structures such as those with diamond-like crystal symmetry have yet to be realized.

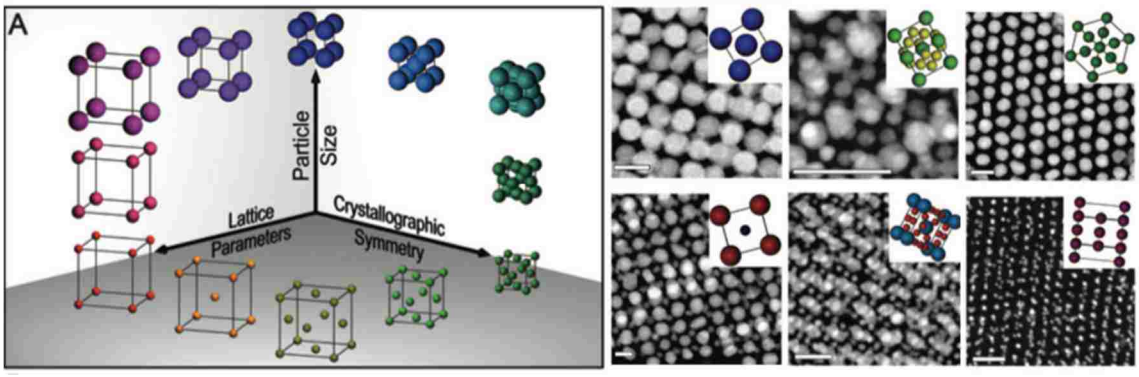

Figure 1.2. Three main factors in determining the crystal structures, and experimentally realized structures by tuning these factors

1.2.3 Self-Assembly of DNA-coated Microparticles

As mentioned above, while the self-assembly of the gold *nanoparticles via* DNA-mediated interactions has been achieved through development and exploitation of specific design rules, the assembly of *micron*-sized particles into various crystal structures has proven more difficult suggesting that design rules cannot be simply extended across scales. The fundamental differences between micron- and nanometer-sized particles that could underlie the barrier for realizing ordered microparticle structures include: (a) the high strength of attraction (*35*), (b) the sharp thermal activation (*37*, *38*), and (c) the lower mobility of these larger particles. These factors can drive microparticles to become kinetically hindered in metastable free-energy minima, slowing down equilibration dramatically (*20*, *27*, *42*).

A variety of research in microparticles has been performed to understand DNA-driven assembly of particles and thereby realize the formation of DNA-programmable crystal structures. The first *fully reversible* DNA-driven assembly of micron-sized polystyrene particles was proved by Valignat *et al*. (*35*) and Rogers *et al*. (*66*) These papers suggested that the addition of non-ionic surfactant or stabilizer allows DNA-driven assembly to enhance full dissociation or dispersion of aggregated particles upon heating above the DNA dissociation temperature (melting temperature, T_m). As discussed in Valignat's paper, careful consideration in controlling attractive interactions due to interparticle DNA hybridization and steric and/or electrostatic repulsive interaction is needed for micron-sized particles, unlike nanoparticles, in order to overcome irreversible binding due to the van der Waals interaction. The introduction of non-ionic surfactant or stabilizer to systems of micron-sized particles helped to increase the repulsive interaction.

Later research focused on understanding and exploring DNA-mediated assembly of microparticles, including: (a) the influence of ionic strength, the hybridization segment length, and composition of suspension mixtures on tuning the degree of attractive interactions between DNA-coated particles (*41*, *67*), (b) the utilization of secondary structure formation to the DNA to tune the interparticle interaction (*36*, *68*), (c) polygamous particles with multiple DNA sequences to bind specifically to many different partners (*69*), (d) the effect of DNA density on controlling the DNA-mediated interactions and theoretical approach (*37–39*), and (e) the direct measurement of DNA-mediated interactions between DNA-mediated microparticles (*70*, *71*).

Despite these attempts at diverse control of attractive interactions for DNA-mediated assembly, most of the self-assembled structures formed were large disordered aggregates or small polyhedral clusters rather than ordered structures. Only the work of Crocker *et al*.(*71–73*) showed DNA-mediated crystallization in close-packed lattices of micron-sized polystyrene, but they suggest that this can be accomplished only by long incubation (> 1 day) and within a very narrow temperature window (~ 0.5 °C) near the melting point. They further suggested that the specific surface chemistry employed was critical to induce interparticle rolling necessary for annealing ordered structures. Specifically, only polystyrene anchored PEGylated DNA (*74*) apparently displayed excellent colloidal stability, and was successful in growing small hexagonally stacked crystals. In contrast, they suggested that neither the avidin-biotin nor the carbodiimide chemistry for linking DNA to the particle surface could be used for achieving crystalline microparticle structures.

Additionally, they proposed that the formation of the crystal structure is very sensitive to the amount of DNA on the particles and the steric repulsion between the particles. In particular, crystallization was shown to be possible only if the hybridization-mediated attraction was strong enough to cause clustering, yet weak enough to allow structural rearrangement. Only very recently, have DNA-microparticle systems showing re-entrant liquid-solid-liquid transitions (*43*) as predicted theoretically (*75*) using DNA displacement and extended binary compositionally ordered structures using very smooth surface and very short sticky ends (*34*) been reported.

1.2.4 Two-Dimensional DNA-mediated Assembly

Numerous studies have focused on three-dimensional (3D) DNA-mediated particle assembly using nanoparticles as well as microparticles. Yet, despite its simplicity, advantage for *in situ* visualization (e.g., via inverted optical microscopy in the case of microparticles), and direct implications for applications in structured thin films, the study of two-dimensional (2D) DNA-mediated particle assembly remains poor. Specifically, the aims of 2D DNA-mediated particle assembly studies to date can be largely classified into three categories: (i) the fundamental understanding of DNA-mediated assembly, such as a quantitative modelling of association/dissociation transitions (*37*, *38*); (ii) the formation of DNA-functionalized particle monolayer on a patterned surfaces with complementary ssDNA strands (*76–79*); (iii) the hexagonal lattice of DNA-functionalized particles using different interactions without exploiting DNA hybridization (*80*, *81*).

In the case of 2D DNA-mediated particle assembly on patterned substrates (*76–78*), only surface-particle interactions were activated, and, thus, the resulting ordered structures were predominantly attributed to registry with the structural order of the underlying

template rather than particle-particle interaction. The introduction of different lengths of 'DNA likers' aimed at inducing lateral ordering, ultimately only controlled interparticle distance without extending the extent of ordering.

Template-free 2D hexagonal lattices were observed in two separate studies. However, these were not driven by specific and reversible DNA hybridization. Instead, one was driven by density and the other was driven by non-specific binding. Very recently, DNA-functionalized nanoparticles showed 2D phase transformation from hexagonal lattices to disordered network structures at positively charged lipid layers by controlling interparticle attraction depending on monovalent salt concentration (*82*). While electrostatic self-assembly(*83*) or self-assembly by Ising interaction (*84*), no reports have successfully demonstrated the accessibility of diverse 2D crystalline morphologies by exploitation of DNA-mediated interactions.

1.3 Thesis Overview

Motivated by the above mentioned challenges, this thesis aims to construct a diversity of crystalline arrangements by taking advantage of controlled mixing of complementary ssDNA strands on individual particles (a system we will refer to throughout this thesis as '*multi-flavored*'), deviating from the more common approach of functionalizing separate particles with the same complementary ssDNA strands (a system we will refer to throughout this thesis as '*uni-flavored*'). To achieve this aim, DNA-mediated *binary microparticle* assembly is implemented and monitored in *two-dimension* for simplicity and visualization. Furthermore, we will elucidate the feasibility of novel concept of DNA-mediated *microparticle* assembly *via* theory, simulation and experiment.

In Chapter 2, we describe sample preparation and characterization of DNA-coated microparticles used in this study. Specifically, single-stranded DNAs (ssDNA) are attached covalently onto micron-sized silica particles by taking advantage of silianization and subsequent cyanuric chloride chemistry. The resulting microparticles possess a specific and reversible, temperature-dependent behaviors corresponding to DNA association/dissociation between complementary DNA tethers. We also estimate surface coverage of DNA and effective DNA density by using a fluorescence technique.

In Chapter 3, we describe the effect of nonionic surfactant on DNA-mediated interactions between the microparticles. Firstly, we study the role of nonionic surfactant, which allows the DNA-coated microparticles to remain mobile near substrates (e.g., glass coverslips) used for their *in situ* observation, and for facilitating colloidal stability in solution to avoid non-specific particle aggregation and promote DNA-mediated assemblies. We work with 2D systems, due to fast settling of heavy silica particles from solutions of low enough solids content to result in relatively dilute particle coverage on substrates used for *in situ* observation. With that system, we establish melting profiles, namely transitions among freely dispersed (i.e., singlet) and aggregated or assembled states, that provide insight into characteristic inter-particle interactions. From the cooling and the following heating process, we find that the melting transition of DNA-coated particles is affected by the concentration of nonionic surfactant, and is modulated by the formation of micelles. These experiments indicate that additives such as nonionic surfactants that are commonly used as a stabilizing agent can also be used as an additional handle to modulate and tune DNA-mediated interactions (i.e., along with salt and other means) as a tool for helping to

achieve long-range colloidal crystallinity. We also discuss how this modulation of melting temperature may be influenced by the critical micelle temperature (CMT) in this system.

In the studies described in Chapter 3, we also begin to explore how functionalization of the particles with a mixture (50/50) of complementary ssDNA strands ('multi-flavoring') influences the resulting assemblies as compared to the binary systems where the complementary ssDNA strands are attached to separate particles ('uni-flavoring'). These studies provide first insight into the formation of both square and hexagonally packed structures that motivate more detailed study of the so-called 'multi-flavored' system. The remainder of this thesis describes computational, theoretical, and experimental work that explores the structural diversity that can be predicted and experimentally verified for these 'multi-flavored' systems.

In Chapter 4, we describe a comprehensive strategy that makes use of available information on pair interactions between DNA-coated particles from molecular dynamics (MD) simulation, to calculate the relative stability of various crystal polymorphs as a function of interparticle attraction strengths. Here, we work with effective pair potentials derived from explicit DNA-particle coarse-grained model. For simplicity, we present theoretical and simulation results on a system of equal-sized particles that can be assembled in two-dimensional (2D) crystalline lattices. The key parameter is the relative attraction strengths between like particle pairs (E_{AA}, E_{BB}) with respect to unlike particle pairs (E_{AB}). We design these relative interactions based on 'multi-flavored' system, deviating from the conventional 'uni-flavored' system. To be more specific, we work with two design strategies, symmetric ($E_{AB} > E_{AA} = E_{BB}$) and asymmetric one ($E_{AB} > E_{AA} > E_{BB}$ or $E_{AB} > E_{BB} > E_{AA}$). First, we use lattice energy calculations to obtain a quick estimate of relative

stability of possible crystalline structures, and then use MD simulations to test the predictions of such calculations. MD simulations are also complemented with standard free energy calculations, as needed, to further verify results. We determine the range of E_{AA}/E_{AB} and E_{BB}/E_{AB} values, suitable for assembling particles in square versus hexagonal lattices (alternating string, honeycomb, etc.).

In Chapter 5, we present representative experiments aimed at testing MD simulation predictions of 2D assembly of microparticles into diverse crystal structures. We work with asymmetric design of interparticle interactions, which shows various crystal phases, such as square and hexagonal lattices (honeycomb, kagome and square kagome). Microparticles are functionalized by a tailored mixture of two different, partially complementary DNA strands (αDNA, βDNA). Here, we demonstrate that attractive interaction strengths can be tuned by controlling particle 'flavoring' via control of the ratio of αDNA, βDNA predicted by the simple statistical mechanics model from Chapter 4 that defines relative attractive interactions. Also, we present the effect of particle number ratio on DNA-mediated particle assembly in 2D. As a result, by using an optical microscope, we observe particles arranged in square, pentagonal and hexagonal structures, which are compositionally ordered in unique and desirable honeycomb as well as kagome lattices.

In Chapter 6, we provide a summary of the main findings of this work and briefly discuss suggestions for future work on this research.

Chapter 2:

Sample Preparation and Characterization

2.1 Introduction

Numerous study has been done to functionalize DNA chains, consist of binding group, spacer and sticky ends, on colloidal particles. In available literatures, we briefly describe commonly used methods to graft DNA to nano-sized or micron-sized particles. Also, we present the methods to determine nominal and effective DNA density.

For nanoparticles, most of crystals assembled by DNA-directed interactions are based on gold nanoparticles with alkylthiol-terminated DNA chains. This solid protocol by Mirkin and coworkers (*47*) is continuing to be used to other study with some modifications for DNA-mediated nanoparticle assembly. By simple mixing of them under aqueous conditions, alkylthiol-terminated DNA strands form stable binding with gold nanoparticles. Subsequently, DNA-coated nanoparticles can be obtained after centrifugation and subsequent removal of supernatant that includes only unbound DNAs. Further study strives to find DNA-based particles without non-specific binding. As a result, current system is mainly use high density of DNA strands (*31*) with dT-based spacer that possess the lowest affinity with gold (*30*).

Most of DNA-mediated microparticle assembly is based on spherical polystyrene. In the initial stage, three different coupling methods are used to graft DNA strands on the polystyrene particles: avidin-biotin linking, water-soluble carbodiimide linking or

swelling/deswelling method. Kim and coworkers (*72*) show that DNA-coated microparticles made by swelling/deswelling-based method successfully assemble into close-packed crystal structures. This method works with triblock copolymers adsorbed easily on polystyrene surface. Small amount of solvent allows the hydrophobic block of the polymer to penetrate the particle surface. Also, DNA can be reacted with hydrophilic block of the polymer. Hence, removal of solvent leads to DNA-labeled microparticles with long polymer spacer. In this case, additional treatment such as surfactant is not needed to remove non-specific binding. However, this method is limited to polymer-based colloids.

To quantify DNA grafting density on particles, fluorescence-based techniques (*31*) or radio-active labeling methods (*37*) can be used. For gold nanoparticles, appropriate chemical treatments is used to quantify loaded DNA density and hybridizable effective DNA density on the particle surface. For microparticles, flow cytometer can be used to quantify the number of DNA strands grafted per particles using fluorescent DNAs.

In our study, single-stranded DNAs (ssDNA) are attached covalently onto micron-sized silica particles by taking advantage of silianization and subsequent cyanuric chloride chemistry. The use of silica particles possess largely two advantages for further understanding of DNA-mediated particle assembly. Firstly, high density of silica particles (~ 2 g/ml) facilitate to make two-dimensional assembly. This enables to have simple and visual system to understand DNA-mediated particle assembly. Also, the various size of monodispersed silica particles can be easily synthesized by Stöber method and others (*85*, *86*) and the hydroxylated silica surface can be readily modified by diverse chemicals (*87*, *88*). Using versatility of silica particles, we can develop DNA-mediated particle assembly

as a bottom-up approach to hierarchical materials with characteristic dimensions spanning nanometer to micrometer.

2.2 Materials and Abbreviations

The current section includes the materials and abbreviations used the following chapters. Surfactant-free silica particles were purchased from micromod Partikeltechnologie GmbH (Germany). Poly(ethylene oxide)-poly(propylene oxide)-poly(ethylene oxide) (PEO-PPO-PEO) triblock copolymer, or Pluronic® F127 and Pluronic® F88, was obtained from BASF and used without any further purification. Single-stranded sequences of deoxyribonucleic acid (DNA) were custom synthesized and standard desalting purified by Integrated DNA Technologies (Coralville, IA). Below table (**Table 2.1**) shows single-stranded DNA (ssDNA) used the following sections. Cyanuric chloride (CCl) and N,N-diisopropylethylamine (DIEA) were purchased from Sigma-Aldrich (St. Louis, MO). (3-Aminopropyl) triethoxysilane (APTES, 99%) was purchased from Acros Organics. Acetonitrile (99.7%) was purchased from Alfa Aesar. Two kinds of buffer solution were used throughout this work. One is 1x TE (pH 8.0) buffer consisted of 10 mM tris-HCl and 1 mM EDTA (ethylenediaminetetraacetic acid). The other is Borate buffer (pH 8.5) consisted of 200 mM boric acid and 50 mM sodium tetraborate.

Table 2.1 The DNA sequences used in this study. The underlined solid portions represent the sticky ends and can hybridize together to form a 7-basepair (between αDNA and βDNA) or 12-basepair (between δDNA and Cy5-γ'DNA) DNA duplex. The following section provides detailed information where they were used

DNA Name	Sequences (5' to 3')	Note
αDNA	NH_2-$(CH_2)_6$-$(T)_{50}$-TAATGCCT**GTCTACC**	
βDNA	NH_2-$(CH_2)_6$-$(T)_{50}$-TGAGTTGC**GGTAGAC**	
γDNA-Cy5	NH_2-$(CH_2)_6$-TTTTTTATGTATCAAGGT-Cy5	to quantify the number of attached on the particle
δDNA	NH_2-$(CH_2)_6$-TTTTTT**ACCTTGATACAT**	to quantify the number of the effective DNA
Cy5-γ'DNA	Cy5-**ATGTATCAAGGT**	to quantify the number of the effective DNA

2.3 Particle Functionalization

2.3.1 Intermediate Silica Particle Functionalization

Silica particles (1 and 1.5 μm, micromod Partikeltechnologie GmbH, Germany) were functionalized with single-stranded 5'-primary amine-modified DNA, ssDNA (Integrated DNA Technologies, Inc), via intermediate cyanuric chloride tethers as schematized in **Figure 2.1**a (*88*). The cyanuric chloride tethers were achieved by firstly functionalizing the native silica particles with (3-aminopropyl) triethoxysilane (APTES, Acros Organics),(*88*, *89*) the amine groups of which were subsequently reacted with cyanuric chloride (CCl, Sigma-Aldrich). Specifically, 0.9 ml of a 50 mg/mL silica particle solution was washed by three times of centrifugation (4,000 rpm/1 min) using high speed centrifuge (MTX-150, TOMY SEIKO Co., Ltd) and replacement of the supernatant with fresh ethanol (190 proof). Then, a ~3 wt% ethanol-silica solution was sonicated for 20 minutes to redisperse particles. APTES was added to the resulting solution to achieve an APTES:(surface silanol) molar ratio of 1.2:1, with silica surface silanol functionality estimated assuming monodisperse spherical particles of 1 μm diameter, 2 g/cm^3 of silica density, and ~6 SiOH/nm^2 of surface silanol density(*90*). The mixture was allowed to react in a sealed centrifuge tube for ~12 hours at room temperature under moderate rotation. The resulting NH_2-functionalized silica particles were washed six times by centrifugation and redispersion in ethanol. The composition of unreacted APTES in the supernatant from each washing step was assessed via reaction of its amine functionality with ninhydrin(*89*, *91*) reagent, resulting in Ruhemann's purple, concomitant visible purple coloration of the solution, and development of signature UV-vis bands at 407 nm and 570 nm as measured on an UV-visible spectrophotometer (Ultrospec 3300 pro, Biochrom Ltd.). The ninhydrin

reaction was carried out through addition of 250 μL of a 20 mM ninhydrin in ethanol to 1 mL of the test solution, in this case the supernatant, with subsequent heating at 65°C for 30 min. Centrifugation and redispersion washing cycles were continued on the functionalized particles until the ninhydrin-treated supernatant became colorless and the UV-vis signature nearly disappeared. Three washings beyond the number (typically 3) where colorless supernatants were achieved were consistently performed to ensure removal of all unreacted APTES. Subsequent ninhydrin indicator reactions were carried out as described above on the 1 wt% NH_2-functionalized silica particles in ethanol to investigate existence of amine groups on silica particles.

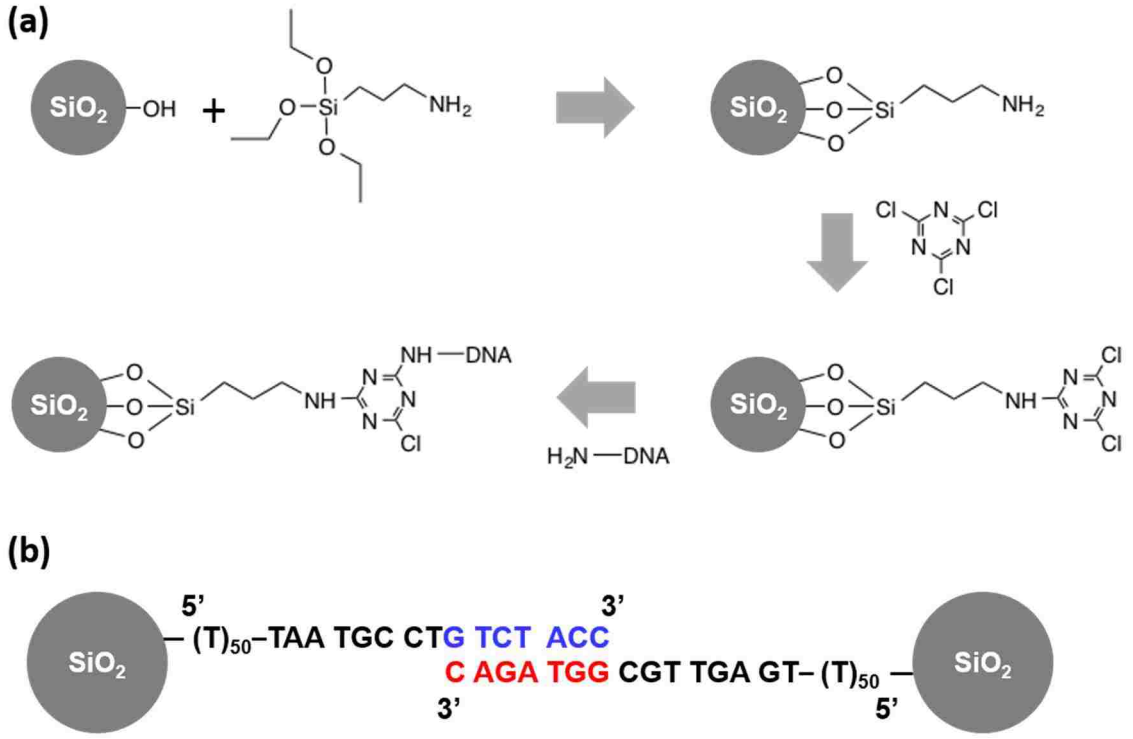

Figure 2.1 (a) Scheme of attaching amino-modified oligonucleotide to silica particles. (b) Scheme of the hybridization between αDNA- and βDNA-functionalized silica particles.

The NH_2-functionalized silica particles were transferred from ethanol to acetonitrile (Alfa Aesar, 99.7%) by three times of centrifugation and solvent exchange to yield a final solids content of ~5 wt%. It was followed by addition of N,N-diisopropylethylamine (DIEA, Sigma-Aldrich), for which molar ratio of DIEA to surface silanol was 17.5:1, and then 30-minutes sonication to get well-dispersed NH2-functionalized silica particles in acetonitrile. Finally, cyanuric chloride (CCl, Sigma-Aldrich), for which molar ratio of CCl to surface silanol was 69:1, was inserted to this solution. After reacting at room temperature for 2 hrs, the mixture was washed 6 times by sequential centrifugation and solvent exchange with fresh acetonitrile, and sonication steps. Aliquots of the resulting mixture were solvent exchanged with ethanol and used for carrying out ninhydrin indicator reactions as described above to assess the success of nucleophilic substitution of the CCl chlorine by amines on the surface of silica particles. **Figure 2.2** compares the UV-vis absorption spectra for ninhydrin-treated NH_2-functionalized and CCl-functionalized silica particles, with existence and absence, respectively, of absorption bands near 407 nm and 570 nm indicating the NH_2 functionalization of the base silica particles and nearly complete reaction of CCl with that functionality.

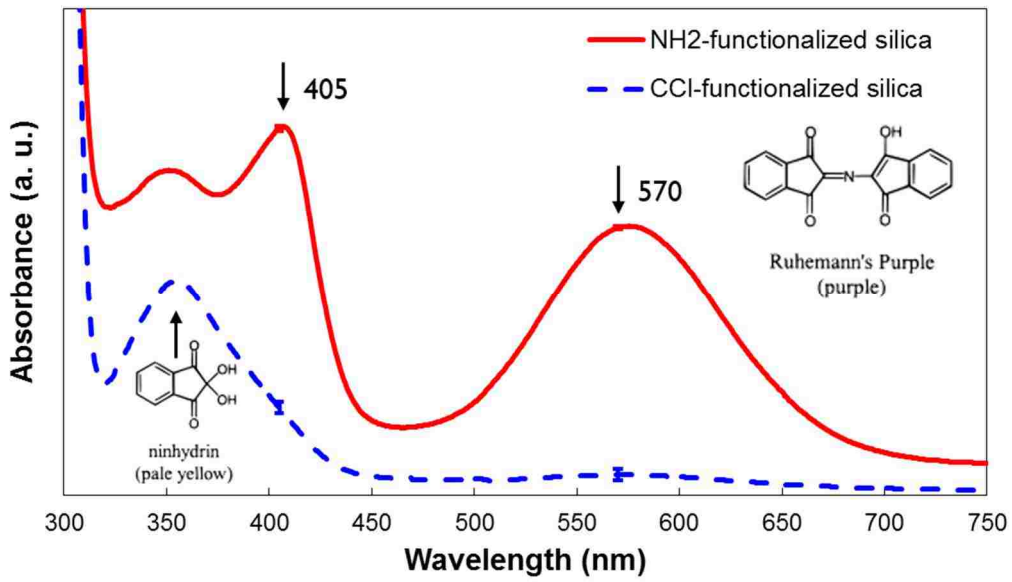

Figure 2.2. UV-vis absorption spectra of the supernatant solutions of the reaction mixtures of ninhydrin with the amine- and CCl-functionalized silica in ethanol.

2.3.2 ssDNA Functionalization of Silica Particles

Covalent attachment of DNA oligomers to the surface of CCl-functionalized silica particles was carried out following the procedure outlined by Steinberg and coworkers (*88*) using DNA oligomers with complementary short sticky ends to form DNA duplex as shown in **Figure 2.1b**, as one of the example. CCl-functionalized silica particles in acetonitrile were first cleaned with, and redispersed at a concentration of ~3.2 wt% in a borate buffer (pH 8.5) consisting of 200 mM boric acid and 50 mM sodium tetraborate. 100 μL of this CCl-functionalized silica solution was added to an oligo-NaCl solution prepared by mixing 324 μL of borate buffer including 848 mM NaCl and 6 μL of 300 μM DNA in aqueous solution. The mixture was allowed to react in a sealed Eppendorf tube for ~12 hrs at room temperature under gentle rotation. The DNA-functionalized silica particles were then washed more than 6 times by centrifugation and redispersion in TE buffer (pH

8.0) consisting of 10 mM tris-HCl (pH 8.0), 1 mM ethylenediaminetetraacetic acid (EDTA), and 100 mM NaCl. The existence of unreacted DNA was assessed by analysis of UV-vis or fluorescence spectrum for each supernatant. Typically, more than 4 washes were required to remove most of the non-tethered DNA.

Mirkin *et al*. has established that the coverage of DNA on the gold nanoparticle can be modulated by using the salt-aging process (*31*, *92*). Therein, the existence of salt facilitates increasing density of surface-tethered DNA due to the screening of charge repulsions between neighboring DNA strands. In our system, ~ 860 mM salt is nominally included to attach the DNA strands to CCl-functionalized silica particles. As a simple control study, we synthesized two sets of DNA-mediated particles, one in the presence of salt and the other without, to see the effect of the salt on the attachment of DNA to silica micoparticles. The DNA-functionalized particles made in salty solution aggregated, but the particles made in non-salty solution formed only singlets at room temperature. This indicates that we can use salt aging process to achieve detailed control of surface density on the micron-sized silica particles.

2.3.3 Quantitation of Loaded and Hybridized ssDNA

In order to quantify the density of DNA oligomers on the silica particle surface, DNA oligomer functionalization of NH_2-functionalized particles analogous to that described above was carried out using fluorescently labeled DNA (5'-NH_2-$(CH_2)_6$-TTTTTTATGTATCAAGGT-Cy5-3', **γDNA-Cy5**, Integrated DNA Technologies).(*41*) Fluorescence measurements (λ_{ex} = 648 nm, λ_{em} = 668 nm) on a TECAN infinite M2000 PRO (**Figure 2.3**) comparing fluorescence spectra collected for solutions of the CCl-

functionalized silica particles and silica particles subsequently functionalized with Cy5-modified DNA reveal distinctly marked absorption over signature Cy5 wavelengths (680 nm~740 nm) only in the case of functionalization with the Cy5-modifed DNA. Based on calibrated absorption at 696 nm correlated with **γDNA-Cy5** concentration (without silica particles), a DNA surface density of approximately 38,000 DNA/μm^2 was estimated. Since the **γDNA-Cy5** bears a different sequence and lower number of base pairs (18 bps) compared to the nominal DNA (**αDNA and βDNA)** employed in this study (65 bps), we anticipate this estimated density may serve as an upper bound for the actual density of the 65-bp DNA on the silica surface.

In order to determine the activity of loaded ssDNA for hybridization, another fluorescently labeled DNA (**Cy5-γ'DNA**), which were complementary to the surface-bound oligonucleotides (**δDNA**), were reacted with the DNA-functionalized non-fluorescent silica particles (568 nm diameter) under hybridization conditions (0.1 M salty TE buffer with 1 wt% Pluronic® F127, pH 8, 2 hours). An excess (2×) of the labeled DNA compared to the amount of surface-bound ssDNA, which was already measured, was used. Following incubation, the particles were washed 7 times by sequential centrifugation and redispersion by the same buffer to remove excess Cy5-labeled DNA target strands. Then, the fluorescence intensity of the particle solution was measured by the fluorescence spectroscopy, as described above, to estimate the number of hybridized Cy5-labeled DNA. Based on this result, we estimated the density of effectively hybridizable DNA on the particle was approximately 1,300 DNA/μm^2.

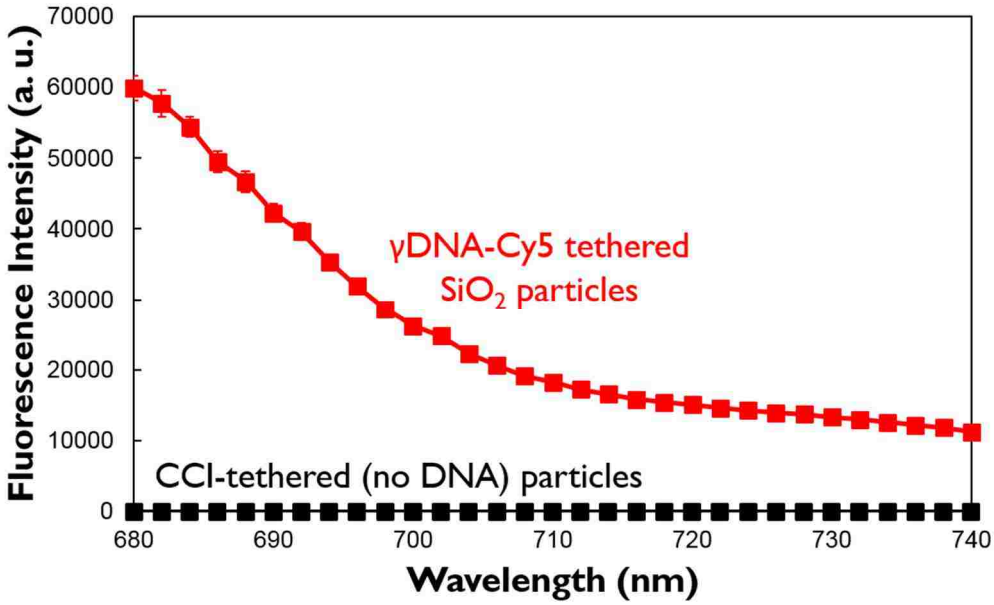

Figure 2.3. Fluorescence spectra of the cyanuric chloride functionalized silica reacted with fluorescent DNA and the cyanuric chloride functionalized silica.

2.4 Specific and Reversible Assembly of DNA-coated Silica Particles

Employing the established imaging conditions, we have studied the dynamics, interaction, and assembly of mixtures of silica particles functionalized with complementary strands of DNA. In order to verify that inter-particle binding that we observe is a result of hybridization occurring between complementary strands of DNA, we have studied the assembly of αDNA- and βDNA-functionalized particles of distinctly different sizes. Namely, we have functionalized 1 μm particles with αDNA and larger, 1.5 μm particles with complementary βDNA. The binding process was performed in salty TE buffer including nonionic surfactant at room temperature and observed using the optical microscope. As shown in **Figure 2.4**, we observe the assembly of small clusters wherein only association between large and small particles occurs (i.e., particles functionalized with complementary DNA). No clusters of particles of the same size (i.e., same DNA) are

observed. This suggests, that under the assembly conditions studied, particle assembly results from DNA hybridization as opposed to non-specific aggregation of particles.

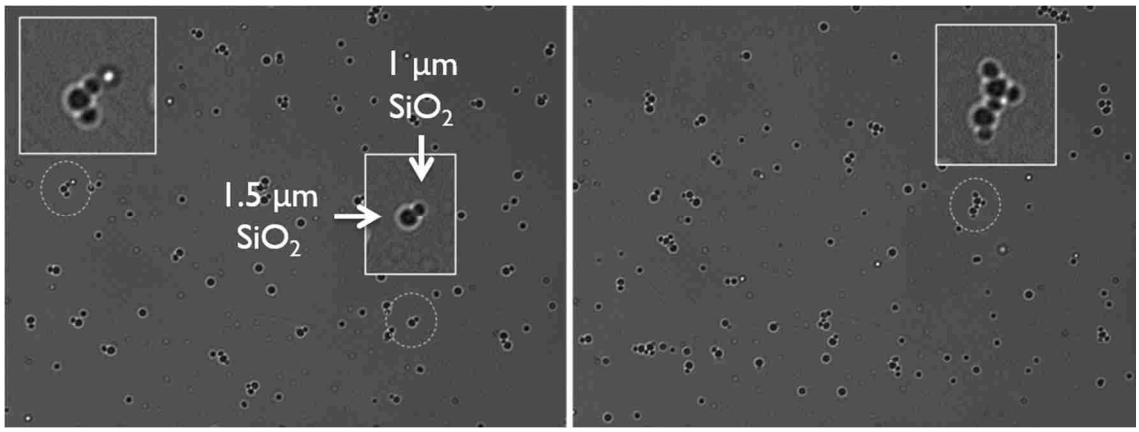

Figure 2.4. The assembly of the binary DNA-mediated particles (1 μm and 1.5 μm sized particle) to see the specific binding.

To see the reversibility of the assembly of DNA-mediated silica particles, we tried to look at temperature-dependent assembly of the mixture of the particles in salty TE buffer with nonionic surfactant. Initially, the particles were aggregated and showed fractal-like structures at room temperature. Increasing temperature allowed the aggregated particles to start to dissociate and finally showed full dissociation at temperatures above the melting temperature. Subsequent decreasing of the temperature led to re-association of the particles, with further decreases to room temperature showing full aggregation like the initial state. **Figure 2.5** describes temperature-dependent dissociation/association of DNA-mediated silica particles. Therefore, these data suggest that the prepared DNA-functionalized silica microparticles possess *a specific and reversible, temperature-dependent behavior* consistent with DNA hybridization and dehybridization between complementary DNA tethers, attached to 'binary' silica particles.

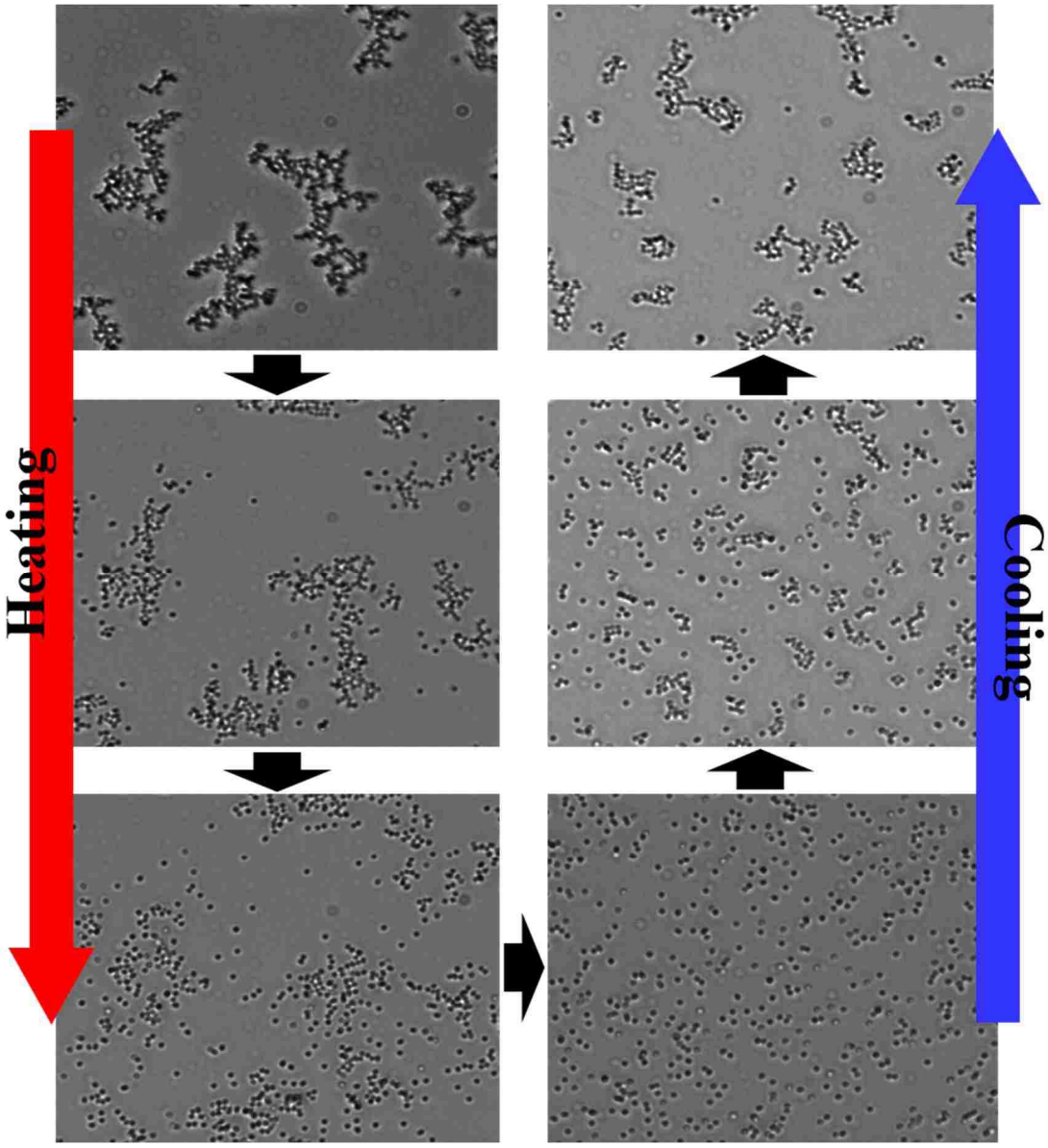

Figure 2.5. The temperature-dependent reversible assembly of DNA-mediated silica particles

2.5 Conclusion

In this Chapter, we demonstrate the protocol to prepare and subsequently characterize DNA-coated particles. Specifically, single-stranded DNAs (ssDNA) are attached covalently onto micron-sized silica particles by taking advantage of silianization and subsequent cyanuric chloride chemistry. The resulting microparticles possess a specific and reversible, temperature-dependent behaviors corresponding to DNA association/dissociation between complementary DNA tethers. We also estimate surface coverage of DNA and effective DNA density by using a fluorescence technique. The salt-aging process can be exploited to increase or decrease DNA density to control interparticle interactions.

Chapter 3:

Effect of Nonionic Surfactant on Association/Dissociation Transition of DNA-Functionalized Colloids

3.1 Introduction

It is well-known that DNA-mediated interaction can be mainly controlled by temperature (*38*, *70*). Thus, determination of melting temperature and its understanding can play a significant role in constructing crystalline structures or desired structures. Nykypanchuck *et al*.(*32*) showed 3-dimensional crystalline structures of gold nanoparticles using long flexible DNA and thermal cycling across melting temperature. In this study, the formation of crystalline structures was dramatically slow much below melting temperature due to high DNA hybridization energy. Weak and reversible DNA-mediated attraction near melting temperature allowed the particles into thermodynamically stable crystalline structures. Furthermore, processing temperatures based on melting temperature can provide different structures of DNA-mediated assembly. Park *et al*.(*45*) showed different crystal structures, a close-packed structures at near melting temperature and a non-close-packed structures at several degrees below melting temperature, depending on assembly temperature due to competition between entropic and enthalpic contributions. Therefore, predetermined melting temperature can be a useful criterion to design an efficient

annealing schedule for equilibrium phase and secure desired structures in DNA-mediated assembly.

Along with the position of melting, observation of shape of melting transition can play a significant role in finding right conditions for crystalline structures. Generally, the melting transition of DNA-functionalized particles is much sharper than that of free DNA.(*37*, *57*) The sharp melting transition is more influential to microparticles than nanoparticles due to extent of inter-particle hybridization (*27*). Thus, the assembly of micron-sized particles into crystalline structures has been quite difficult to achieve as micron-sized particles encounter, easily, metastable free-energy minima due to large number of DNA hybridization between the particles in the narrow window of temperature. To date, short-ranged crystallization was accomplished by long incubation with very narrow window of temperature and special DNA coupling chemistry.(*71*, *72*) A recent research provides an experimental clue regarding the correlation between the shape of melting curve and the ordered structures. Leunissen *et al*.(*42*) showed that wider association/dissociation transition by using particles with surface-mobile DNA linkers, which could be comparable the particle-particle rolling for further rearrangement, could provide a much larger temperature window for equilibrium self-assembly and thus facilitate the formation of well-organized structures. Therefore, the observation of melting profile can be used not only to predict the possibility of well-ordered structure by using wide window of temperature but also to know which factors are dominate to give broader annealing range.

In addition, recently, the utilization of multiple melting temperatures induced by multiple binary DNA-functionalized particles can provide strategies for new materials.

Michele *et al*.(*93*) reported that two well-defined melting temperatures by two binary DNA-functionalized particles can be used to, sequentially, trigger selective interactions and thus allowing two-step gelation and core-shell gelation for mesoporous materials. Recently, Macfarlane *et al*. (*94*) also exploited two different melting temperature to realize topotactic interconversion for more complex crystal structures. Here, they generated five ternary nanoparticle superlattice by insertion of smaller particles into a pre-established crystal structure, which is across the first melting temperature, by activating DNA-mediated attraction sequentially. Therefore, it is essential that the underlying origin of the melting properties be unraveled as the observation of melting curve directly impact one's ability to design annealing process and build materials from DNA-functionalized particles.

Several research groups have been performed to understand DNA-mediated interaction depending on various parameters, such as DNA sequence (*41*), DNA length (*29*, *95*), surface density on particles (*38*, *39*), and salt concentration (*39*, *67*). Among them, Jin et al. (*29*) investigated systematically the melting temperature for DNA-coated gold nanoparticle to evaluate and define the contribution of particles, oligonucleotides and others by using UV-visible spectrophotometer. They reported that the melting temperature and the width of melting transition can be changed by various variables, such as the particle size, the surface density of DNA, salt concentration and interparticle distance. For micro-sized particles, Dreyfus and coworkers (*37*, *38*) initiated to use images of colloids by using a light microscope to get a melting curve. Since this system was regarded as two-dimensional by using particles with high density, they were able to measure the fraction of nonaggregated particles or the "singlet fraction" on the surface through dividing the singlet area by total area of particles. They investigated the association/dissociation transition of

DNA-coated particles as a function of the temperature and the surface density of DNA. As a result, the melting temperature increased with increasing the DNA surface density, whereas the broadness of the melting profile decreased slightly. In earlier work by Valignat et al. (*35*) reported that reversible self-assembly of DNA-coated particles was achieved by introduction of adsorbed polymer, which produce steric repulsion between inter-particles, onto the particle surface. Interestingly, they investigated the melting profiles of DNA-coated particles with various copolymers that were used as stabilizers and thus showed that melting temperature of DNA-coated particle increased with decreasing the molecular weight of stabilizers owing to lower steric hindrance effect. This sensitivity of the melting transition is particularly interesting given the convention to use surfactant as a means to stabilize particles against non-specific aggregation. It raises the question about the system sensitivity to this required and/or often used additive.

No previous study, to our knowledge, has comprehensively and systematically reported on the effect of varying commonly used surfactant amount on the melting curve. In this Chapter, we present the melting curve of DNA-functionalized particles with the concentration of Pluronic® F127 (PEO_{100}-PPO_{65}-PEO_{100}) and Pluronic® F88 ($PEO_{103.5}$-$PPO_{39.2}$-$PEO_{103.5}$), which are used to promote colloidal stability and protect against surface adhesion. As a result, interestingly, we observed the change of association/dissociation transition of DNA-functionalized silica particles depending on the concentration of nonionic surfactants. Furthermore, we introduce two simple crystalline arrangements (square and hexagonal lattices) based on the pre-established melting profile for following Chapters.

3.2 Materials and Methods

3.2.1 Nonionic Surfactant

Pluronic® nonionic surfactants were used as a stabilizing agent for many colloidal dispersions. Pluronic® nonionic surfactants are composed of one centrally-positioned hydrophobic poly(propylene oxide) and two end-positioned hydrophilic poly(ethylene oxide) regions, as shown in **Figure 3.1** (*96*, *97*). Typically, the nonionic surfactant dissolves in dilute aqueous solution at low temperature as monomers. As the concentration or temperature increases, the critical micellization concentration (CMC) or critical micellization temperature (CMT) is observed, respectively, and leads to the formation of intermolecular micelles, which consist of a hydrophobic core of PPO segments and a hydrophilic shell of PEO segments.(*98*, *99*)

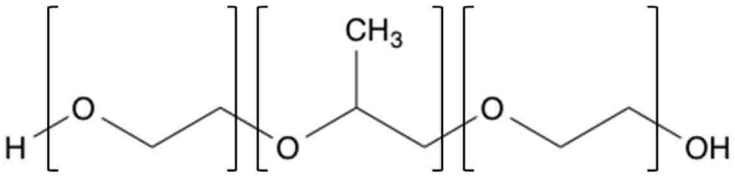

	Structure	Molecular weight	PEO wt%
Pluronic® F127	PEO_{100}-PPO_{65}-PEO_{100}	12,700	70
Pluronic® F88	$PEO_{103.5}$-$PPO_{39.2}$-$PEO_{103.5}$	11,400	80

Figure 3.1. The structure of tri-block copolymer Pluronic® and their detailed information from these references.

3.2.2 Microscopy Setup for Temperature Studies

A POCmini-2 Tissue Culture Chamber System (PeCon GmbH), hereafter referred to as a "heating chamber", was utilized for systematic heating and cooling of solutions of DNA-functionalized particles. Particle solutions were held by a silicone O-ring (ID=20mm, OD=30mm, borosilicate, Hemogenix®) sandwiched between two round coverslips (diameter=30mm, thickness=0.17mm) mounted within the heating chamber. The local temperature within the heating chamber was measured with a thermocouple (K-type, thickness=0.25mm, OMEGA Engineering, INC.) inserted at the chamber center. The chamber itself was placed on a Nikon Eclipse TE2000U inverted optical microscope equipped with40x air immersion objective with 1.5x amplifier. A temperature controller (Tempcontrol 37-2 digital, PeCon GmbH) and a chamber-compatible heating insert (Heating Insert P, PeCon GmbH) were used to scan and hold temperatures of the system during image collection. Full sedimentation of the DNA-functionalized silica particles for ~1 hour, owing to the silica density (ca. 2 g/cm^3), enabled two-dimensional (2D) optical imaging on the inverted microscope at a focal depth of ca. 1 μm to sufficiently capture 2D particle dynamics, aggregation, and assembly within the system (*37*, *100*). Optical analysis was employed to quantify particle dynamics and association during sequential temperature ramping/equilibration, with a minimum of five optical images from different regions across the sample chamber collected at each equilibrated temperature step. Subsequent image analysis was carried out using ImageJ software, employing particle identification and area percentage calculations in order to quantify the singlet fraction.

3.2.3 Sample Preparation

The detailed protocol to functionalize micron-sized silica particles with amine-terminated single-stranded DNAs was described in the previous Chapter. For following experiments, DNA-coated microparticles in salty TE buffer (0.1 M) are transferred into solutions with desired amount of nonionic surfactant, with repetitive centrifugation and re-dispersion. To this mixture, a controlled amount of Pluronic® nonionic surfactant F127 (0.1, 1, 2 wt%) or F88 (0.1 1, 2, 4 wt%) was added. For each melting study, solution of equal amounts of prescribed types of DNA-functionalized particles (e.g., αDNA-βDNA) was prepared in salty TE buffer with a total particle volume fraction of 0.0005 wt%, amounting to a nominal surface density of sedimented particles within the heating chamber of approximately 0.01 particle/μm^2. 10-minutes bath-sonication and vortex mixing were carried out in order to ensure homogeneous particle dispersion.

3.2.4 Cooling and Heating Elucidation of Melting Curve

Melting curves for mixtures of particles functionalized with complementary strands of DNA were quantified on the basis of the degree of particle dispersion and assembly/aggregation by the fraction of isolated or so-called 'singlet' particles existing at a specific equilibrated temperature. Melting behavior was assessed through cooling and subsequent heating experiments. The prepared sample solutions with equal were initially heated at 60 °C for 1 hr in an oil bath. Simultaneously, the heating chamber was pre-heated to a temperature exceeding the characteristic αDNA-βDNA melting temperature, here at least 40°C. After injecting 650 μL of the heated solution into the coverslip/O-ring reservoir in the pre-heated chamber, cooling studies were carried out by gradual, step-wise reduction

of the set point temperature, and intermediate temperature equilibration via ambient cooling. Cooling cycles were terminated once temperatures (here, ca. 25^{o}C) well below the nominal DNA melting temperature were reached and the singlet fraction reduced to approximately 10% or less. Subsequent heating cycles were performed by step-wise increase in the equilibrated set point temperature of the system.

3.2.5 Image Analysis for Mean Square Displacement

The sample preparation and measurement by the optical microscope were the same with previously mentioned methods. The temperature of measurement was controlled to 28 °C by using the heating chamber. 2,000 frames were taken to use image analysis of mean square displacement at a capture rate of ~ 4.7 frames/second. Each frame was composed of 1392 × 1040 pixels collected with 8-bit grayscale resolution. Particle tracking was carried out in which 2,000 frames sequential images were digitally acquired. The time-step between frames was around 0.210 seconds. The analysis composed of image processing and numerical processing has been performed by using MATLAB code provided by Dr. Maria Kilfoil (*101*) at University of Massachusetts at Amherst, which is based on IDL by Dr. John Crocker (*100*). The image processing is briefly composed of the feather finding and tracking. In the step of feature finding, the right rejection parameters (such as integrated intensity, eccentricity, and particle size, etc.) are established to optimize the number of false features rejected and real features and accepted. Then, based on the algorithm to minimize the total distance between features in two successive frames, the positions found in successive frames are connected into trajectories. As the numerical processing, the positions are firstly converted from pixel to micrometers and then the drifting in the data is removed. The obtaining of full trajectories from the feature finding

and tracking process is followed by the analysis of mean square displacement, as calculated as sum of the x and y direction MSDs.

3.3 Results and Discussion

3.3.1 The Role of Nonionic Surfactants

Nonionic surfactant plays a significant role in allowing the DNA-functionalized particles remain mobile on the substrate and for facilitating colloidal stability in salty TE buffer, both necessary conditions for studying DNA-functionalized dynamics and assembly. We find that the presence of nonionic surfactant helps stabilize the DNA-functionalized particles against both particle aggregation and non-specific binding to the glass surface with or without plasma treatment of the glass surface in the heating chamber including TE buffer solution with 100 mM NaCl. Namely, with particles functionalized only with αDNA, we find that without nonionic surfactant, most of particles stick to the glass surface of the heating chamber (**Figure 3.2a**). By plasma treating the glass surface, this irreversible binding of the particle to the glass surface can be avoided, enabling particle mobility on the surface. However, as shown in **Figure 3.2b**, in the absence of non-ionic surfactant non-specific aggregation of αDNA-functionalized particles occurs, even though there exists no complementary pair, βDNA-functionalized particles. Therefore, in this study, nonionic surfactant is critical not only to track the particles but also to study two-dimensional DNA-mediated dynamics and assembly by using optical microscopy.

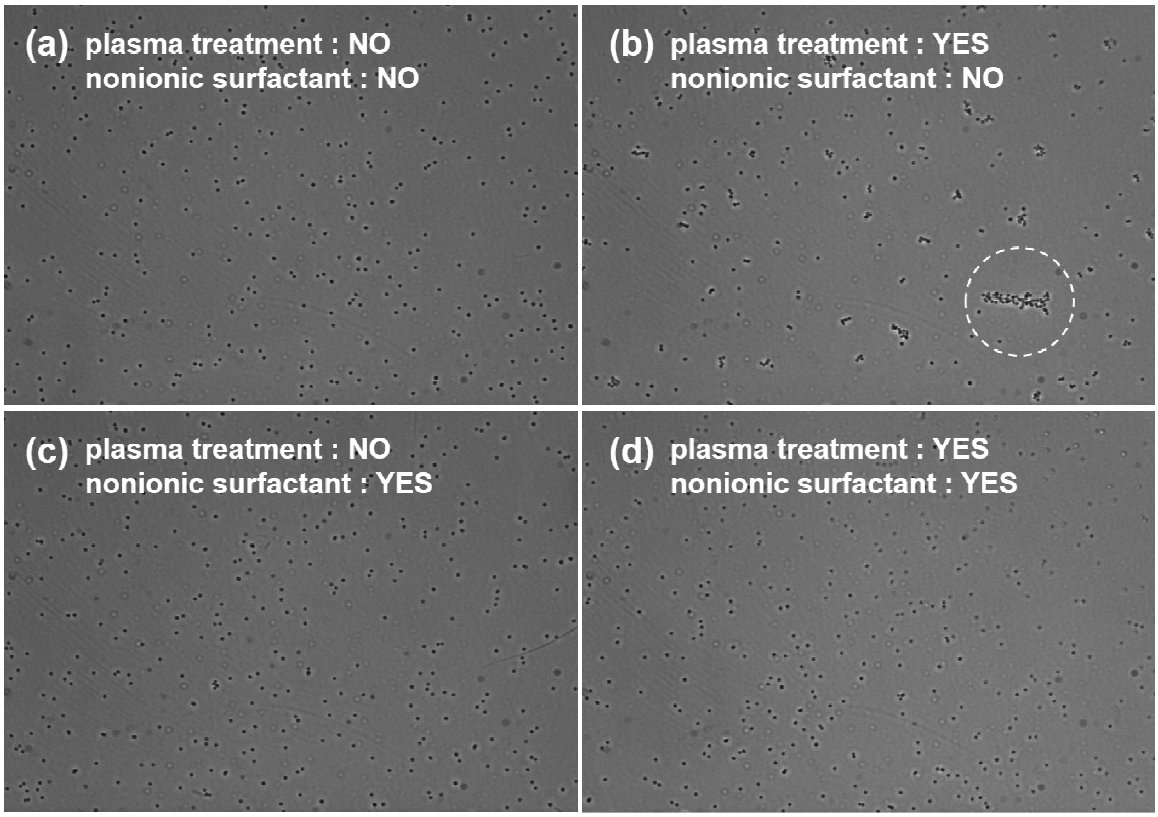

Figure 3.2. The images of αDNA-functionalized silica particles depending on the plasma treatment and the existence of nonionic surfactant in salty TE buffer. All particles have been anchored on the glass surface in **Figure 3.2a**. However, the particles moved freely on the surface in the other images (**Figure 3.2a, Figure 3.2c and Figure 3.2d**).

3.3.2 Time Dependence of Singlet Percentage

We firstly investigated the singlet percentage, defined as amount of unbound particles on the surface through dividing the singlet area by total area of particles, as a function of time and temperature to see how long it takes for singlet amount to be stabilized. For heating procedure the sample firstly remained at room temperature for at least two hours to get full aggregation of the particles and then 1 hour measurement has been performed to check the equilibrated time of singlet amount. **Figure 3.3a** shows the singlet amount as a function of time for the sequential heating to each temperature of interest. The percentage of singlet would reach constant value in 30 min to each temperature. Thus, we soaked the sample for 30-minutes at each temperature prior to obtaining the melting curve by heating. **Figure 3.3b** shows the time-dependent singlet amount with each temperature for the sequential cooling procedure. Consistent with the result of the heating tests, the singlet percentage appears to equilibrate within 30 minutes. Based on this time-dependent singlet percentage, the melting curve generated by cooling has been prepared through 30-minute equilibration at temperatures above and below the transition region, and 1-hour equilibration in the transition region to conservatively ensure establishment of equilibrium in this critical range.

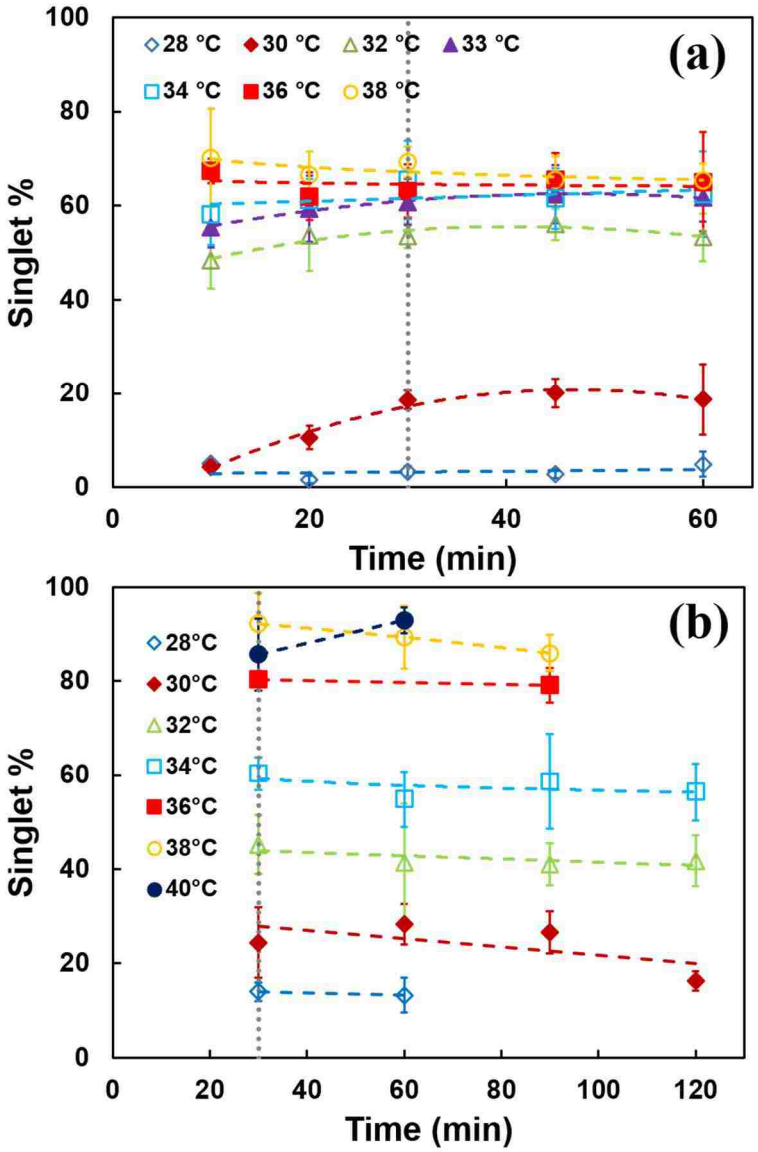

Figure 3.3. The singlet percentage as a function of time and temperature: **(a)** Sequential heating for DNA-functionalized silica particles in salty TE buffer including F127, **(b)** Sequential cooling for DNA-functionalized silica particles in salty TE buffer including F127

3.3.3 The Effect of Nonionic Surfactant on Melting Curve

To determine the effect of increasing nonionic surfactant concentration on the melting properties of DNA-functionalized aggregates, we studied melting behavior as a function of F127 concentration. **Figure 3.4a, 3.4b and 3.4c** show melting curves obtained by cooling and heating regiments according to the percentage of singlets (i.e., isolated particles) observed by optical microscopy (i.e., see **Figure 3.4d, 3.4e, and 3.4f**, for representative snapshots of decreasing singlet fraction with decreasing temperature). Interestingly, the melting behavior show that nonionic surfactant substantially affects the melting temperature of the DNA-mediated assembly. As the F127 concentration was increased from 0.1 wt% (**Figure 3.4a**) to 2 wt% (**Figure 3.4c**), the melting temperature increased from ~ 29 °C to ~ 33 °C, with subtle modulation of shape of transition. With respect to reversibility of the association and dissociation related to melting, the particles in salty TE buffer with 0.1 wt% F127 showed consistent melting profiles between cooling and the subsequent heating. Both the particles in salty TE buffer with 1 wt% F127 and 2 wt% F127 also showed consistent melting profiles, except a lower singlet percentage for the subsequent heating in the high temperature region. This might be due to the formation of micelles and thereby slower dissociation kinetics and different interactions for DNA-mediated assembly. Later, we will discuss about micelle formation and its influence on DNA-mediated particle assembly.

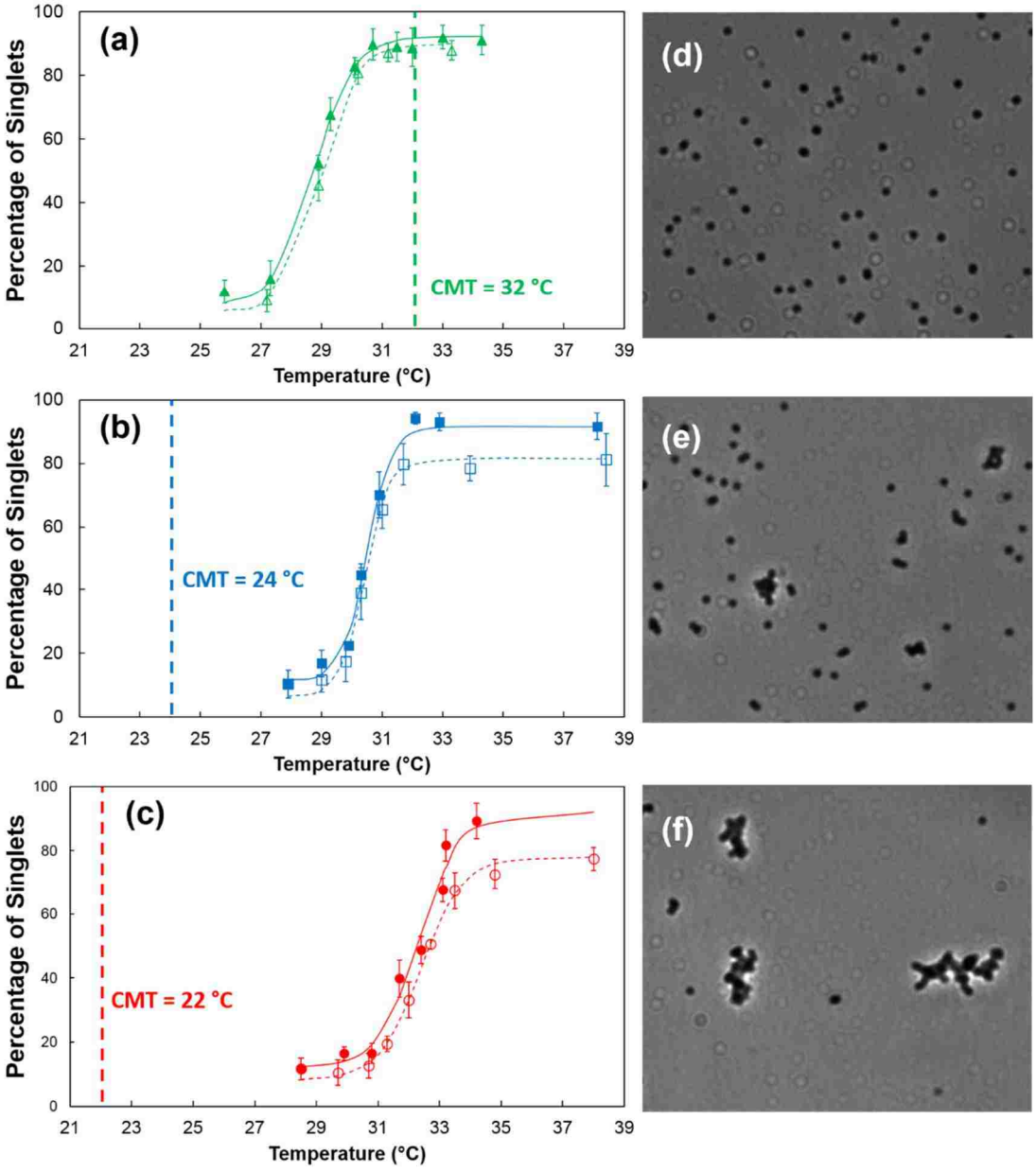

Figure 3.4. The percentage of singlet as a function of temperature for the mixture of αDNA- and βDNA-functionalized particles in salty TE buffer with **(a)** 0.1 wt% F127, **(b)** with 1 wt% F127, and **(c)** with 2 wt% F127 for cooling (solid symbol) and the subsequent heating (open symbol). The optical microscope images of DNA-functionalized silica particles in TE buffer with 0.1 wt% F127 (Figure 3.4a): **(d)** 31.5°C (above the melting temperature); **(e)** 28.9°C (inside the melting transition); **(f)** 25.8°C (below the melting transition). The vertical dotted lines in the Figure 3.4a, 3.4b and 3.4c indicate critical micelle temperature (CMT) at each F127 concentration in aqueous solution, adopted from Alexandridis et al.

Specifically, the formation of micelles of nonionic surfactant is determined by the concentration and temperature. The phase diagram (i.e., micellization boundary) for a variety of Pluronic® PEO-PPO-PEO copolymers in aqueous solutions has been established by Alexandridis et al.(*97*) The critical micellization temperatures in 0.1, 1 and 2 %w/v F127 of aqueous solution are adopted from this literature and plotted along with the melting curve, as the vertical dotted lines in **Figure 3.4**. In the case of 0.1 wt% F127 the melting temperature is slightly lower than the CMT. On the other hand, the melting temperatures for 1 wt% and 2 wt% F127 are much higher than the corresponding CMTs. Hence, it is quite difficult to know the exact nature of the influence of the micelle formation on melting transition of DNA-functionalized particles. For better understand how the relative melting temperature and CMT may play a role in the rise in the melting temperature as a function of the concentration of nonionic surfactant, we used Pluronic® F88 with similar molecular weight but much higher CMT than Pluronic® F127. In detail, the CMT of F88 in 0.1 %w/v of aqueous solution is ~50 °C, whereas that of F127 in the same concentration of aqueous solution is ~ 32 °C.

Figure 3.5 shows the effect of F88 concentration on the melting temperature of DNA-functionalized particles. Interestingly, the melting transition of DNA-coated particles in the salty TE buffer with 0.1 wt% of F88 is almost similar to that in the salty TE buffer with 1 wt% of F88, shown in **Figure 3.5a**. Increasing F88 concentration to 2wt% leads to an increase in melting temperature of DNA-functionalized particles in the salty TE. Additional increase of the amount of nonionic surfactant (4 wt% F88) leads to further rise of the melting temperature of DNA-functionalized particles.

This study shows a correlation between the melting transition and the CMT. For the system that has higher CMT than the melting temperature, the melting temperature is relatively insensitive to changes in the concentration of the surfactant. On the other hand, the melting temperature is similar or above the critical micelle temperature, the melting temperature of DNA-mediated particles shows a significant dependence on the concentration of the nonionic surfactant as shown in **Figure 3.5b**. This understanding is of practical importance given the need to establish detailed melting behavior in order to control crystallization and shows that surfactant concentration may serve as a handle for tuning the melting transition to higher temperatures to take advantage of enhanced particle mobility. However, it is necessary to do more research to interpret the detailed mechanism, such as the effect of monomer or micelles on the specific and attractive interaction among DNA-coated particles.

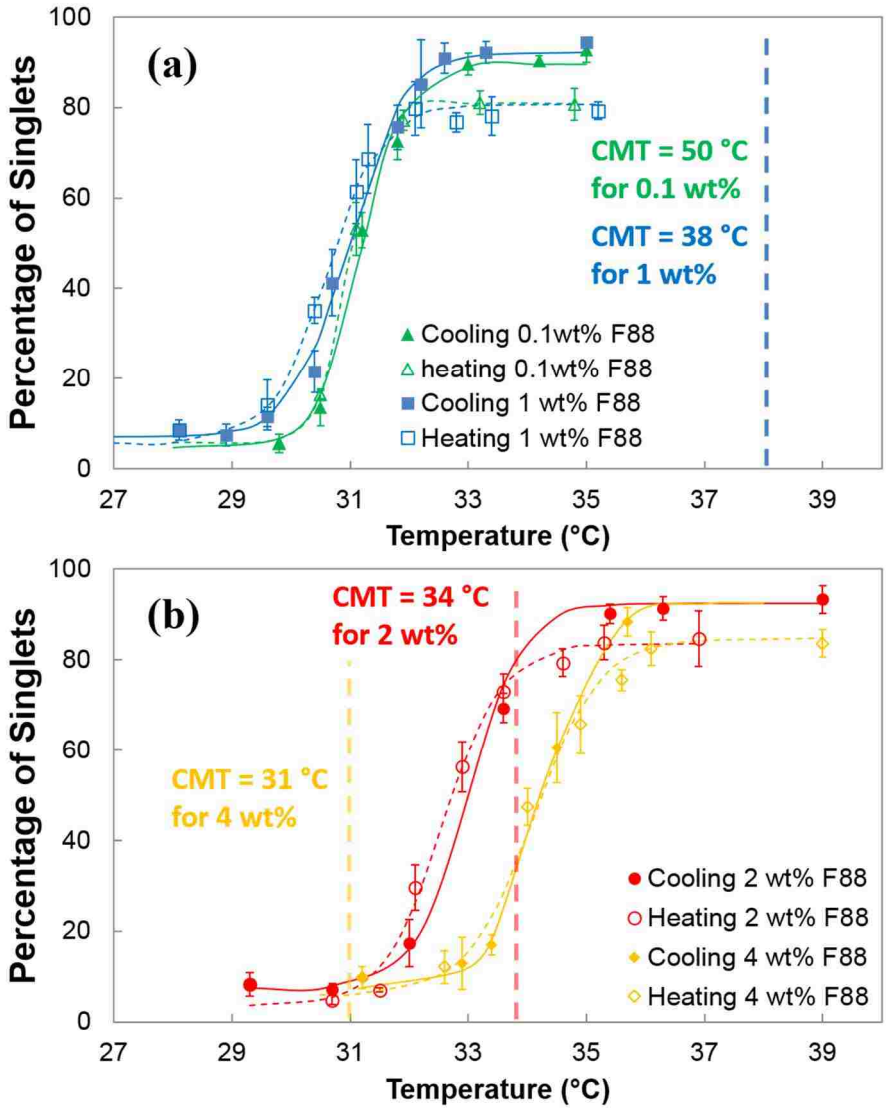

Figure 3.5. The percentage of singlet as a function of temperature for the mixture of αDNA- and βDNA-functionalized particles in salty TE buffer with (a) 0.1 wt% and 1 wt% F88 and (b) with 2 wt% and 4 wt% F88 for cooling (solid symbol) and subsequent heating (open symbol). The vertical dotted lines in the Figure 3.5a and 3.5b indicate critical micelle temperature (CMT) at each F88 concentration in aqueous solution, adopted from Alexandridis *et al*.

3.3.4 Further Discussion on Melting Transition

To understand melting transition of DNA-functionalized particles interconnected with the formation of micelles, other possible interactions with the exception for the DNA hybridization could be worth consideration in this study. Actually, we performed particle tracking tests depending on buffer solutions including different concentration of F127. The diffusion of the particles get slower with increasing F127 concentration in the salty TE buffer solution, as shown in **Figure 3.6**. In salty TE buffer including 2 wt% F127, it is started to see a few anchored particles with time. Furthermore, most of DNA-functionalized particles get stuck, with subtle jiggling motions, on the glass surface in salty TE buffer with 9 wt% F127. This slower diffusion with increasing the nonionic surfactant might be caused by structural changes from formation of a jammed array.(*102*) However, the concentration of F127 is not enough to make this structural changes, considering general concentration is more than 15 wt% of F127 to induce the jammed array of micelles. In this test, we can guess the existence of additional interaction according to F127 concentration, even though we can't reveal, clearly, additional interactions that induce different melting transition.

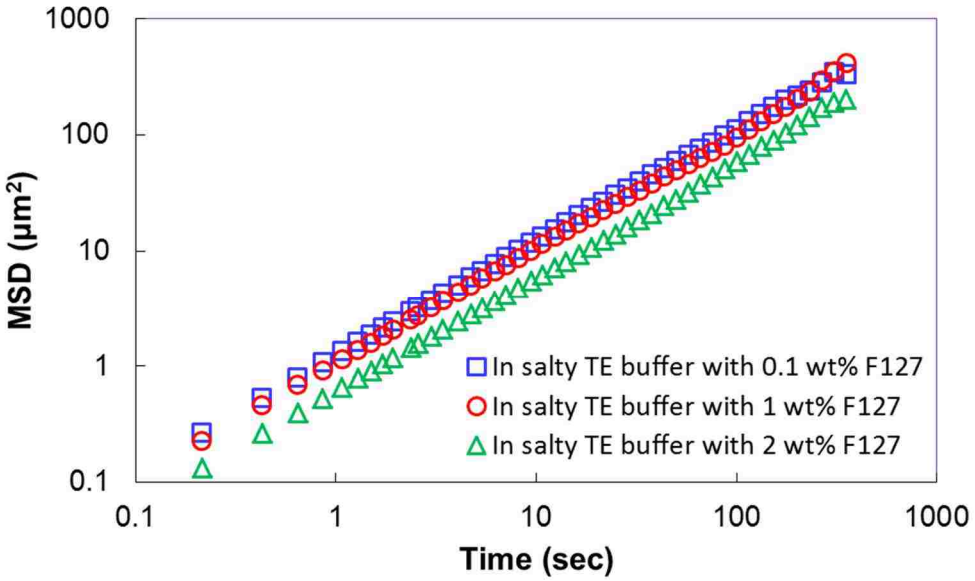

Figure 3.6. The mean square displacement (MSD) log-log plot at 28 °C for the DNA-coated particles in three type of solution: 0.1 wt% F127 in salty TE buffer (square); 1 wt% F127 in salty TE buffer (circle); 2 wt% F127 in salty TE buffer (triangle).

Among the possible interactions, a depletion interaction could be appropriate candidate to understand mechanism of these behaviors of DNA-functionalized particles in salty TE buffer including different concentrations of the nonionic surfactant. It is well-known that the depletion attraction emerges in a system consisting of two significantly different sizes of structures (e.g. nanoparticles, micelles, and polymers) owing to the exclusion of a nonadsorbed smaller structure from the region between larger structures.(*103*) Previously, it is reported that micelles have been used to induce the depletion attraction between spherical particles.(*104–108*) Typically, the depletion interaction can be tuned by concentration of micelles as well as by temperature. Sober and coworkers(*108*) measured the interaction energy between colloidal polystyrene latexes and a flat surface in the presence of charged cetyltrimethylammonium bromide (CTAB) micelles. In this paper, they didn't see any attractive interaction below the CMC of CTAB.

Above CMC, attractive minimum was seen clearly to increase with increasing surfactant concentration, while the distance between the particle and surface decreased. Recently, two groups, Kumar *et al*. and Ray *et al*., reported that charged silica nanoparticles can be clustered due to depletion interaction in the presence of nonionic surfactant (*104*, *106*). Interestingly, Ray and coworkers showed that the nonionic micelles produce micelle decorated core-shell structures by adsorbing on the nanoparticles in absence of salt, but the adsorption of the micelles on nanoparticles is cancelled in the presence of salt, driving the depletion-induced aggregation of nanoparticles. Considering the depletion interaction on charged silica particles with nonionic micelles, we performed control experiments to check the depletion interaction using only αDNA-functionalized particles in different F127 concentrations and temperatures. In this test, we can't find any clustering of αDNA-functionalized silica particles. **Figure 3.7** shows that average of singlet percentage and there is not much difference depending on temperature and surfactant concentration. This result does not simply prove the existence of depletion interaction, but supports specific binding due to the DNA hybridization, as shown in **Figure 2.4**. However, we can make possible mechanism to understand increase of melting transition depending on surfactant concentration. As shown in **Figure 3.5**, the melting transition of DNA-functionalized particles is sensitive to the micelle formation of nonionic surfactant. Here, we assumes that the depletion force by micelles formation exists, as reported by the literatures, and the magnitude of repulsion interaction caused by electrostatic and steric hindrance of DNA might be larger than induced depletion interaction caused by micelles. Hence, only after making DNA hybridization between complementary pairs and thereby driving to overlapping between particles, the effect of depletion attraction might be triggered. In other

word, DNA hybridization might be dominant attraction to make aggregates and depletion attraction might be secondary. The distance between particles after hybridization might become closer according to depletion interaction and thus more DNA hybridization might be induced to get higher melting temperature above CMC. Recently, Srivastava and coworkers (*109*) showed super-compressible DNA nanoparticle lattice, which exhibits isotropic compression in presence of different osmotic pressure dependent on surfactant concentration. In micron-sized particles, this compression might enhance the number of DNA hybridization on the particle surface and thereby inducing increase of attractive interaction between DNA-functionalized particles. However, we need to further study to verify this influence of depletion interaction on melting transition of DNA-functionalized silica particles.

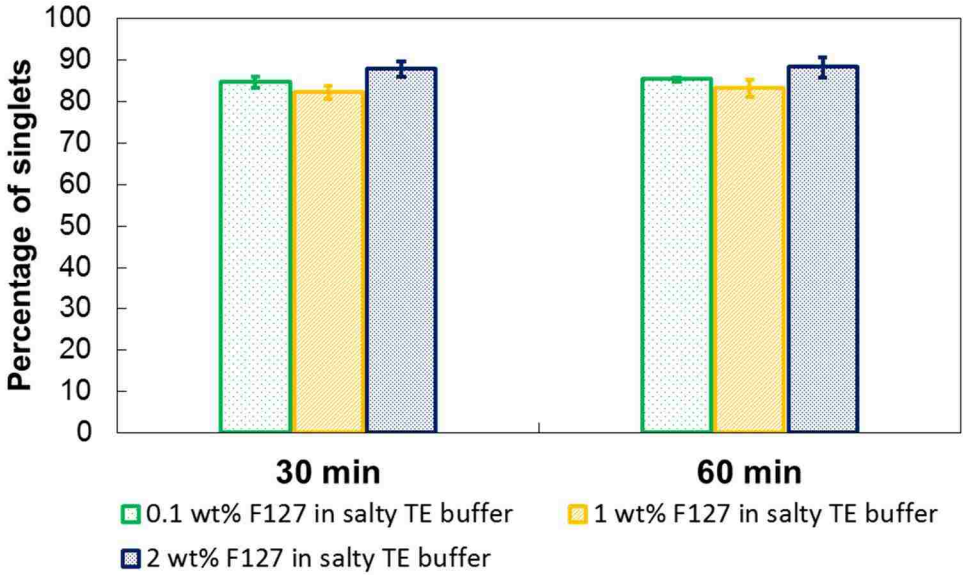

Figure 3.7. The percentage of singlets for αDNA-coated particles in each solution for 30 and 60 minutes. This graph is derived from the overall average of singlet percentage for all temperatures in the range of melting transition.

3.3.5 Evolution of DNA-coated Microparticle Assembly

To study the aggregate evolution of *micron-sized* DNA-mediated silica particles we employ our detailed melting curves to gain mechanistic insight into aggregation and evolution of order as a function of system temperature using *in-situ* optical microscopy of aggregates and singlet. Two temperatures are selected from the melting curve. One temperature is 26 °C, where there is only full aggregates (below the melting transition) and the other is 29.5 °C where the singlet percentage is around 20% (just inside the melting transition) as shown in **Figure 3.4b**. Full dissociation over melting temperature is followed by long-term staying at the target temperatures to see aggregate restructuring.

From this test, we can see the distinction in assembly behavior according to the selected temperatures (data not shown). Below melting transition, pre-existing small aggregates continued to merge with increasing time, finally forming the large branched aggregates without any restructuring. On the other hands, within the melting transition, we can see the association between the aggregates, subsequent dissociation, merging to the large one aggregate and then internal restructuring of the aggregate to more compact structure. Therefore, it is understood that the weak and reversible interaction inside the equilibrium region (the melting transition) is the driving factor to rearrange and restructure the aggregates, and maintaining system temperature at the lower bound of the melting transition region, avoids complete dehybridization toward singlets.

For the clearer visualization of DNA-mediated assembly, *1.5 μm* sized DNA-coated silica particles in the salty TE buffer with 1 wt% F88 have been employed to see the DNA-mediated self-assembly. **Figure 3.8** shows the representative images in this test. Interestingly, we can see the ordered structures after the subsequent cooling without any

careful consideration of annealing procedure (*32*, *45*, *62*) and any special functionalization of the surface (*42*). Without thermal annealing, resulting assembly shows open and disordered structures as shown in **Figure 3.8a**. One component system is achieved by blending αDNA and β (1:1) and resulting assembly is hexagonal lattice as shown in **Figure 3.8b**. Also, square lattice emerges in binary components system.

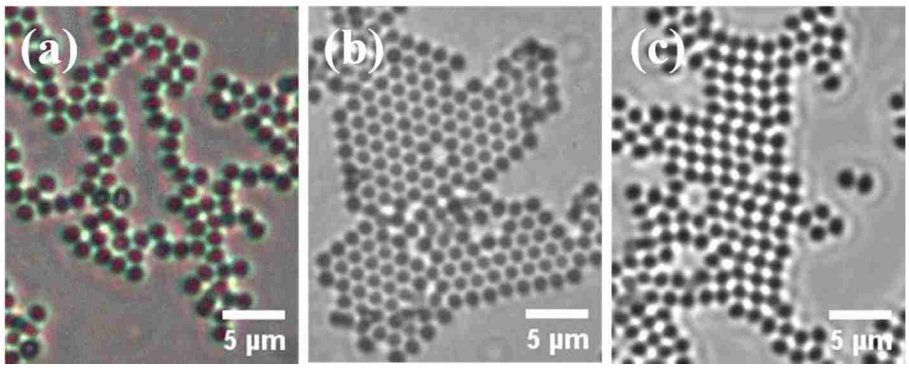

Figure 3.8. The optical images for resulting structures. (a) Open and disordered structures for sample without thermal annealing, (b) hexagonal lattice structure for one component with thermal annealing, (c) square lattice structure for binary components with thermal annealing.

3.4 Conclusion

In this Chapter, we have demonstrated the influence of Pluronic® nonionic surfacants on the association/dissociation transition of micron-sized colloids functionalized with complementary single-stranded DNA as a function of nonionic surfactants concentration (Pluronic® F127 and F88). From the cooling and the subsequent heating process, we have shown that the melting transition of DNA-functionalized silica particles is affected by the concentration of noninonic surfactant according to the formation of micelles. Although further studies will be needed to prove its correctness conclusively, depletion interaction from micelles might allow the particles to get more hybridization and thereby it might result in rise of melting transition above critical micelle concentration at specific temperature. Also, we have investigated DNA-mediated microparticle assembly along with the pre-determined melting profile. Within the melting transition, assembled structures is evolved to ordered structures such as square and hexagonal lattices according to the system. Following Chapter will deal with molecular dynamic simulations for further understanding of these assembly via DNA-mediated interactions.

Chapter 4:

Computational Study of DNA-Mediated Assembly

4.1 Introduction

DNA-mediated particle assembly (*32*, *45–47*, *62*) has shown unique potential for programming a diversity of crystalline arrangements spanning nanometer to micrometer scales due to the selectivity of Watson-Crick base pair interactions and the temperature-dependent control over DNA hybridization. To be more specific, Macfarlane et al.(*94*) demonstrated structural characteristic for a total of 41 crystals that adopted one of nine crystal lattices, which cannot be achieved through other methodologies (*11*, *110*, *111*), by using tunable main two parameters, nanoparticle size and DNA-mediated interactions. Despite significant progress in recent years, two major challenges in DNA-mediated assembly is still going on: 1) realization of low-coordinated lattice structures, such as diamond lattice, in terms of promising application (*20*, *26*, *27*); and 2) further understanding of kinetic barriers(*74*, *112*) in terms of fundamental details.

The key features for DNA-mediated particle assembly relies on how to control interparticle interactions by using temperature-dependent DNA hybridization. The preferred systems to control this interaction have been achieved by not only designing specific DNA sequences(*32*, *36*, *41*) but also controlling the DNA grafting-density on the particle surface (*38*, *39*, *67*). However, most of studies were focused on using conventional

'uni-flavored system', which means that a single type of favorable particle interaction was restricted to in a given assembly. Recently, a few studies demonstrated 'multi-flavored system', which is composed of functionalized particles with more than one type of DNA sequence on the same particles, and so showed the possibility of new aspects of DNA mediated assembly. For example, Wu et al.(*69*) demonstrated the multi-flavored particles, which can connect to four different types of particles, based on theoretical consideration. Employing particles to specifically bind to a particular set of other particles facilitates further design of DNA-mediated assembly for the fabrication of complex crystals. Taking advantage of this strategy, Macfarlane et al. showed additional crystal structures, isostructural with sodium chloride and simple cubic, in binary gold nanoparticle system. Furthermore, Casey et al.(*40*) demonstrated binary colloidal crystals from compositionally ordered crystals with CsCl and CuAu-I symmetries to disordered one through tunable relative attraction strengths between like particle pairs (E_{AA}, E_{BB}) with respect to unlike particle pairs (E_{AB}). Very recently, Zhang et al.(*113*) demonstrated the selective transformations of DNA-nanoparticle superlattices into distinctive structures by input of specific types of strands, such as uni-flavored, multi-flavored and repelling strands, that modify interparticle interactions within the lattice. Whereas majority of the studies so far have focused on three-dimensional (3D) structures (*114*), the progress has been relatively slow in successfully transforming DNA-functionalized particles in diverse two-dimensional (2D) crystal structures.

In this Chapter, we present a comprehensive strategy that makes use of available information on pair interactions between DNA-coated particles from simulation, to calculate the relative stability of various crystal polymorphs as a function of interparticle

attraction strengths. For simplicity, we present theoretical and simulation results on a system of equal-sized particles that can be assembled in two-dimensional (2D) crystalline lattices. The key parameter is the relative attraction strengths between like particle pairs (E_{AA}, E_{BB}) with respect to unlike particle pairs (E_{AB}). First, we use lattice energy calculations to obtain a quick estimate of relative stability of possible crystalline structures, and then use molecular dynamics (MD) simulations to test the predictions of such calculations. MD simulations are also complemented with standard free energy calculations, as needed, to further verify results. We determine the range of E_{AA}/E_{AB} and E_{BB}/E_{AB} values, suitable for assembling particles in square versus hexagonal lattices (alternating string, honeycomb, etc.).

4.2 Methods

4.2.1 Effective Pair Potentials

Our group developed a detailed coarse-grained model of DNA-functionalized particle (DFP), which includes the explicit representation of the grafted DNA strands, to compute the potential of mean forces between two DFPs by varying parameters such as temperature, spacer length, grafting density in a systematic manner (*95*). Here we fit these potential of mean forces (PMF) between two DFPs with a modified continuous Jagla (MCJ) potential, which has three terms to represent the contribution from (1) sphere-sphere repulsion due to volume exclusion, (2) repulsion due to compression of the grafted DNA chains and (3) attraction due to DNA hybridization respectively as follows:

$$U(r) = \epsilon\left(\frac{\sigma}{r}\right)^{n} + \frac{A_0}{1+\exp(A_1 r - A_2)} + \frac{B_0}{1+\exp(B_1 r - B_2)}$$

Figure 4.1a shows one example of comparison between the original data and the fitted MCJ potential. The original data (black circles) is the PMF between two DFPs with each particle grafted by 16, 12-mer long sticky end (TTTTTTATGTATCAAGGT and TTTTTTACCTTGATACAT), DNA strands at temperature T=0.228. In order to improve the fitting quality, we also apply umbrella sampling to obtain additional data points at short contact distances (red circles). The fitted MCJ potential exhibits a very good representation of the original data for a wide range of temperatures (**Figure** 4.1**b**) and grafting density (data not shown).

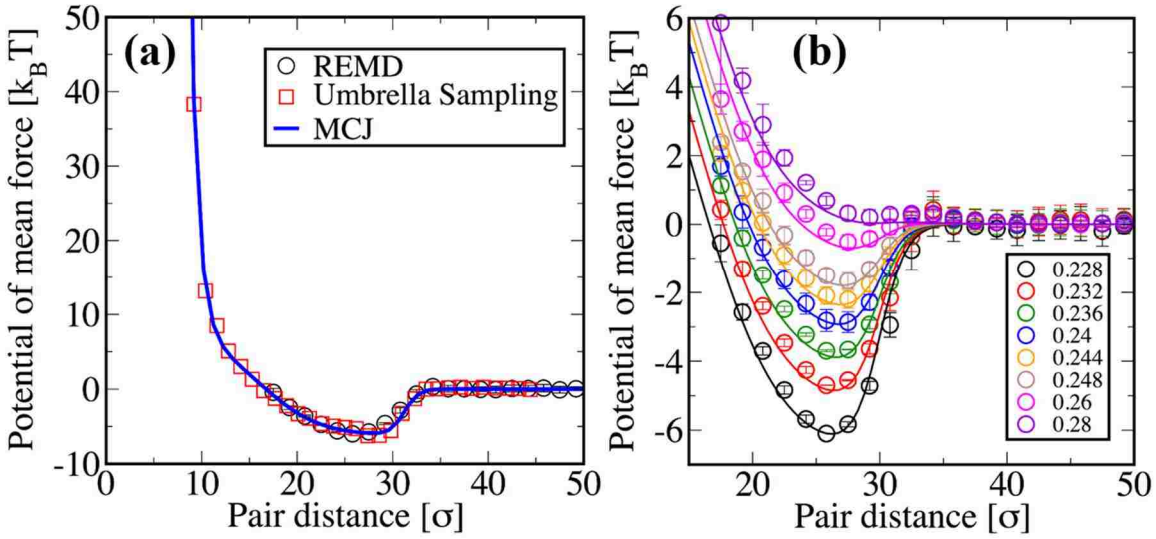

Figure 4.1**. (a)** Fitting of potential of mean force (PMF) between two DNA- functionalized particles with each particle grafted by 16, 12-mer long sticky end, DNA strands at T=0.228. **(b)** Fitting of PMFs as described in the left panel but for different temperatures.

After using the MCJ potential to fit a large amount of PMF data from the previous work. We have the following conclusive points for a specific grafting scheme: (1) Sphere-sphere repulsion, which can be modeled as 12^{th} power repulsive potential, has very weak temperature independence as expected; (2) Polymer-type repulsions between overlapped DNA chains also have very weak temperature independence; (3) Attractive interactions due to DNA hybridization are strongly dependent on temperature; (4) Only single parameter B_0 is needed to capture the temperature dependence of attractive interactions. Therefore, all the parameters related to the sphere-sphere repulsion are only dependent on particle size; all the parameters relevant to polymer-type repulsion is only dependent on the grafting scheme, i.e. number of grafted DNA chains and length and sequences of DNA strands; all the parameters for the attractive portion of interaction except B_0 are dependence on grafting scheme. Only by varying B_0, we can obtain pair interactions at all the temperatures if the particle size and grafting scheme are fixed.

The PMF is essentially for 10 nanometer particles. Although DNA-functionalized microparticles differ from its nano-sized counterpart in terms of DNA-grafting density, particle curvature and length of grafted DNA. The PMF from the previous work resembles the experimentally measured effective pair potentials (*70*). Other simulation (*115*) also confirmed that the differences between micro-sized and nano-sized particle only affect the strength of attraction, albeit the length of spacer, which is the non-hybridized part of grafted DNA, do affect the range of attraction. By considering the above points, we only need to scale our MCJ potential in order to simulate the 1-micron DFPs. The scaled MCJ diverged around 1σ and the attraction range is 0.04σ.

4.2.2 Design of interparticle interaction

DNA-mediated interactions can be programmable through large parameter space: 1) the particles, such as their shape (*33*, *59*), size ratio (*44*, *116*) and stoichiometry (*117*), 2) the oligonucleotides, such as their sequence (*41*), length (*29*, *95*) and surface coverage (*31*, *39*, *70*) and 3) the operating conditions, such as temperature (*70*) and salt concentration (*67*) as well as surfactant concentration (*109*). Most of the previous studies stick to the conventional design of interparticle interactions, 'uni-flavored' system, in which the interactions between like particles (A-A or B-B) are purely entropic repulsive and those between unlike particles (A-B) are enthalpic attractive as shown in **Figure 4.2**. In order to achieve more complex and diverse crystalline phases and applications, an alternative way could be to use 'multi-flavored' particles in which particles are coated with more than one type of DNA sequence (with complementary DNA sequence carried by more than one type of particles), which can be used to further control interparticle interactions. Such multi-

flavored particle systems are attractive from material design standpoint as they can be easily made by using the same material synthesis of uni-flavored one in the laboratory setting (*40*, *44*, *69*). In next Chapter, we will deal with its detailed information how to achieve in our experiment.

For simplicity in the multi-flavored systems, we work with two design strategies of interparticle interactions on a system of equal-sized binary particles (A and B) that can be assembled in two-dimensional crystalline lattices. One is 'symmetric design' of interparticle interactions that leads to the unlike interactions to be stronger than the like interactions and two like interactions to be equal ($E_{AB} > E_{AA} = E_{BB}$), which is symmetric attraction between like particles, as shown in **Figure 4.2**. The other is 'asymmetric design' of interparticle interactions that leads to the unlike interactions to be stronger than the like interactions but two like interactions to be different ($E_{AB} > E_{AA} > E_{BB}$ or $E_{AB} > E_{BB} > E_{AA}$). Taking advantage of available information on pair interactions through our empirical function based on the coarse-grained model of DNA-coated particles with explicit representation of DNA chains, we construct two designs and so demonstrate the relative stability of various crystal polymorphs as a function of interparticle attraction strengths.

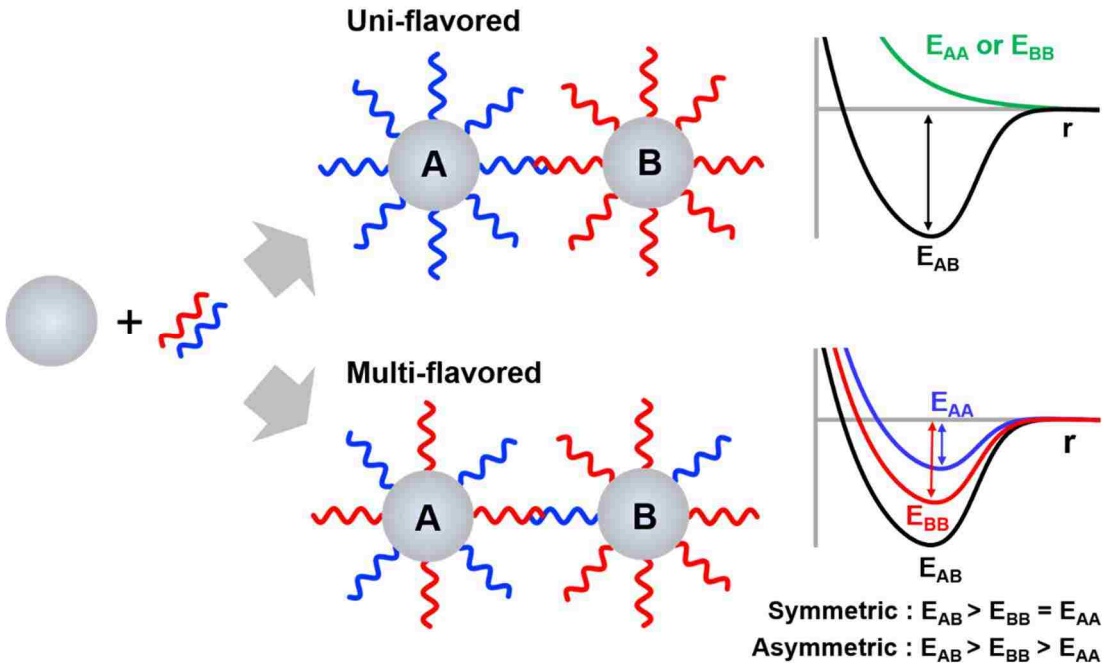

Figure 4.2. The scheme of DNA-coated particles (uni-flavored and multi-flavored) and the strategy to tune the attractive interaction between different particle pairs (A-B, A-A, B-B).

4.2.3 Simulation Details

Molecular dynamics simulations are carried out under the canonical ensemble using a Langevin thermostat with damping parameter = 2 $(\varepsilon/m/\sigma^2)^{-1/2}$ in a 2D simulation box with periodic boundary conditions in x and y directions. As we are interested in crystalline structures stabilized by DNA-mediated interactions (as opposed to entropically stabilized structures at higher density), we perform simulations at a lower density, $\rho = 0.10$. For each simulation, we simulate 400 particles (200 each of A and B type), which are placed randomly inside the simulation box, for 10^8 steps with a step size of $t = 0.001$ $(\varepsilon/m/\sigma^2)^{-1/2}$.

4.2.4 Binary Lattice Analysis

Figure 4.3 shows various 2D crystal lattice structures (square and hexagonal) that appear spontaneously in binary system. The number of nearest neighbors enable to differentiate square and hexagonal lattice. However, it is not sufficient to distinguish each crystal structure in binary system due to possible assignments of each nearest neighbors as either like or unlike particles. For example, alternating string (**Figure 4.3b**) has two green (A) and four red (B) particles as the nearest neighbors but honeycomb lattice (**Figure 4.3c**) has only six red (B) particles.

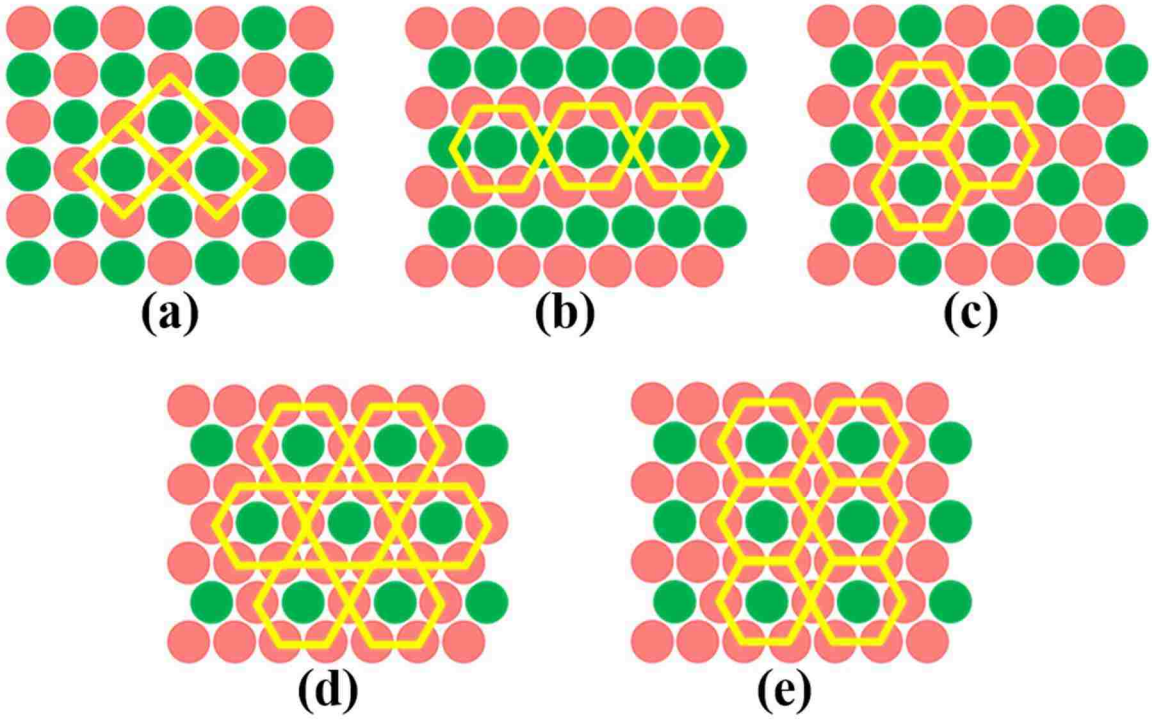

Figure 4.3. Possible 2D crystalline arrangements in binary system with equal size of A (green) and B (red) particles: (a) square lattice; (b) alternating string; (c) honeycomb lattice; (d) kagome lattice; and (e) square kagome.

In order to distinguish and quantify the compositional arrangements in binary system, we calculate average number of bonds, defined as $N_K = \sum n_K^i / 2n$ with K = {AB, AA, BB}, formed for each particle in given lattice according to the number of nearest

neighbors. Here, n is total number of particles based on criteria of nearest neighbors, N^{NN} = 4 or 6, in a given lattice and n_K^i is the total number of bonds (AB, AA or BB) between particle i and its nearest neighbors. The summation is over all the particles in the lattice and the factor of 2 is used to account for the double counting of bonds. **Table 4.1.** shows an average number of contacts as an order parameter for each 2D crystalline structure.

Table 4.1. The average number of contacts formed between unlike (N_{AB}) and like (N_{AA} and N_{BB}) particle pairs for possible 2D crystal lattices.

	$2N_{AB}$	$2N_{BB}$	$2N_{AA}$	$2(N_{BB} - N_{AA})$
Square	4	0	0	0
Alternating string	4	1	1	0
Honeycomb	4	2	0	2
Kagome	3	3	0	3
Sq. Kagome	3	3	0	3

As you can see, the differentiation of these crystal structures can be determined by N_{AB} as well as N_{AA} and N_{BB}. Although the value of N_{AB} is same for square, alternating string and honeycomb as 4, the values of N_{AA} and N_{BB} are different among these lattices. Completely random square and hexagonal lattice with 1:1 stoichiometry by simple probability argument provide 2 and 3 of N_{AB}, respectively.

Differentiating formed binary crystalline structures in 2D, we firstly calculate the average number of nearest neighbors of formed structures to differentiate square and hexagonal lattice. Then, we calculate the average number of contacts formed between unlike and like particles pairs to distinguish further arrangements of the lattices and quantify those compositional ordering.

4.2.5 Free Energy Calculation

For further understanding and verification of crystalline structures formed, solid free energy of the 2D arrangements of interest is carried out using our implicit potential of DNA-coated particles, which is described as the modified continuous Jagla potential (MCJ). The Helmholtz free energy is evaluated through 'Einstein crystal method' proposed by Frenkel and Ladd (*118*). Recently, the Einstein crystal method was extended to GROMACS or LAMMPS widely used open source molecular dynamics simulation programs by Vega et al. (*119*). Here, we calculate the Helmholtz free energy of 2D crystal phase of interest using modified LAMMPS version. In this method, the Helmholtz free energy (A_{sol}) of the 2D arrangements of interest can be described as following three terms:

$$A_{sol}(T,V) = A_0(T,V) + \Delta A_1(T,V) + \Delta A_2(T,V)$$

Here, A_0 is related to the free energy of the ideal Einstein crystal reference system with fixed center-of-mass and the free energy difference between the solid with and without the fixed center-of-mass (*120*). A_0 can be calculated using following analytical expression:

$$\frac{A_0}{Nk_BT} = -\frac{1}{N}\ln\left[\frac{1}{\Lambda^{2N}}\left(\frac{\pi k_BT}{\Lambda_E}\right)^{N-1} A\right]$$

Here, N is the number of particles, Λ is the thermal de Broglie wave length, k_B the Boltzmann constant, A is the area of system and Λ_E the harmonic spring constant. The thermal de Broglie wave length is assumed to an arbitrary convenient value as it doesn't affect to compare the relative difference between arrangements.

Both ΔA_1 and ΔA_2 are calculated by using numerical simulations in LAMMPS according to the method suggested by Vega et al. Firstly, ΔA_1 is the free energy change between an interacting Einstein crystal and a non-interacting Einstein crystal (both with fixed center of mass) and can be computed by following:

$$\frac{\Delta A_1}{Nk_BT} = \frac{U_{lattice}}{Nk_BT} - \frac{1}{N}\ln\langle\exp\left[-\frac{1}{k_BT}(U_{sol} - U_{lattice})\right]\rangle_{Ein-id}$$

Here $U_{lattice}$ is the potential energy of the perfect lattice and U_{sol} is the interparticle potential of the solid. The subscript Ein-id represents ideal Einstein crystal without interparticle interactions. As recommended by Vega et al., we choose Λ_E value that leads to slightly higher ΔA_1 than $U_{lattice}$ (approximately 0.02 Nk_BT). ΔA_2 corresponds to the free energy difference between the interacting Einstein crystal and the solid of interest and can be evaluated by following:

$$\frac{\Delta A_2}{Nk_BT} = -\frac{1}{Nk_BT}\int_{\ln(c)}^{\ln(\Lambda_E+c)} \frac{\langle U_{Ein-id}\rangle_{N,V,T,\lambda}\,(\lambda\Lambda_E + c)}{\Lambda_E}\; d(\ln(\lambda\Lambda_E + c))$$

Taking advantage of the Gauss-Legendre quadrature formula, this function is evaluated based on 15 nodes and weights.

In our free energy calculation of the 2D arrangements of interest, the system size and box shapes are as follow: square lattice, N = 256, square box; hexagonal lattice including kagome lattice, N = 256, rectangular box $L_y = \frac{\sqrt{3}}{2} L_x$; honeycomb lattice, N = 240, rectangular box $L_y = \frac{16\sqrt{3}}{30} L_x$. It is used to calculate the free energy for the 2-dimensionally periodic arrangements for both symmetric case ($E_{AA}/E_{AB} = E_{BB}/E_{AB}$), at $k_BT/\varepsilon = 0.08$, to understand the transformation between square and alternating strings, and asymmetric case ($E_{AB}/E_{AB} > E_{BB}/E_{AB} > E_{AA}/E_{AB} = 0$), at $k_BT/\varepsilon = 0.11$, to understand the formation of honeycomb lattice and coexistence between honeycomb and kagome lattice at higher E_{BB}.

4.3 Results and Discussion

4.3.1 Lattice Energy Based Prediction

Although the progress has been relatively slow in understanding kinetic effect on DNA-mediated assembly (*73*), the empirical design rule based on the ground-state free energy was quite useful to predict and verify the stability of crystalline structures so far (*44*). In our study, we firstly calculate the nearest neighbor binding energy, which is assumed to be dominant owing to short-ranged nature of DNA-mediated interactions, in the possible 2D lattice by using the effective pair interactions derived from coarse-grained model for the lattice-energy based prediction.

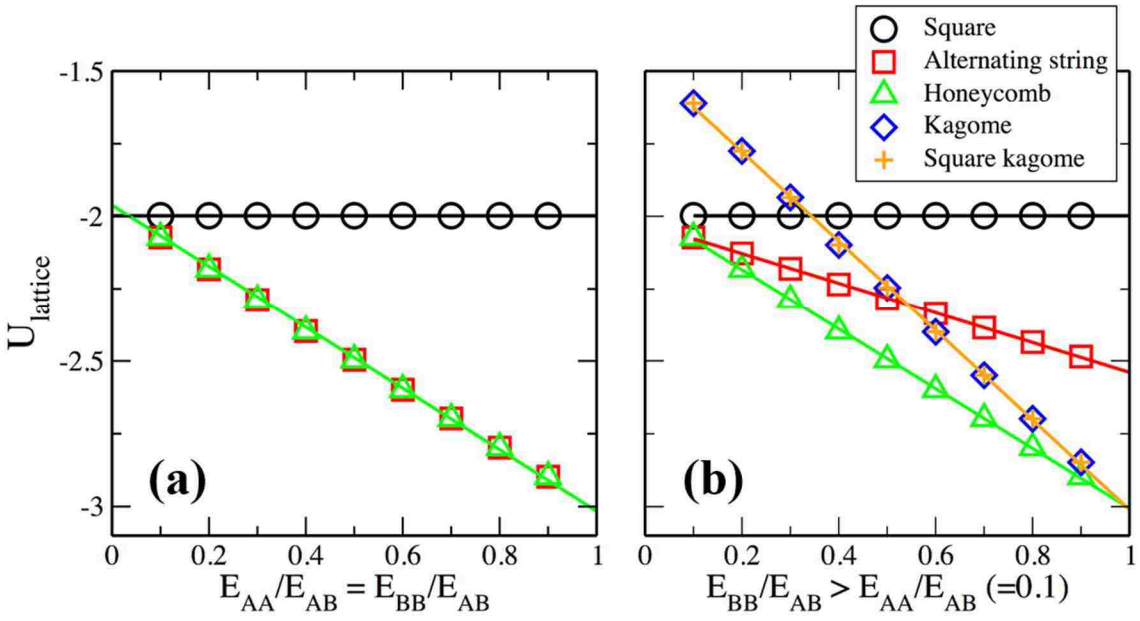

Figure 4.4. Lattice energy obtained by the effective pair potential for the possible 2D lattices as a function of the attractive interactions corresponding the symmetric design between like particles ($E_{AA}/E_{AB} = E_{BB}/E_{AB}$) and the asymmetric design of like particles ($E_{BB}/E_{AB} > E_{AA}/E_{AB}$). Dots are from MD simulation and solid line is fitting line for the results.

Figure 4.4 shows the relative stability of various 2D crystal lattice as a function of the symmetric ($E_{AB} > E_{AA} = E_{BB}$) and asymmetric ($E_{AB} > E_{BB} > E_{AA}$) interparticle

interactions between like particles through simple molecular dynamic (MD) simulation based on the effective pair potential. For the 4-fold coordinated square lattice, each particle possess 4 unlike particles as the nearest neighbors (**Figure 4.3a**). As you can see in **Figure 4.4a**, the lattice energy of square lattice is independent on the value of E_{AA} and E_{BB} since all the like particles don't belong to the nearest neighbors. For the 6-fold coordinated hexagonal lattice, on the other hand, assigned particles with respect to the center particle as the nearest particles can be either like or unlike particles. Different from the square lattice, the hexagonal lattices are dependent on the value of E_{AA} and E_{BB} due to the existence of like particles' contacts. To be more specific, in the honeycomb lattice, the center particle always contacts with unlike particles but these unlike particles contact with their like particles. The lattice energy for the hexagonal lattices, thus, decreases as increasing like particle interactions. Here, the lattice energy for both alternating string and honeycomb is same under the condition of symmetric design of attractive interaction. Hexagonal lattices (alternating string and honeycomb) and the square lattice intersect at $E_{AA}/E_{AB} = \sim 0.03$ based on fitting lines. The square lattice has lower lattice energy comparing with hexagonal lattice below this point, which indicates the square crystals as the stable phase at the ground state, even though the lattice energy between them is expected to be same when $E_{AA} = E_{BB} = 0$ due to the same N_{AB}. This relative stability of the square lattice arises from the fact that the extra like bonds, which stem from overlap of the non-hybridizing DNA chains from nearest-neighbors like particles, increase the lattice energy of the hexagonal lattice.

We also consider the lattice energy for asymmetric design of like particle attractions ($E_{BB}/E_{AB} > E_{AA}/E_{AB} = 0.1$). Interestingly, the lattice energy of honeycomb lattice gets lower

than that of alternating string with increasing E_{BB}. This prediction indicate that asymmetric design of interparticle interactions could be very useful to differentiate two structures. We also calculate kagome and square kagome based on this design. Similar to honeycomb, the lattice energy of them decreases gradually as increasing E_{BB} and finally arrive into similar value to honeycomb at $E_{BB} = 1$.

4.3.2 MD Simulation for Symmetrically Designed Interactions

Following the lattice energy prediction of the possible 2D crystal lattices, we perform standard molecular dynamics (MD) simulations to determine different crystalline phases formed as a function of relative interparticle attraction strength between like particle pairs with respect to the unlike particles pairs according to the symmetric ($E_{AB} > E_{AA} = E_{BB}$) or asymmetric design strategy ($E_{AB} > E_{BB} > E_{AA}$) in the binary system. Here, we apply the empirical function based on our previous simulation results which were obtained with a coarse-grained model of DNA-functionalized particles with explicit representation of ssDNA chains. MD simulations with their various combination of binding energy are initiated with 400 particles with equal number of A and B particles, which are randomly placed in the early stages, as 10% of packing fraction inside simulation box.

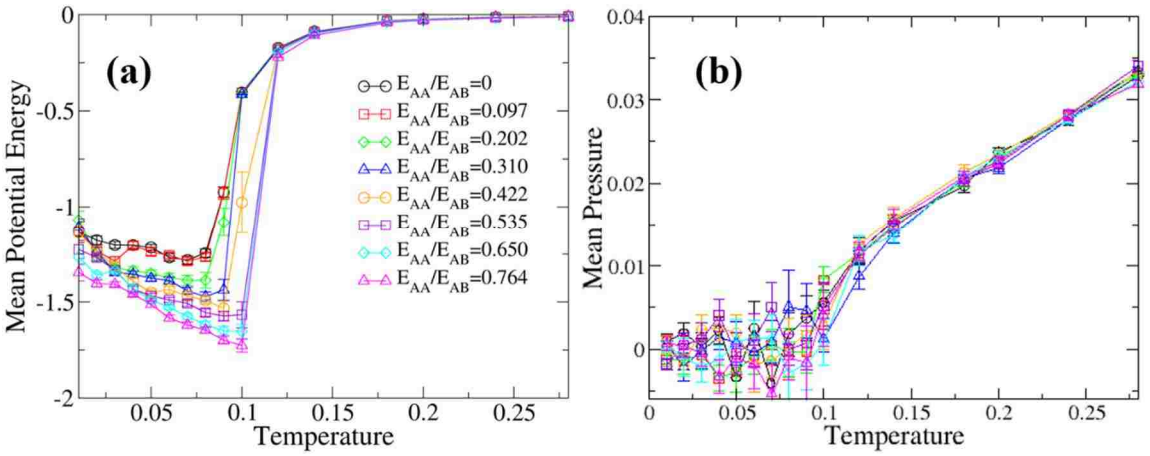

Figure 4.5. Temperature-induced dissociation for symmetrically designed particles ($E_{AB} > E_{AA} = E_{BB}$) with different relative attractive interactions (E_{AA}/E_{BB}) through the variation in average potential energy **(a)** and pressure **(b)**.

We firstly investigate melting temperature based on the variations in average potential energy and pressure as a function of temperature to determine appropriate temperatures to assemble certain crystalline structures. **Figure 4.5a** and **Figure 4.5b** show association/dissociation transitions for symmetrically designed particles ($E_{AB} > E_{AA} = E_{BB}$) with respect to mean potential energy and mean pressure, respectively. Based on these information, we use data for T = 0.08, which is slightly below the melting point for all the relative attractive strengths (E_{AA}/E_{BB}) considered here, for further analysis.

For the quantitative identification of lattice structures (square vs hexagonal), we calculate the average number of particles N^{NN} with a certain number of nearest neighbors (NN) based on a distance cutoff criteria. The resulting data are shown in **Figure 4.6a** for square (NN =4) and hexagonal lattice (NN = 6). For the relatively small relative interactions (E_{AA}/E_{AB} or E_{BB}/E_{AB}), the formed lattice is square lattices. For further increase in E_{AA}/E_{AB} ($=E_{BB}/E_{AB}$), we can see hexagonal lattices. For the quantification of the compositional arrangements with various relative interactions, we calculate average

number of contacts formed between unlike ($2N_{AB}$) and like ($2N_{BB}$ and $2N_{AA}$) particle pairs for a fixed value of NN. As shown in **Figure 4.6b**, all formed square lattices provide unlike particle binding without any like particles binding ($2N_{AB} = 4$, $2N_{AA} = 2N_{BB} = 0$; data for N_{AA} and N_{BB} not shown), which exhibits almost perfect compositional ordering, independent on E_{AA}/E_{AB}. On the other hand, the compositional ordering in a hexagonal lattice is dependent on E_{AA}/E_{AB}. In **Figure 4.6b**, the average number of contacts (N_{AB}) shows slight decrease in intermediate E_{AA}/E_{AB} range (~ 0.18 to 0.6) and steep decrease over the intermediate. To be specific, the calculated value of average number of contacts relatively corresponds to the value for well-ordered alternating string ($2N_{AB} = 4$, $2N_{AA} = 2N_{BB} = 1$) at $E_{AA}/E_{AB} = 0.18$, while the value corresponds to the value for completely random hexagonal lattice ($2N_{AB} = 2N_{AA} = 2N_{BB} = 3$) at $E_{AA}/E_{AB} = 1$. This resultant 2D structures as a function of E_{AA}/E_{AB} shows relatively good agreement with the ground-state free energy prediction as shown in **Figure 4.4a**. However, the free energy calculation based on Einstein crystal method in **Figure 4.6c** provides more precise and reliable criteria to predict and verify the resultant structures through almost same crossing point of E_{AA}/E_{AB} for relative stability between square and hexagonal lattice.

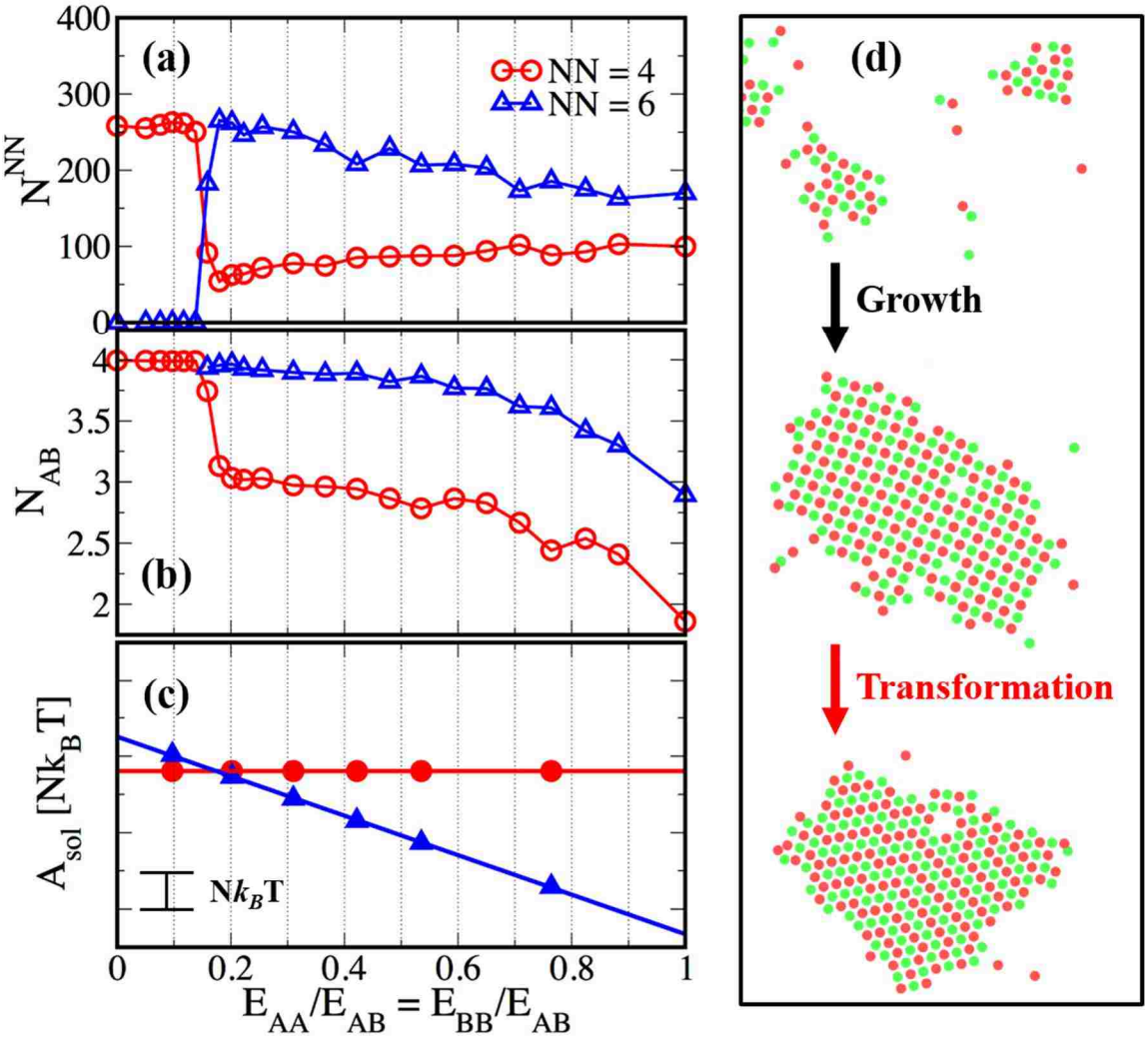

Figure 4.6. Ordering parameters and free energy for binary crystals under the symmetric interactions between like particles ($E_{AB} > E_{AA} = E_{BB}$). For each criterion of square (NN = 4) and hexagonal lattices (NN = 6), (a) the number of nearest neighbors N^{NN} and (b) the order parameter N_{AB} is computed to quantify the ordering of square and hexagonal lattice. The free energy (c) also is calculated as function of relative interparticle interactions. Representative snapshots of square-hexagonal transformation (d) are also shown in this figure.

In addition, at the condition of $E_{AA}/E_{AB} \sim 0.2$, we interestingly observe a transformation from the square to the alternating string as shown in **Figure 4.6d**. To be more specific, small crystal nuclei in this system emerge initially as square lattices, but transformed to alternating-string hexagonal lattice once the square lattices grow up to a

certain critical point. Based on this observation, we perform further simulations to see the effect of the size of square lattices on the transformation of square-hexagonal lattices by using various the relative attractive strengths for the symmetric design of interparticle interactions. Pre-determined configurations as 2D square lattice with different number of particles are investigated in each simulation box with the same packing density (0.10). The resulting data are shown in **Figure 4.7**. To identify this dynamic reconfigurations for each number of particles and relative interaction, we computed average number of nearest neighbors with respect to average number of nearest neighbors at $E_{AA}/E_{AB} = 0$, which is expressed by $\Delta\langle NN\rangle = \langle NN\rangle - \langle NN\rangle_{\frac{E_{AA}}{E_{AB}}=0}$. This data indicates that the transformation of square-hexagonal lattice (alternating string) in 2D is dependent on the size of square lattice as well as the relative attractive strengths. Over a certain number of particles (~70), the relative interaction to trigger the transformation reach to constant value (~ 0.20). In this plot, the extent of blue and red color represents square and hexagonal lattice, respectively. The green color between them represents the critical region to be transformed.

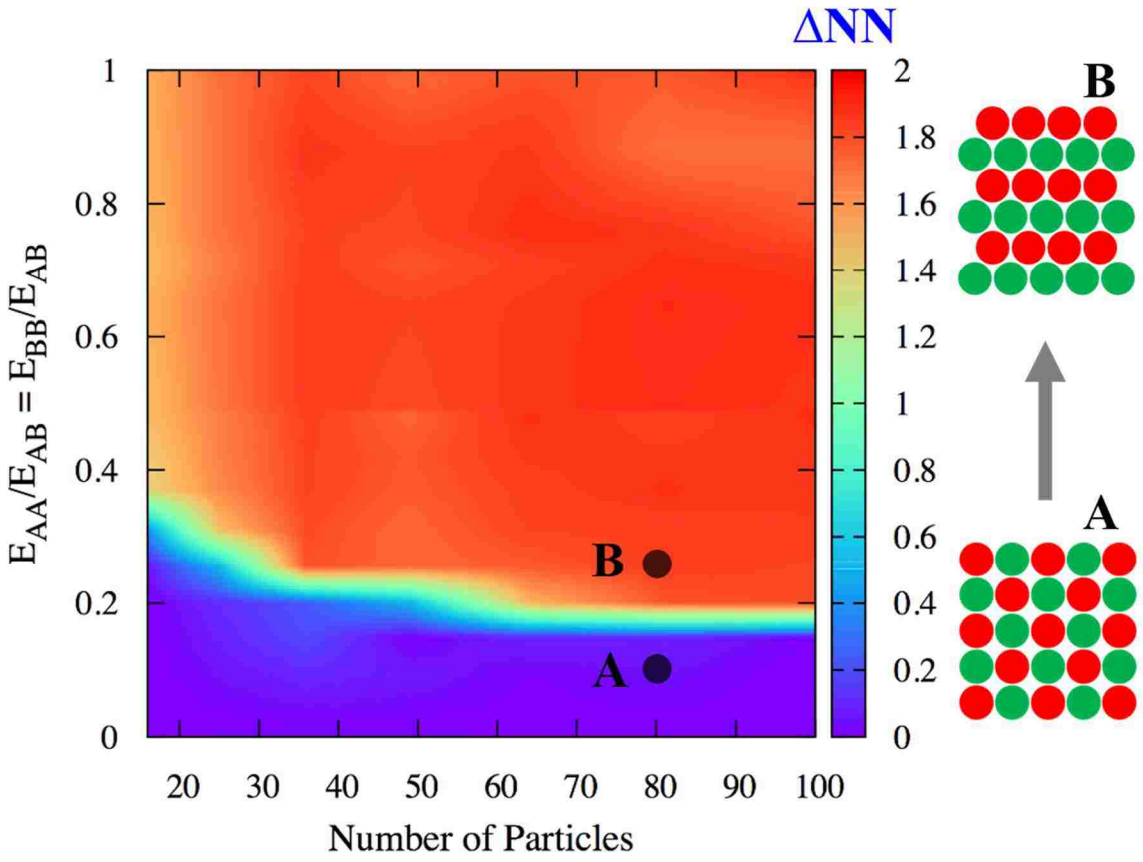

Figure 4.7. The relative stability between square and hexagonal lattice as a function of relative attractive strengths and number of particles in the pre-determined square lattices.

In order to investigate that these size-dependent transformations is kinetically accessible due to the pre-determined square structures, we perform further simulations, in which the pre-assembled hexagonal lattice in the previous run uses as initial structures by simply changing relative interactions preferable to form square lattice. The pre-assembled 49 (or 64) particles as hexagonal lattice in the previous simulation at $E_{AA}/E_{AB} = 0.25$ (or 0.20) performs further simulations by changing $E_{AA}/E_{AB} = 0.20$ (or 0.15), at which the favorable structure is square lattice. As shown in **Figure 4.8**, the hexagonal lattices initially fluctuate slightly at new relative interactions and finally transformed to square lattice as thermodynamic phase, reversibly. This reversibility test allows to confirm that

thermodynamic effects lead to the square-hexagonal transformations as a function of the number of particles and the relative interactions in a given structure. However, this transformations generate kinetic-limitation to hinder the formation of honeycomb lattice that has the same free energy to alternating string (data not shown). In other words, the alternating string structure is quite difficult or impossible to access without this nucleation and transformation process (*121*) in the symmetrically designed particle system. In next section, we deal with how to circumvent this kinetic limitation to achieve honeycomb lattice.

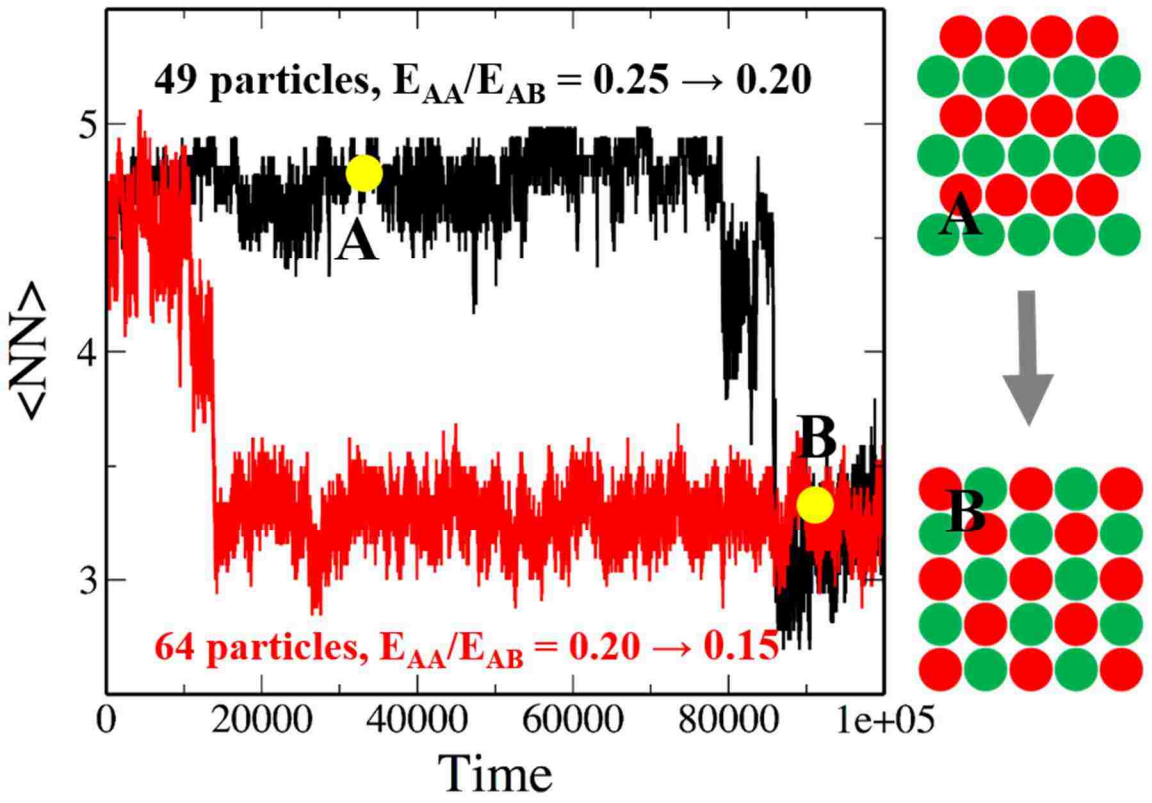

Figure 4.8. The reversibility test of square-hexagonal transformations by using pre-assembled hexagonal lattice and simply changing the relative attractive interactions:

E_{AA}/E_{AB} = 0.2 from E_{AA}/E_{AB} = 0.25 for 49 particles (black) and E_{AA}/E_{AB} = 0.15 from E_{AA}/E_{AB} = 0.15 for 64 particles (red).

Before moving to asymmetric design of interparticle interactions, we discuss about the fact that square lattice shows completely ordered arrangement but hexagonal lattice are subject to a significant compositional disorder under equilibrium conditions. We firstly investigate different temperatures (higher than T = 0.08) as the selection of annealing temperature is critical to form well-ordered structures. However, the different annealing temperatures provide little difference in compositional ordering of binary system due to the constant effective pair potentials with temperature (data not shown). The plausible explanations would be due to the difference in nucleation (related to the transformation) and growth (related to energy penalty with different relative interactions). In case of square lattice, it initiates from square nuclei and then grows under substantially large energy penalty of antisite (*112*), which is defined as a single compositional ordering defect in a binary lattice. As a result, the formed square lattice is highly compositionally ordered structure. Different from the square lattice, hexagonal lattice shows different nuclei depending on the relative attractive interactions, consistent with the presence of polymorphism during nucleation (*122–124*). To be specific, small nuclei emerge as square lattice in the intermediate region of E_{AA}/E_{AB}, whereas they exist as triangular/hexagonal lattice near $E_{AA}/E_{AB} \sim 0.7$ at which most of the lattices are compositionally disordered. For the square nuclei, it grows further and then shows size-dependent transformations to alternating-string hexagonal lattice, which is relatively compositionally ordered, according to the relative interactions. Following these transformations, the compositional ordering can be determined by the size of transformed structure and the energy penalty of antisite. As shown in **Figure 4.6**, the compositional ordering is high at $E_{AA}/E_{AB} \sim 0.2$ as transformed

structures are relatively large and the relatively high energy penalty contribute to growth step. During the growth, alternating-string is competing with honeycomb due to the same lattice energy and free energy, which it can protect the perfect compositional ordering, as well. Then, in range of $0.2 < E_{AA}/E_{AB} < 0.7$, the compositional ordering shows slight decay due to gradual decrease in size of transformation and energy penalty. Beyond the range of $E_{AA}/E_{AB} \sim 0.7$, compositional disordering increases steeply due to the triangular/hexagonal nuclei and little difference in the energy penalty.

4.3.3 MD Simulation for Asymmetrically Designed Interactions

For symmetric design of interparticle interactions, we can see square, alternating-string and random hexagonal lattices. As we discussed in the previous section, the energy difference between like ($E_{AA} = E_{BB}$) and unlike (E_{AB}) particle interactions are critical to create the compositionally ordered phases. As alternative way to form diverse 2D crystal phases, we adopt asymmetric design of DNA-mediated interactions and carry out MD simulations. **Figure 4.9** shows a pseudo-crystal phase diagram under the condition of $E_{AB} > E_{BB} > E_{AA}$, where honeycomb lattice is anticipated based on the lattice energy predictions (**Figure 4.4b**). In low value of the relative interactions around ~ 0.2 of E_{BB}/E_{AB}, we can see perfect compositionally ordered square lattice (A). Interestingly, we find that rhombic lattice (B) is relatively stable between $E_{BB}/E_{AB} = 0.2$ and 0.3, with relatively smaller value of E_{AA}/ E_{AB}. Actually, this rhombic structures can be found for the symmetric design during the square-hexagonal transformation, but it doesn't produce equilibrium state. This also emerges as relatively large structures and so it would be helpful for the formation of large compositionally ordered alternating-string (AS) hexagonal structures, comparing with the AS hexagonal lattice (C) for the symmetric design. For hexagonal structures, we calculate

N_{AB} and N_{BB}-N_{AA} to identify structures and quantify compositional ordering, as shown in **Table 4.1**. From the snapshot of MD simulations, we firstly find honeycomb lattices with less defects for the relatively small value of E_{AA}. As shown in **Figure 4.9b**, the emergence of the honeycomb lattice ($2N_{AB} = 4$, $2N_{BB} = 2$, $2N_{AA} = 0$) is usually located under the condition close to $E_{AA} = 0$. For $E_{BB}/E_{AB} = 0.7$ and $E_{AA}/E_{AB} = 0$, we can find perfect honeycomb lattice (D). However, the compositional ordering for honeycomb lattices decreases and reaches to random hexagonal lattices with increasing E_{AA}/E_{AB} value, which is more critical to determine the ordering rather than E_{BB}/E_{AB} value. In addition, we can see square kagome and kagome structures ($2N_{AB} = 2N_{BB} = 3$, $2N_{AA} = 0$) at relatively high E_{BB}/E_{AB} value (F), coexisting with the honeycomb lattice. The plausible reason for coexistence of kagome and honeycomb structures at high E_{BB}/E_{AB} value would be due to the fact that both free energy and lattice energy between them are getting closer and so they are competing each other (data not shown).

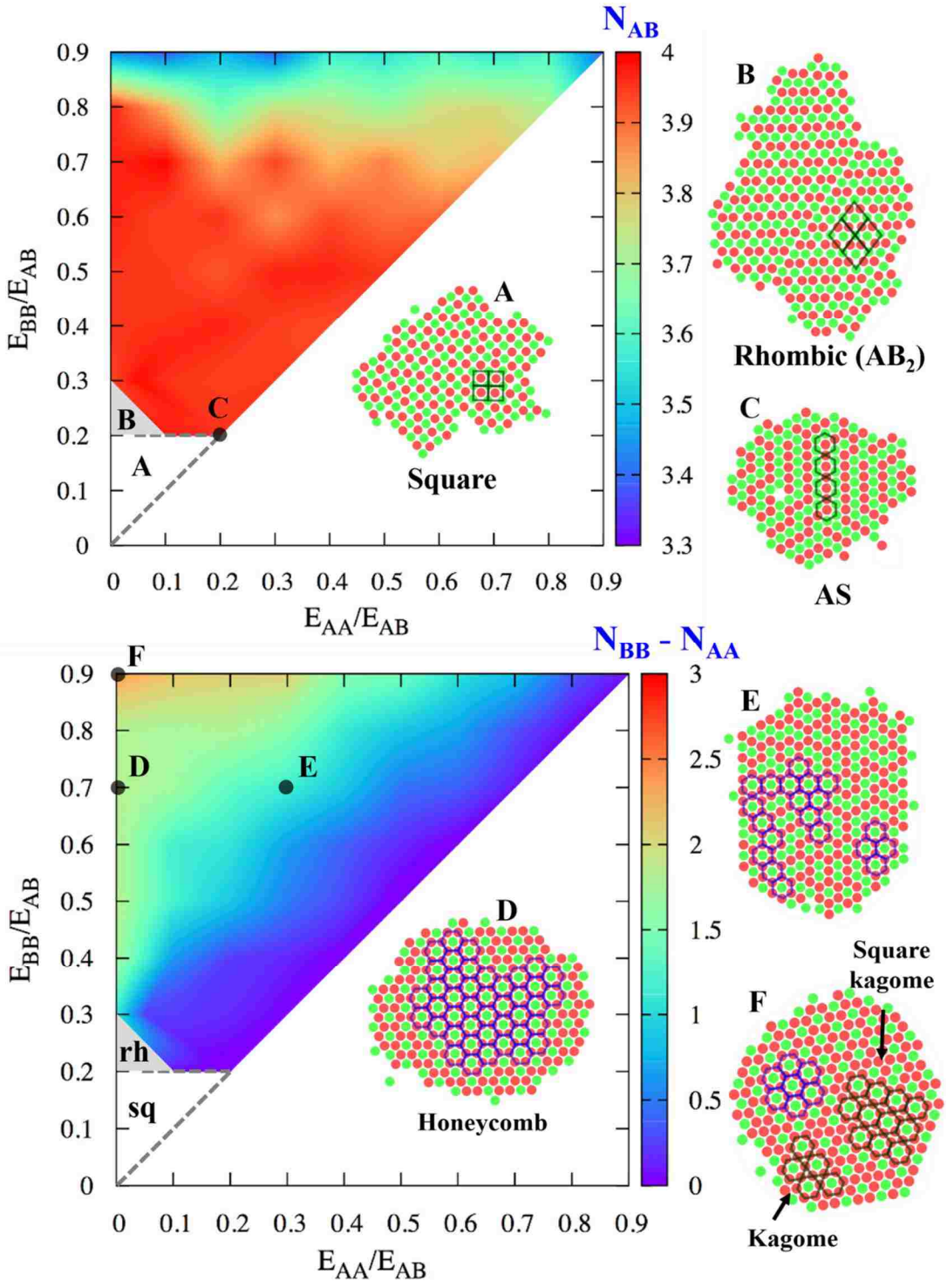

Figure 4.9. Phase diagram and snapshots from MD simulations for binary crystalline lattices under the condition of asymmetric design ($E_{AB} > E_{BB} > E_{AA}$). N_{AB} (upper) and N_{BB}-N_{AA} (below) are calculated for hexagonal phase to identify and quantify the compositional ordering of formed structures.

4.4 Conclusion

In this Chapter, we demonstrate a comprehensive strategy that makes use of available information on pair interactions between DNA-coated particles from molecular dynamics (MD) simulation, to calculate the relative stability of various crystal polymorphs as a function of interparticle attraction strengths. As a result, a diversity of 2D crystalline arrangements is accomplished by interplay of like (A-A, B-B) and unlike (A-B) interactions. Here, these are largely attributed to the employment of 'multi-flavoring' concept for various 2D crystalline lattices, not conventional 'uni-flavoring'. This study shows that resultant crystal phases are largely determined by how to design 'multi-flavored' system: (1) symmetric and (2) asymmetric design of like particle interactions.

In addition, we demonstrate the square-hexagonal transformation and its dependence on the size and relative interaction of formed square lattices. Reversible stability of transformed structures (square to hexagonal and hexagonal to square) according to the relative interactions shows that transformation would be thermodynamically driven. Different size of transformation according to relative interactions allows further understanding of nucleation and growth of final structures. Also, we also observe that the mixing ratio of particles has no meaningful effect on compositional ordering of crystalline lattices. However, due to the slow kinetics, the mixing ratio can play an important role in determining the final structures as observed from our experimental study.

Chapter 5:

Experimental Study of DNA-Mediated Assembly

5.1 Introduction

The nanoparticle-based three-dimensional (3D) assembly via this strategy realized a diversity of crystalline morphologies by taking advantage of main parameters relevant to particle size and DNA, its length and coverage on each particle (*32*, *44*, *45*, *125*). However, the parameters and design rules are not able to be extended completely on the other size of spectrum, micrometer scale, due to relatively short-range interaction with respect to particle size(*32*). Actually, it is quite difficult for DNA-microparticle system to fabricate ordered phases due to its strong attraction and narrow temperature window to find right condition (*27*, *37*, *39*). This influence of particle size on DNA-mediated interaction becomes rather slower to develop diverse crystalline assemblies in micrometer scale, albeit the first observation of crystalline structures was conducted by using the microparticle with special DNA coupling chemistry (*72*). Recently, peculiar approach exploiting both tunable 'like' and 'unlike' particle interactions in binary system, different from conventional approach that use only 'unlike' particle interaction, by changing mixing ratio of two different DNA strands on each submicron-sized particle was successful to form compositionally ordered crystals with two symmetries, CsCl and CuAu-I(*40*). Still, the feasibility of this strategy in micrometer scale has not been explored in order to increase

diversity of DNA-programmable microparticle assembly, even though there existed noticeable reports to overcome the limitations, which the introduction of surface mobile linker(*42*) or DNA displacement(*43*) enable to widen equilibrium window. Considering that microparticles are desirable as their lattice spacing is comparable to the wavelength of visible light (*20*), it is essential to carry on increasing a diversity of well-defined crystalline structures via DNA-mediated microparticle assembly.

The study for two-dimensional (2D) DNA-mediated particle assembly are largely classified into three categories: (i) the fundamental understanding of DNA-mediated assembly, such as a quantitative model of association/dissociation transition (*37*, *38*); (ii) the formation of DNA-functionalized particle monolayer on an patterned surface with complementary ssDNA strands (*76–79*); (iii) the hexagonal lattice of DNA-functionalized particles using different interactions without exploiting DNA hybridization (*80*, *81*). In case of 2D DNA-mediated particle assembly on the patterned substrate (*76–78*), only surface-particle interaction was activated and thus the ordered structures on an ordered pattern of surface is predominantly caused by the template, not particle-particle interaction. The introduction of different length of 'DNA liker' to induce lateral ordering controlled interparticle distance, whereas there was no additional ordering. Template-free 2D hexagonal lattice was observed in separate two study. However, these were not driven by specific and reversible DNA hybridization, one was driven by density and the other was driven by non-specific binding. Very recently, DNA-functionalized nanoparticles showed 2D phase transformation from hexagonal lattice to disordered network structures at positively charged lipid layer by controlling interparticle attraction depending on monovalent salt concentration. Despite various approach, there is no report according to

diverse 2D crystalline morphologies by using DNA-mediated interaction unlike other strategy, such as electrostatic self-assembly (*83*) or self-assembly by Ising interaction (*84*)

In Chapter 5, we present representative experiments using DNA-mediated interactions to test the preceding MD simulation prediction guided the 2D assembly of microparticles into diverse crystal structures. We work with asymmetric design of interparticle interactions which shows various crystal phases, such as square and hexagonal lattices (honeycomb, kagome and square kagome). Microparticles are functionalized by tailored mixture of two different, partially complementary DNA strands (αDNA, βDNA). Here, we demonstrate that attractive interaction strengths can be tuned by controlling particle 'flavoring' via control of the ratio of αDNA, βDNA determined by the simple statistical mechanics for adopted relative attractive interactions from MD simulation. Also, we present the effect of particle number ratio on DNA-mediated particle assembly in 2D. As a result, by using an optical microscope, we observe particles arranged in square, pentagonal and hexagonal structures, which are compositionally ordered in desirable honeycomb as well as kagome lattices.

5.2 Methods and Materials

5.2.1 Particle Functionalization

Green and red fluorescent 1.5-micrometer-diameter silica particles (micromod Partikeltechnologie GmbH, Germany) are functionalized with single-stranded 5'-primary amine modified DNA, ssDNA (αDNA and βDNA in **Table 2.1**; Integrated DNA Technologies, Inc), using silanization and cyanuric chloride chemistry as reported previously (*88*). The detailed information of functionalization and further characterizations is in Chapter 2. Following is focused on how to control the interparticle interactions in this experiment.

Figure 4.2 in the previous chapter outlines the schematic of our strategy to control the attractive interaction strength between different particle pairs (A-A, B-B, A-B), which can also be easily translated to a laboratory experiment. We consider two ssDNA sequences (αDNA, βDNA) that can hybridize with each other but not with themselves with an associated hybridization free energy. If the particles of type A and B are coated with ssDNA α and β, respectively, unlike particle pairs can reversibly bind due to DNA hybridization but the like pairs cannot bind ($E_{AA} = E_{BB} = 0$). One can induce binding between like particle pairs by grafting ssDNA sequences α and β on the same particle(s); the strength of unlike versus like attraction can therefore be controlled by the relative fraction of the two ssDNA. We note that the same ssDNA blending strategy can also be applied to more than two ssDNA sequences or by adding non-hybridizing (inert) ssDNA, thereby allowing further control on interparticle interactions.

For the experimental realization of a diversity of 2D crystal phases as predicted in the MD simulation, we modulate the asymmetrically designed interparticle interaction,

here $E_{AB} > E_{BB} > 0$ and $E_{AA} = 0$, by blending two different DNA. Specifically, 'B' particles are functionalized by blending different ratio of two complementary DNA strands, 'αDNA' and 'βDNA', on particle surface. On the other hand, 'A' particles are functionalized by only αDNA. This asymmetric functionalization enables to modulate two different attractive interaction, E_{AB} and E_{BB}, with remaining constant as $E_{AA} = 0$, which leads to asymmetric attraction between like particles (AA or BB pairs).

5.2.2 Binding Free Energy Estimation

It is essential to estimate the binding free energy as a function of blending ratio of DNAs on the particle in order to carry out experiments based on the previous simulation results. Based on the previous simple statistical mechanics (*37*, *68*), we modify partition function to be applied to the case of blending of DNA on the particle and then estimate relative attractive interactions based on below formula. Suppose N_{DNA} is total number DNA per a particle. $N_{A,\alpha}$ is number of α DNA on a particle A. $N_{B,\beta}$ is number of β DNA on the particle A. $N_{B,\alpha}$ is number of α DNA on a particle B. $N_{B,\beta}$ is number of β DNA on the particle B. The possible maximum number of bonds can be formed by A and B particles is:

$$N_m = \theta \left[\min\left(N_A^{\alpha}, N_B^{\beta}\right)\right]$$

$$N_n = \theta \left[\min\left(N_A^{\beta}, N_B^{\alpha}\right)\right]$$

where θ is ratio between adhesion area $S = \pi r(2L - h)$ and particle surface area $A = 4\pi r^2$. ϕ is ratio between hybridization area $H = 4\pi[L^2 - (h/2)^2]$ and particle surface are $A = 4\pi r^2$. h is surface separation and L is length of DNA.

$$Z = \left[\sum_{N=0}^{N_m} \binom{N_m}{N} \left[\phi \max\left(N_A^{\alpha}, N_B^{\beta}\right)\right]^N e^{-N\Delta G/k_B T}\right]\left[\sum_{N=0}^{N_n} \binom{N_n}{N} \left[\phi \max\left(N_A^{\beta}, N_B^{\alpha}\right)\right]^N e^{-N\Delta G/k_B T}\right]$$

$$= \left(1 + \phi \max\left(N_A^{\alpha}, N_B^{\beta}\right) e^{-\Delta G/k_B T}\right)^{N_m} \left(1 + \phi \max\left(N_A^{\beta}, N_B^{\alpha}\right) e^{-\Delta G/k_B T}\right)^{N_n}$$

Therefore, the binding free energy is

$$\Delta F = -k_B T \ln Z$$

5.2.3 Sample Preparation

Heterogeneous or homogenous suspensions of desired composition and ratio of particle number are prepared by mixing of stock suspensions after washing and redispersion by 100 mM NaCl TE buffer including 0.1 wt% of Pluronic F88 (BASF), which enables the particles to protect non-specific binding between the particles and move freely on glass surface. Microchamber is composed of plasma-treated two coverslips bonded together by melting and solidification of parafilm (~ 250 μm thickness). One of four sides is open to load sample suspension to the chamber. The chamber is sealed by UV-curable optical adhesive (Norland 63) after loading of the desired sample suspension.

5.2.4 Melting Curve

Essentially two-dimensional suspension can be applied to measure melting curve due to high specific weight of silica particles. Samples are prepared by loading unary (B particle) or 1:1 binary (A and B particles) mixture of particles in the microchamber. Surface concentration of the particles is approximately 0.01 particle/μm^2. A Peltier thermoelectric module (TE Technology, Inc) driven by a dipolar thermoelectric temperature controller (TE Technology, Inc) allows to control the sample temperature. The thermoelectric module

with a center hole is attached on a sapphire window (Base Optics), which is placed on top of the sample chamber using thermally conducting paste (TECHSPRAY), by silicone vacuum grease. Five independent images are taken by an inverted optical microscope (Nikon Eclipse TE2000U) a ×60 using air-immersion objective to get each average data point. The singlet percentage, defined as amount of unbound particles on the surface through dividing singlet area by total area of particles, is determined by common microscopy methods(*37*, *100*). Melting curve measurements are done by slow cooling through 15-minutes equilibration at each temperature above and below transition region and 30-minutes equilibration in the transition region to conservatively ensure establishment of equilibrium in this critical range. Melting curve generated by subsequent heating provides almost similar one.

5.2.5 Colloidal Crystallization

Each sample chamber including binary mixture of suspensions (A and B particles) with desired ratio of particle number and relative attractive interaction is attached onto block of PCR machine (DNA Thermal Cycler 480, Perkin-Elmer) using silicone grease and incubated to form crystal structures at specific temperature history. The surface density of particles is 0.08 or 0.16 particle/μm^2. The temperature is initiated above melting temperature (~ 45 °C) where most of particles exist as unbound particles and then decreased at 1 °C intervals of temperature to room temperature where all particles are bonded together. Each temperature remains constant for ~ 4 hours. Resulting two-dimensional structures are observed by fluorescence mode of the microscope (Nikon Eclipse TE2000U) using a ×60 oil-immersion objective.

5.2.6 Image Processing and Pair Correlation Function

All image analysis are based on the image processing routines developed by Crocker and Grier and code developed by Eric Weeks and implemented in the software package IDL (Exelis Visual Information Solutions). The pair correlation function with respect to all particles (A and B particles) is calculated from independent bright-field images. Both pair correlation functions with respect to green (A) or red (B) particles are calculated from independent fluorescent images.

5.3 Results and Discussion

5.3.1 Asymmetric Design of Interparticle Attractions

Green and red fluorescent 1.5 μm diameter silica particles, 'A' and 'B', were functionalized with complementary single-stranded DNAs using silanization and cyanuric chloride chemistry as reported previously (*88*). Attractive interaction to form DNA-mediated assembly can be modulated by the physical properties related to particles and DNA (*95*, *115*). We programed the different attractive interaction strengths by changing blending ratio of two different DNAs only for one species of particle to achieve desired 2D morphologies and their compositionally ordered arrangements through the MD simulations. Specifically, 'B' particles are functionalized by blending different ratio of two complementary DNA strands, 'αDNA' and 'βDNA', on particle surface. On the other hand, 'A' particles are functionalized by only αDNA. This asymmetric functionalization enables to modulate two different attractive interaction, E_{AB} and E_{BB}, with remaining constant as $E_{AA} = 0$, which leads to asymmetric attraction between like particles (AA or BB pairs).

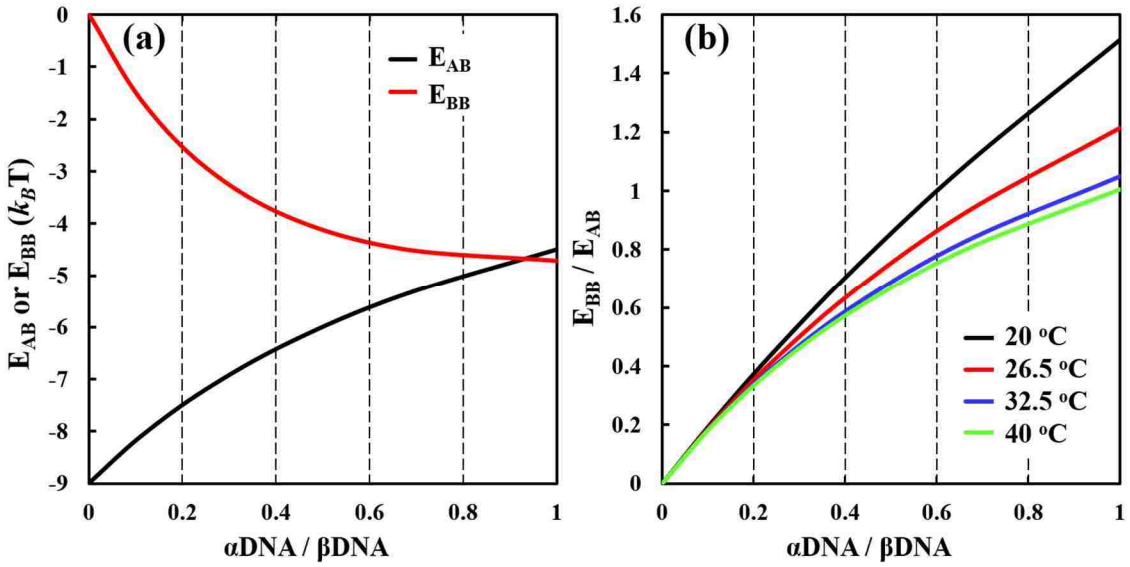

Figure 5.1. The binding free energy estimated by simple statistical mechanics approximation as a function of blending ratio of αDNA and βDNA on 'B' particle in this study. (a) The binding free energy between unlike particles (A-B) or like particles (B-B) at 32.5 °C near melting temperature obtained experimentally. (b) The relative interparticle interactions (E_{BB}/E_{AB}) depending on four different temperatures. Here, we adopt the relative interparticle interactions at 32.5 °C for further experiments guided by MD simulations.

To combine the outcome of simulations with experiments, it is essential to estimate the binding free energy as a function of blending ratio of DNAs on the particle. The estimation of the attractive interaction is based on simple statistical mechanics approximation (*38*) (see Methods for details). **Figure 5.1a** shows attractive interaction strengths between unlike (A-B pair) and like (B-B pair) particles depending on blending ratio of αDNA to βDNA for the B particle with specific parameters, such as temperature (32.5 °C) and effective DNA chains (~ 9000 per particle). The attraction between unlike particles decreases monotonically, while attraction between like particles increases with increasing the fraction of βDNA on B particles and thus the gap between them converges on one point ($E_{AB} = E_{BB} \sim -5$). The attraction between two different particles (A-B pair) is

designed to be stronger than identical particles (B-B pair) to circumvent particle segregation (*73*). To confirm tunability of interparticle attraction based on the asymmetric design, we measured melting transition of DNA-functionalized particles. As we expected, the melting transitions shift to higher temperatures in order of the strength of attractive interaction illustrated in **Figure 5.1a** (data not shown). In order to select appropriate blending ratio according to the simulation outcome, we calculate the relative interparticle interaction (E_{BB}/E_{AB}) as a function of blending ratio for different temperatures. The relative attractive strengths increases with decreasing temperature. Considering weak binding regime of the binding free energy to facilitate for rearrangements of particles and measured melting temperature as a guideline, we choose the relative interactions for 32.5 ^{o}C, which the trend of the relative interactions is comparable to the previous literature (*40*), to get appropriate blending ratio of two DNA chains on the particles. Guided by the ordering diagram for asymmetrically designed interactions in **Figure 4.9** and the relative interactions depending on blending ratio in **Figure 5.1b**, we synthesize DNA-coated particles with three blending ratios (αDNA/βDNA = 2/8, 3/7 and 4/6). For control study, we also prepare two additional blending (αDNA/βDNA = 0/10 and 5/5).

Sample chambers with the particles with different compositions (by different mixing ratio between αDNA and βDNA on B particles) and particle number ratio between A and B particles were prepared with surface concentration of 0.08 or 0.16 particle/μm^2. Before loading solution with desired particle-mixing ratios to the chambers, stock solution was redispersed in salty TE buffer including Pluronic F88, which is essential for the particles to be freely moved on surface without any non-specific binding. Then, the chambers were incubated on the block of PCR machine at pre-designed temperature history

(see Methods for details). Sequential decrease of temperature from 45 °C gave rise to formation of DNA binding between unlike (AB pairs) or like particles (BB pairs) near melting transition (26.5 °C ≤ T_m ≤ 31.5 °C) and finally allowed to evolve into solid state from fluid state at room temperature. Two species of DNA-functionalized particles produced essentially two-dimensional structures due to high specific weight of silica particles. Therefore, we were able to observe a diversity of 2D crystal structures readily by optical or fluorescence microscope.

5.3.2 Crystal Morphology

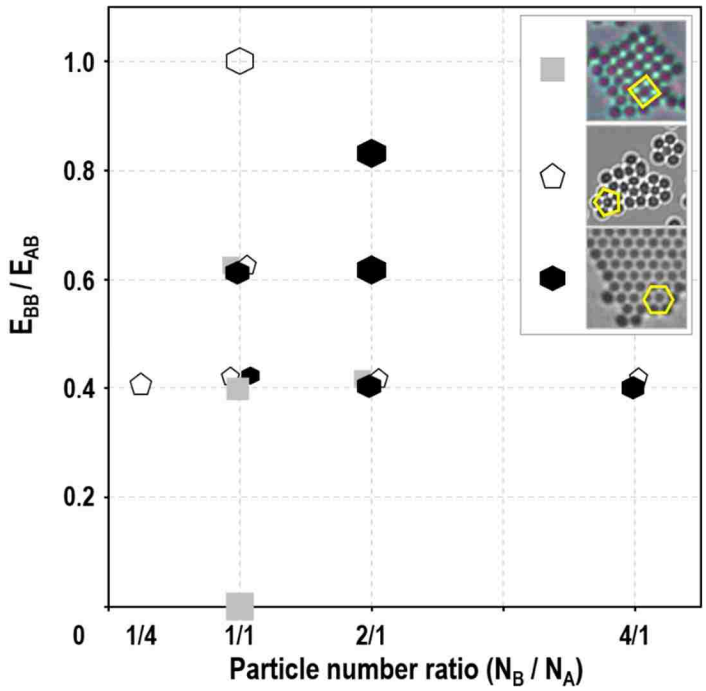

Figure 5.2. Phase diagram representing formed 2D structures for different particle number ratio and relative attraction (E_{BB} / E_{AB}). Depending on ratio of particle number and relative strength of interaction, various 2D structures form, including square (symbolized by grey squares), pentagonal and hexagonal lattice (marked by open pentagons and black hexagons, respectively). For some combinations, mixture of these three structures can be observed. In these cases, the structure that is formed most often is indicated by the front symbol.

Morphological changes according to the relative attractive interaction (E_{BB}/E_{AB}) and particle number ratio (N_B/N_A) are observed by an inverted optical microscope at room temperature after completion of thermal annealing. The phase diagram in **Figure 5.2** illustrates square, hexagonal lattice and pentagonal aggregates that result from the combination of the relative interparticle attraction and particle number ratio. Considering the structural changes dependent on the attraction between particles when the ratio of the numbers of different types of particles is around 1:1, square lattice emerges predominantly at $E_{BB}/E_{AB} = 0$ ($E_{AA} = E_{BB} = 0$). This might be due to the fact that enthalpic binding between unlike particles and entropic repulsion between like particles occur. On the other hand, formed structure at $E_{BB}/E_{AB} \sim 1$ (homogeneous B particles) is extended hexagonal lattice through unary crystallization. Between $E_{BB}/E_{AB} = 0$ and $E_{BB}/E_{AB} \sim 1$ at this mixing ratio of particles, we can observe coexistence of square, pentagonal and hexagonal assemblies. The extent of hexagonal lattice tends to increase with increasing attractive interaction between B particles. Similar tendency for structural changes to hexagonal lattice occurs at $N_B/N_A = 2$ with attractive interaction, but higher number of B particles leads to full hexagonal lattice in earlier stage of the strength of attractive interaction. The pair correlation function for each relative attractive interaction at constant $N_B/N_A = 2$ ($N_B/N_A = 1$ in case of $E_{BB}/E_{AB} = 0$ and αDNA/βDNA = 5/5), as shown in **Figure 5.3a**, shows that the peaks corresponding to 2D hexagonal lattice (especially, $r/D = \sqrt{3}$) are enhanced as attractive interaction increases. These observations suggest that enhanced 'like' particle interaction leads to the formation of a 2D close-packed assembly.

With constant interparticle attraction ($E_{BB}/E_{AB} = 0.41$), we also observe 2D morphological evolution dependent on particle number ratio (N_B/N_A). Due to asymmetric

design for like particles attraction, resulting structures show different evolution based on reference point, N_B/N_A= 1. In right-hand side, the primary structure is changed from square to hexagonal lattice with increasing particle number ratio. For N_B/N_A= 4/1, most of formed structures are hexagonal lattice. The pair correlation function for three different particle number ratios (N_B/N_A= 1/1, 2/1 and 4/1) shows that hexagonal character becomes stronger with increasing particle number ratio, as shown in **Figure 5.3b**. The increasing number of B particles, which can be bound with both A and B particles, shows similar structural changes to the increasing relative attractive strength. In contrast, for N_B/N_A= 1/4 in left-hand side of the reference, local pentagonal aggregates are predominant structures. This might be due to the entropic repulsion between A particles. It is suggested that the formation of desired structures can be modulated by the balance between attractive and repulsion interaction as well as particle number ratio.

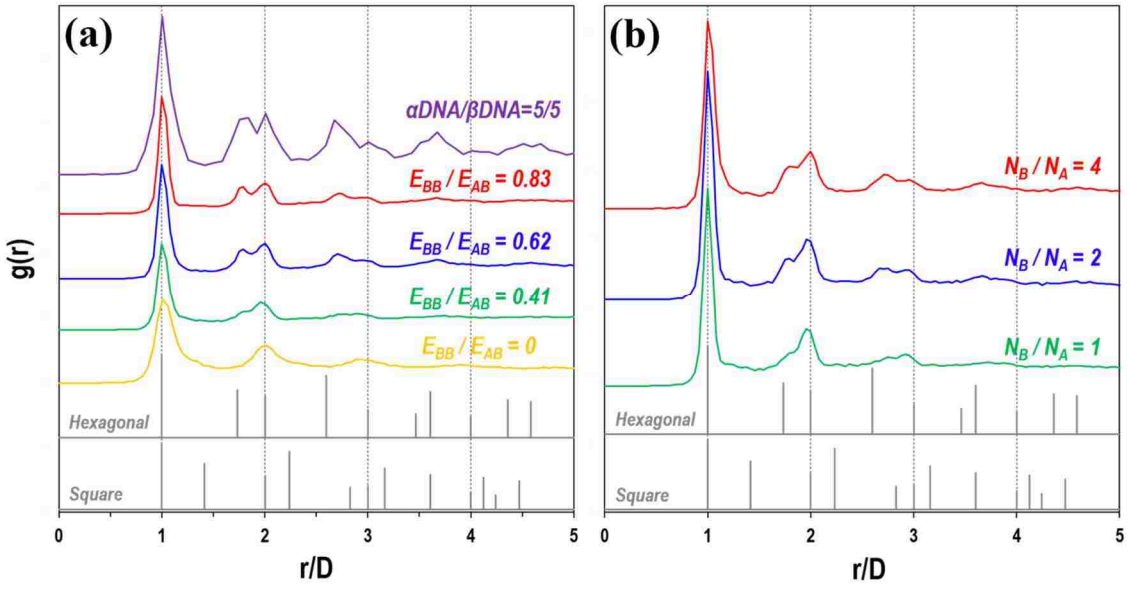

Figure 5.3. Pair correlation function for all particles in bright-field images depending on (a) relative attractive interactions at constant N_B/N_A = 2 and (b) particle number ratio at constant E_{BB}/E_{AB} = 0.41. Grey lines represent perfect square and hexagonal lattice.

5.3.3 Compositionally Ordered 2D Arrangements

Along with observation of 2D structures, we investigate compositional ordering of formed structures depending on relative attractive interaction and particle number ratio by a fluorescence microscopy. For better visualization, primary images are taken by red fluorescence with bright-field mode and secondary ones are taken by green fluorescence mode. The representative images for the formed structures with different particle number ratio are illustrated from **Figure 5.4a** to **Figure 5.4d**. In this case, surface concentration and relative attractive interaction of the samples is 0.08 particles/μm^2 and 0.41 (αDNA/βDNA = 2/8), respectively. For N_B/N_A = 1/1, we can see square lattice (**Figure 5.4b**), which is mostly compositionally ordered. When A particles are present in excess, we can observe pentagonal assembly (**Figure 5.4a**), which shows that each B particle is surrounded by five A particles, as there exists entropic repulsion between two A particles functionalized only αDNA. On the other hand, when we mix the two species of particles in N_B/N_A = 2/1 and 4/1 ratio, the hexagonal lattice forms preferentially, albeit there is coexistence with square and pentagonal structures as there exists lower but still influential entropic repulsion between B particles (αDNA/βDNA = 2/8) due to relatively low amount of αDNA. In the hexagonal assembly, we can find alternating hexagonal lattice (upper domain) and incomplete but almost honeycomb lattice (**Figure 5.4c**), which are energetically degenerate. In particular, we can frequently find A particles enclosed with six B particles in 4/1 of number ratio (N_B/N_A), which is necessary to form honeycomb lattice. It is therefore suggested that further modulations of interparticle interactions based on asymmetric design strategy can realize 2D honeycomb lattice as shown in the previous MD

simulations. Furthermore, stoichiometry between A and B is critical to determine the final assembled structures.

Focusing on one specific particle number ratio, N_B/N_A = 2/1, we investigate compositional 2D structures, in particular the formation of honeycomb assembly, for higher relative attractive interaction, E_{BB}/E_{AB} = 0.62 (αDNA/βDNA = 3/7) and 0.83 (αDNA/βDNA = 4/6), at 0.16 particles/μm^2 of surface concentration. This higher surface concentration shows similar spatial arrangement with lower surface concentration based on peak location of pair correlation function (data not shown). For E_{BB}/E_{AB} = 0.83, even though unlike attractions are stronger than like attractions, segregation of the B particles occurs due to slight difference between unlike and like attractions. As shown in **Figure 5.4h**, whereas most of particles inside hexagonal lattice are B particles, A particles are located outside of the hexagonal lattice. For E_{BB}/E_{AB} = 0.62, we can find extended honeycomb lattice as shown in **Figure 5.4e**. Next, we can also find local kagome and square kagome lattice (**Figure 5.4f** and **Figure 5.4g**) as we already showed in MD simulations. However, where there are local kagome and square kagome, there is frequently local honeycomb lattice. This coexistence of different crystalline domains is comparable to the result from MD simulations, even though the relative interparticle interaction has different range (see Chapter 4). The plausible explanation would be due to the fact that the phase coexistence is caused by kinetics of 2D assembly process and locally different particle number ratio (N_B/N_A = 2/1 in this experiment as opposed to N_B/N_A = 1/1 in MD simulation). These results suggest that appropriate modulation of asymmetric like particle interaction and ratio of particle number lead to 2D close-packed morphologies that is formed as one ‘A’ particle surrounded by six ‘B’ particles. This arrangement could be

basic unit to fabricate compositionally ordered close-packed 2D crystal morphologies which is not able to be produced by simple design of DNA-mediated interactions.

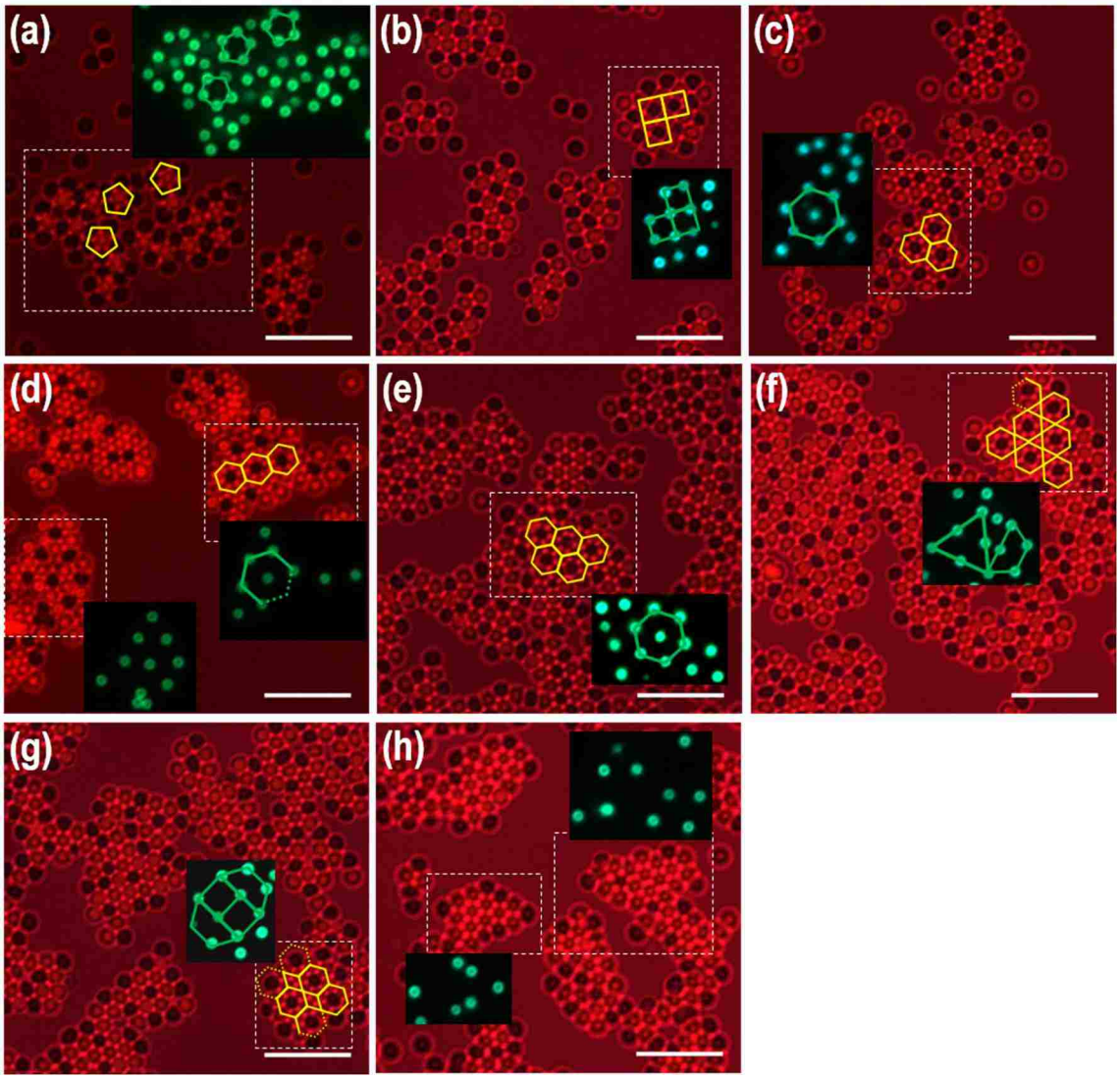

Figure 5.4. The formed 2D structures in terms of ratio of particle number (N_B/N_A) (a-d) and relative attractive interaction (E_{BB}/E_{AB}) (e-h): (a) pentagonal structures ,which B particles are surrounded by A particles at N_B/N_A = 1/4 and E_{BB}/E_{AB} = 0.41, (b) square lattice at N_B/N_A = 1/1 and E_{BB}/E_{AB} = 0.41, (c) honeycomb lattice at N_B/N_A = 2/1 and E_{BB}/E_{AB} = 0.41, (d) honeycomb lattice at N_B/N_A = 4/1 and E_{BB}/E_{AB} = 0.41, (e) connected honeycomb structures at N_B/N_A = 2/1 and E_{BB}/E_{AB} = 0.62, (f) Kagome and honeycomb structures at N_B/N_A = 2/1 and E_{BB}/E_{AB} = 0.62, (g) square Kagome and honeycomb structures at N_B/N_A = 2/1 and E_{BB}/E_{AB} = 0.62 and (h) demixed A and B particles at N_B/N_A = 2/1 and E_{BB}/E_{AB} = 0.83. Scale bar is 10μm.

5.3.4 Pair Correlation Function

To understand resulting structural difference according to the relative attraction and particle number ratio in compositional point of view, the pair correlation function is calculated with respect to each species, green A particles and red B particles from the fluorescent images. Due to limited domain size caused by steeply decreased movement of resultant assembly, the first and second peaks are investigated mainly. **Figure 5.5a** and **Figure 5.5b** shows the changes of pair correlation function in relative intensity and location of peaks for 'A' particles and 'B' particles depending on ratio of particle number (N_B/N_A) with constant $E_{BB}/E_{AB} = 0.41$, respectively. Due to the different amount of particle number and the asymmetric array between like particles, which means that A particles are repulsive each other and B particles are attractive each other, while the primary intense peaks of A species are located in r/D = $\sqrt{3}$ or 2, the primary intense peak of B species is located in r/D = 1 (**Figure 5.5a**). With increasing particle number ratio from $N_B/N_A = 1$ to $N_B/N_A = 4$ with constant $E_{BB}/E_{AB} = 0.41$, the relative intensity of first peak, which corresponds to nearest neighbors, to the second peak for A particles becomes weaker and that of B particles becomes stronger. This is consistent with the formed structures (as shown in **Figure 5.4d**) that each isolated A particle is surrounded by B particles. The extent of surrounding by B particles tends to increase with particle number ratio, consistent with structural changes from square and hexagonal lattice. From reference peaks, the primarily different peak between 2D square and honeycomb lattice is located in r/D = $\sqrt{3}$, irrespective of the particle species. Along with the changes in relative intensity of the first peak, the second peaks of B species in the pair correlation function (**Figure 5.5b**) become broader by growing peak corresponding to r/D = $\sqrt{3}$ with particle number ratio. It is might be due to the fact that the

number of surrounding particles for A species increases from four to six with particle number ratio. For the second peaks of A species, the peak located in r/D = $\sqrt{3}$ gradually increases with particle number ratio. The stronger peak at r/D = $\sqrt{3}$ is compatible with frequent observation of local honeycomb structures as the ratio of particle number increases. However, relatively constant peak at r/D = 2 for A species might be due to the fact that there exists multiple possibility with different lattice structures, including relatively compositionally random structures. The dominant square lattice coexisted with hexagonal lattice and pentagonal aggregates for N_B/N_A = 1 can make the peak located in r/D = 2. For higher ratio of particle number, the existence of peak at r/D = 2 could be caused by coexistence with alternating hexagonal, kagome lattice and random structures as square lattice is not present.

Figure 5.5c and **Figure 5.5d** show the dependence of pair correlation function for each species on the relative attractive interaction with constant N_B/N_A = 2. Considering only A species (**Figure 5.5c**), the peak at r/D = $\sqrt{3}$ becomes stronger from E_{BB}/E_{AB} = 0.41 to 0.62, whereas the peaks for E_{BB}/E_{AB} = 0.83 doesn't show monotonous rise. Increasing of attractive interaction enables B particles to surround more around each A particle. However, further increase near E_{BB}/E_{AB} produces simple phase separation and thus the distance between A species might reach gas state. Actually, the peaks at r/D = $\sqrt{3}$ and 2 for E_{BB}/E_{AB} = 0.83 weaken steeply as opposed relatively more intense peaks for E_{BB}/E_{AB} = 0.41 and 0.62. With respect to B species, low 'like' particle attraction is preferable to form square lattice due to superior A-B binding than B-B binding, whereas high 'like' particle attraction close to 'unlike' particle attraction leads to compositionally disordered hexagonal lattice as mentioned in **Figure 5.4h**. This suggests that proper design of like

particle interaction is necessary to provide selective surrounding around A particles. These individual analysis emphasize that 2D DNA-mediated crystallization depends on interplay between interparticle attraction and ratio of particle number. It is therefore suggested that proper selection between two variables could be significant to program desired two-dimensional DNA-mediated crystallization.

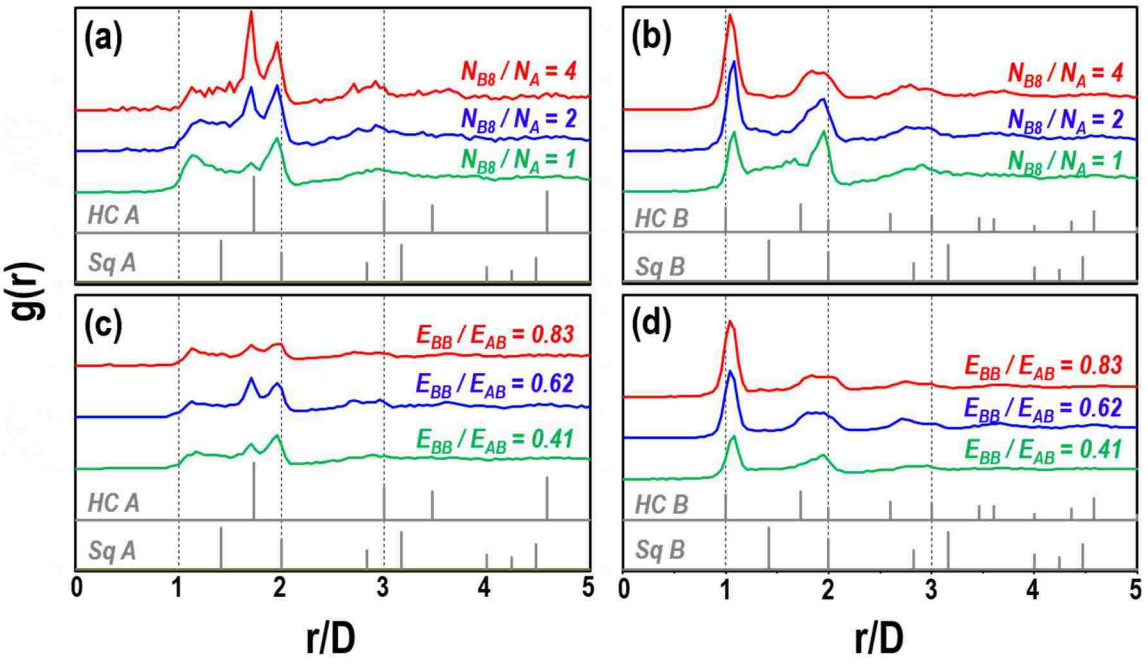

Figure 5.5. Pair correlation function for A and B particles in separate fluorescent images depending on the ratio of particle number ((a) for A particles and (c) B particles) with constant E_{BB}/E_{AB} = 2, and relative attractive interaction ((b) for A particles and (d) B particles) with constant N_B/N_A = 2. Grey lines represent A or B particles in perfect honeycomb structures and square lattice.

5.3.5 Further Discussion on Formed Crystal Phases

The major strategy to realize these diverse 2D crystalline configurations is use of asymmetric design of interparticle interactions, by which diverse crystal phases are accomplished in MD simulations. However, outcome of the preceding MD simulations is not able to translate easily into one of these experiments without the help of stoichiometric

factor. Also, desired structures from MD simulations is not full agreement with those from experiments. At E_{BB}/E_{AB} = 0.41 with N_B/N_A = 1, for instance, experimentally formed structure is primarily square lattice as opposed to hexagonal lattice in MD simulation. Furthermore, the emergence of kagome lattice coexisted with honeycomb is relatively at low relative attractive interactions, at E_{BB}/E_{AB} = 0.62 in the experiments as opposed to E_{BB}/E_{AB} ~ 0.9 in MD simulation, in different N_B/N_A terms. We assume that these distinctions are attributed to thermodynamic and kinetic factors: (1) temperature and annealing protocol difference, (2) slow kinetics in the experiment. For more extended crystalline arrangements, further understanding of these is required as future works.

5.4 Conclusion

In this Chapter, we present the first experimental investigation for a variety of 2D binary crystalline structures by controlling interparticle interaction and particle number ratio based on simple statistical mechanics approximation and preceding MD simulations. Without any template, we observed square, hexagonal lattice and pentagonal aggregates, which are driven by the interplay between attractive and repulsive interaction. With respect to compositional ordering of hexagonal lattice, we observed four different binary ordered structures: alternating, honeycomb, kagome and square kagome. However, more study to understand kinetic effect and defect formation is necessary to achieve well-defined long-range crystalline structures. This strategy opens alternative pathway to create more complex crystalline structures. Also, this 2D DNA-microparticle system could be a convenient platform to study the phase change and dynamics of DNA-mediated assembly, as other area has been performed (*107*, *126*).

Chapter 6:

Conclusions and Future Outlook

6.1 Summary

This dissertation has established the strategies to engineer a diversity of 2D crystalline arrangements using DNA-mediated interactions *via* the interplay of simulation, theory and experiments. Experimental realization for 2D DNA-mediated microparticle assembly described in Chapter 2 was achieved by micron-sized silica particles linked covalently ssDNA through two-step functionalization: silanization and following subsequent cyanuric chloride chemistry. Chapter 3 demonstrated temperature-dependent stability of DNA-induced interactions between these particles can be controlled by the concentration of nonionic surfactant through an apparent coupling with the critical micelle temperature in these system. Also, 2D ordered arrangements (square and hexagonal lattices) were evolved from disordered along with pre-established melting profiles. Motivated by these different 2D arrangements according to designed interactions, 'multi-flavored' system was adopted to propose systematic study that make use of available information on pair interaction between the particles from MD simulation for diverse 2D crystal phases in Chapter 4. The key feature is use of symmetric or asymmetric design of like pair interactions (E_{AA}, E_{BB}), with constant unlike pair interactions (E_{AB}), as a function of relative attraction strengths (E_{AA}/E_{AB}, E_{BB}/E_{AB}). The phase diagram of symmetric system consisted of compositionally perfect square, alternating string hexagonal and random hexagonal lattices. Asymmetric system extended structural diversity into rhombic,

honeycomb, as well as kagome, depending on the relative interparticle interactions. These model findings were translated to the experiment, in which binary microparticles were decorated with a tailored mixture of two different complementary DNA strands as a straight-forward means to realize tunable particle interactions, as described in Chapter 5. Guided by simple statistical mechanics and detailed MD simulations, a structural diversity of microparticle 2D assemblies, such as square, pentagonal and hexagonal lattices (honeycomb, kagome), was realized through the interplay of interparticle interactions and stoichiometry. Controlling interparticle interaction using this DNA-mediated particle "multi-flavoring" should lead to an even wider range of accessible colloidal crystal structures. The 2D experiments coupled with the model predictions can ultimately be used to provide new fundamental insight into nano- or microparticle assembly in three dimensions.

6.2 Future Work

We conclude this thesis with future work to extend the established bottom-up DNA-mediated particle assembly towards structural diversity and 3-dimensional order with preliminary proof-of-concept data. Also, we mention possible ways to modulate DNA-mediated assembly through external forces.

6.2.1 Structural Diversity by Stoichiometry and Lattice Symmetry

In spite of the realization of square and hexagonal lattices with two-dimensional order through reversible and sequence-specific binding, continuing work is necessary to increase the structural diversity of DNA-mediated microparticle assembly in the

fundamental and practical standpoint. The incorporation of stoichiometry and lattice symmetry would greatly enlarge the parameter space for the design of ordered DNA-mediated assembly. While DNA-mediated nanoparticle assembly (*44*) has been achieved to realize various crystal phases under these parameter space, Wang et al. (*34*) demonstrated AB_2 and AB_6 colloidal crystals isostructural to aluminum boride (AlB_2) and cesium fullerene complex (Cs_6C_{60}), respectively, by changing the size ratio and stoichiometry. Also, particle shapes (*33*, *59*) along with DNA-induced interactions can be useful constraint, which determine the accessible configurations, to establish complex, functional and integrated architectures.

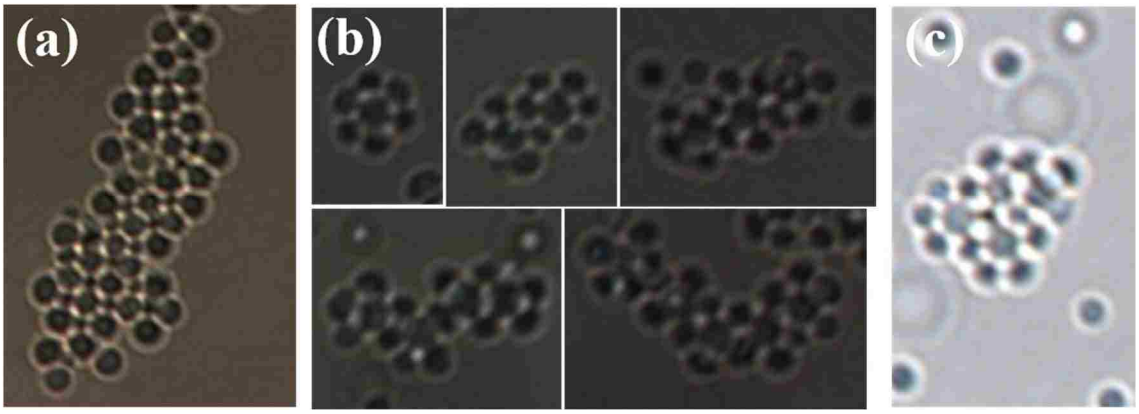

Figure 6.1. DNA-mediated microparticle assembly with two different sizes of particles (1 μm, 1.5 μm) and different stoichiometry. Here, two particles have only selective reciprocal interactions (A-B). (a) square lattice (1:1 stoichiometry), (b) semi-hexagonal lattices (8:1 stoichiometry) and (c) formed small honeycomb lattice (8:1 stoichiometry).

The binary particles with two different sizes (1 μm and 1.5 μm) and two different stoichiometries (1:1 and 8:1) were assembled through selective reciprocal DNA-mediated interactions near melting temperature. With 1:1 stoichiometry, square lattice emerged as shown in **Figure 6.1a**. With 8:1 stoichiometry, most of them are assembled into hexagonal structures with some pentagonal aggregates as shown in **Figure 6.1b**. Also, we were able

to see honeycomb lattices, which emerged for equal-sized particles (1:1 stoichiometry) under asymmetric design of interparticle interactions. These suggest that particle size and stoichiometry also are beneficial parameters to build up complex, functional and integrated architectures in DNA-programmable particle assembly. Combined with the previous strategies to control interparticle interactions, structural diversity can be realized in 2D and extended into 3D. Furthermore, distinct from the crystal phases with 3-dimensional order, the formation of crystal phases in 2D allows us to access time-dependent behavior more easily during structural formation. Therefore, this clearer visualization facilitates to understand their kinetics and detailed formation process.

6.2.2 Extension of MD Simulation to Three-Dimensional Order

Very recently, the cross-dimensional phase behavior of specifically designed isotropic interactions with low coordination has been investigated by Jain and coworkers (*127*). To be more specific, they showed an isotropic, convex-repulsive pair potential that stabilizes 2D-honeycomb lattice is expected to be an excellent candidate for making a 3D-diamond lattice, and vice versa. Motivated by this prominent transferability between 2D and 3D, we are trying to extend our effective pair potential into 3D from 2D. Interestingly, the asymmetric design of like particle pairs ($E_{AB} > E_{AA} > E_{BB}$) provided perfect honeycomb lattice in 2D, as shown in Chapter 4. Strictly, our formed honeycomb lattice is highly coordinated lattice, not low coordination, as central particle in honeycomb lattice is not vacant. Nonetheless, the transferability from 2D to 3D would be quite efficient and useful in terms of fundamental and practical standpoints, in that finding interactions that stabilize lattices in 2D is a simpler and less computationally demanding material design problem that in 3D.

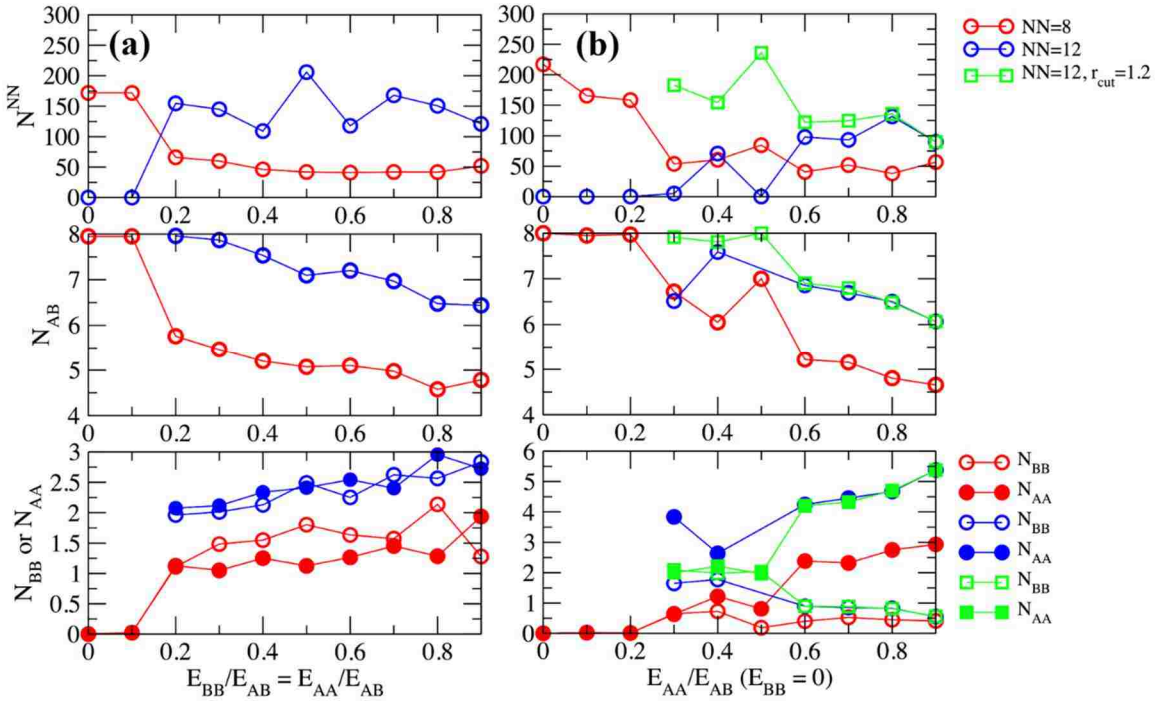

Figure 6.2. Ordering parameters for binary crystals under (a) symmetric interactions between like particles ($E_{AB} > E_{AA} = E_{BB}$) and (b) asymmetric interactions between like particles ($E_{AB} > E_{AA} > E_{BB} = 0$). For each criterion of BCC (NN = 8) and FCC or HCP (NN = 12), the number of nearest neighbors N^{NN} and the order parameters (N_{AB}, N_{AA}, N_{BB}) are computed to quantify the ordering of BCC and close-packed crystals, FCC or HCP.

Taking advantage of similar protocols, the 3D MD simulations are performed through the effective pair potentials under symmetric interactions between like particles ($E_{AB} > E_{AA} = E_{BB}$) and asymmetric interactions between like particles ($E_{AB} > E_{AA} > E_{BB} = 0$). For the quantitative identification of lattice structures (body-centered cubic (BCC) vs. close-packed crystals (CP)), the average number of particles N^{NN} with a certain number of nearest neighbors (NN) based on a distance cutoff criteria is calculated. For the symmetric case, BCC with almost perfect order parameters ($2N_{AB} = 8$, $2N_{AA} = 2N_{BB} = 0$) formed at the relatively small relative interactions (E_{AA}/E_{AB} or $E_{BB}/E_{AB} < 0.2$), whereas there was no formation of CP. At E_{AA}/E_{AB} or $E_{BB}/E_{AB} \sim 0.2$, we can see the transformation from BCC

to CP, which is comparable to outcome of 2D simulations. Above this point, the stabilized structure is CP with different order parameters as a function of the interparticle interactions. Likewise 2D simulations, almost compositionally ordered CP ($2N_{AB} = 8$, $2N_{AA} = 2N_{BB} = 2$) is formed at E_{AA}/E_{AB} (= E_{BB}/E_{AB}) close to the transformation point. As increasing E_{AA}/E_{AB}, the order parameter arrives to the value for compositionally random structures ($2N_{AB} = 6$).

For the asymmetric case ($E_{AB} > E_{AA} > E_{BB} = 0$), almost perfect ordered BCC is stable below $E_{AA}/E_{AB} < 0.2$ ($E_{BB}/E_{AB} = 0$) and CP with low compositional ordering emerges above $E_{AA}/E_{AB} > 0.6$ ($E_{BB}/E_{AB} = 0$), based on a distance cutoff criteria ($r_{cut} = 1.05$). Interestingly, the number of 12-fold coordinated CP structures, which is expected as the number of 8-fold coordinated BCC crystals decreased steeply at $0.2 < E_{AA}/E_{AB} < 0.3$, is relatively low at intermediate region between them. However, when we use larger distance cutoff criteria ($r_{cut} = 1.2$), the 12-fold coordinated CP crystals with almost perfect ordering can be found. This is caused by slight different distance between unlike particle pairs and like particle pairs ($D_{AB} = 1.028$ vs $D_{AA} \sim D_{BB} \sim 1.058$) due to the asymmetric design. Based on adaptive common neighbor analysis in OVITO (*128*), we can get perfect face-centered cubic (FCC) crystal phases. Combined with this and the compositional ordering in the intermediate region, we believe these structures are perfect ordered FCC (CuAu). In the previous literature (*121*), the transformation from BCC to FCC (CuAu) would be promoted by anisotropic dynamics such as self-induced hydrodynamic drag forces. The design of asymmetric like particle interactions would also drive anisotropic dynamics to transform from BCC to FCC (CuAu). However, further analysis is required to verify and confirm these 3D structures.

Distinct from the realization of 3D-diamond structures by using the isotropic, convex-repulsive pair potentials for the 2D-honeycomb lattices, the 2D-honeycomb by using our attractive pair potentials was difficult to produce low coordinated 3D structures. We believe that the current interaction system is not preferable to produce low coordinated structures due to their large lattice free energy relative to the CP and BCC lattices, as predicted in the previous literature (*112*).

Motivated by this preliminary result, we believe that repulsive interaction could be a significant parameter to obtain open structures, which is useful technological applications (*129*, *130*). Tkachenko (*26*) and coworkers suggested that theoretical phase behavior is mainly dependent on two parameters, the relative strength of the attraction (E/U_0: E is reversible binding energy and $U_0 \equiv U(d)$, here U(r) is repulsive soft-core potential) and aspect ratio (d/ξ: d is diameter and ξ is the range of potential U(r)). Interestingly, two parameters are sensitive to the range and strength of repulsive interactions. For example, the emergence of diamond structures is largely dependent on the selection of repulsive potential, such as exponential and Gaussian forms of repulsive potentials. Furthermore, the experimental realization of diamond-like structures using nanoparticles has been established through screened electrostatic interactions commensurate with the dimensions of the assembling objects (*131*).

6.2.3 Assembly in the Presence of External Fields

The current state-of-the-art for achieving crystalline structures from DNA-mediated particle assembly relies on thermal annealing, which leads to local rearrangement and restructuring of particles *via* reversible hybridization/dehybridization (*32*). Here, we consider an additional handle for overcoming kinetic barriers and tuning crystallization.

Namely, the rearrangement of DNA-functionalized particles, especially microparticles, can be induced and enhanced by external forces, such as shear and horizontal vibration (*132*, *133*). Based on this concept, we hypothesize that the enhanced mobility of particles, achieved by imposition of various external fields, may help expand the crystallization window, thus enabling more facile circumvention of dynamic arrest. These concepts can be applied to 2D as well as 3D.

6.2.3.1 Flow field

A significant amount of research has focused on shear-induced clustering, ordering, orientational alignment and structural changes in a variety of soft matter systems (*134–137*). Interestingly, under flow, colloidal crystals often exhibit enhanced order and transition in their symmetry at low shear rates, and shear-induced melting at high shear rates (*138*, *139*). It also has been reported that shear influences both the stretching of DNA molecules and their migration to the centerline of a channel.(*140*) Besides large shear forces can affect the rupture dynamics of the double-stranded DNA (*141*). These effects, observed separately for un-functionalized particles and isolated DNA, provide the groundwork for our study of the effect of flow field on aggregate/assembly of DNA-functionalized particles. Specifically, we study the role of shear to enhance the rearrangement of the particles as a handle for facilitating and controlling crystallization within DNA-mediated assembly.

It has been shown that colloidal aggregates/crystals can undergo microstructural changes in the low shear regime and distortion in the high shear regime (*142*). Firstly, we perform experiments to observe the assembly behavior of DNA-mediated particles depending on the shear force. The shear-induced melting for DNA-mediated assembly is

also interesting from this experiment but the finding of appropriate shear regimes for the rearrangement may be more significant for realization of specific ordered structures.

Based on our preliminary mechanistic insight into the DNA-mediated aggregation of micron-scaled particles, enhancing the particle motion may also allow us to see not only faster restructuring but also the formation of larger aggregates/crystals. Specifically, our studies have shown that aggregates display a glassy structure movement as the size of aggregates increased, with only small crystalline domains emerging (data not shown). We hypothesize that imposition of an external force/flow field will enhance particle movement and thereby induce more rapid and extensive the evolution of crystalline structures similar to the mechanism proposed by Macfarlane *et al*. for nanometer-scale particles (*62*).

6.2.3.2 Horizontal Vibration

Oscillatory flow has also been shown to enhance the rearrangement and anneal defects during the formation of microparticulate structures (*133*, *143*). Interestingly, Muangnapoh *et al*. reported that the convective deposition of particles exhibited a significant enhancement of surface density and local order of monolayers with increasing deposition speed through addition of vibration.

As a preliminary study, we compared the morphology of aggregates achieved by DNA-mediated assembly in the presence of imposed horizontal vibrations. The mixture of 1 μm DNA-functionalized particles with complementary sticky ends was inserted inside a microchamber which was composed of two coverslips with ~ 100 μm parafilm as a spacer. The sample was vibrated horizontally by a wave generator, with 50 Hz and 250 μm displacement, for 20 min. After only 20 minutes, compact aggregates (**Figure 6.3b**) were observed to form whereas only branched (or linear) structures (**Figure 6.3a**) resulted after

2 hours in a quiescent control sample. This preliminary data indicates that particle rearrangement is improved when the horizontal vibration is applied to the chamber. Based on this result, we can study systematically how flow-field oscillations may be used to enhance aggregation and even crystallization of the DNA-functionalized microparticles. We will study factors such as amplitude and frequency of oscillations in an effort to quantify their role in tuning DNA-mediated assembly and crystallization (i.e., structure, quality, extent) as well as to elucidate concomitant effects on the melting transition and the shape/breadth of the transition region.

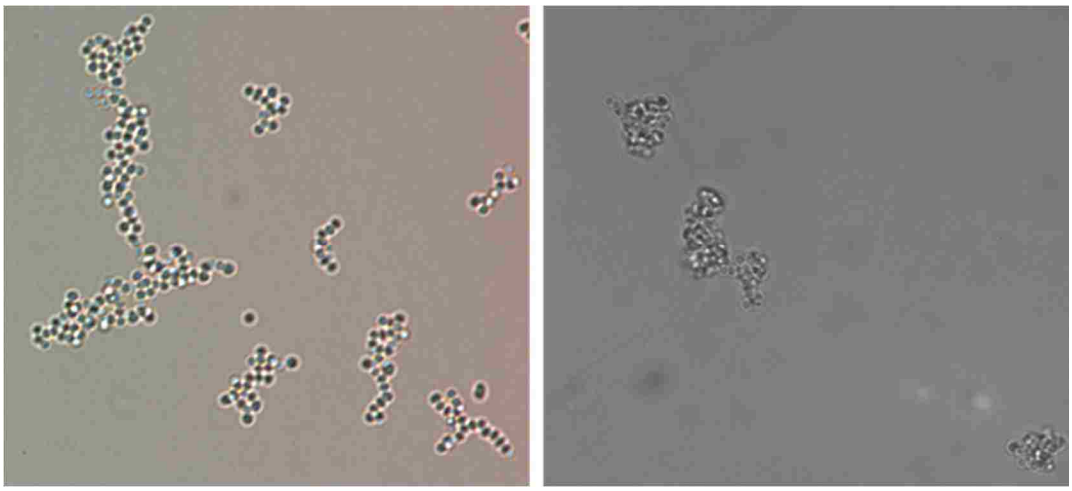

Figure 6.3. The morphology of aggregates according to the existence of the lateral vibration: remained at RT for 2 hours without the vibration (Left); with the vibration, with 50 Hz and 250 μm displacement, for 20 min (Right).

Bibliography

1. H. Löwen, in *Computer Simulations in Condensed Matter Systems: From Materials to Chemical Biology, Vol 2* (2006), vol. 704, pp. 139–161.

2. W. B. Russel, D. A. Saville, W. R. Schowalter, *Colloidal dispersions* (Cambridge University Press, Cambridge, 1989), vol. 54.

3. P. N. Pusey, W. van Megen, Phase behaviour of concentrated suspensions of nearly hard colloidal spheres. *Nature*. **320**, 340–342 (1986).

4. H. Löwen, Melting, freezing and colloidal suspensions. *Phys. Rep.* **237**, 249–324 (1994).

5. S.-H. Kim, S. Y. Lee, S.-M. Yang, G.-R. Yi, Self-assembled colloidal structures for photonics. *NPG Asia Mater.* **3**, 25–33 (2011).

6. A. Stein, B. E. Wilson, S. G. Rudisill, Design and functionality of colloidal-crystal-templated materials—chemical applications of inverse opals. *Chem. Soc. Rev.* **42**, 2763–2803 (2013).

7. G. M. Whitesides, B. Grzybowski, Self-Assembly at All Scales. *Science (80-.).* **295**, 2418–2421 (2002).

8. W. K. Kegel, Direct Observation of Dynamical Heterogeneities in Colloidal Hard-Sphere Suspensions. *Science (80-.).* **287**, 290–293 (2000).

9. S. C. Kung, C. C. Chang, W. Fan, M. A. Snyder, Template-free ordered mesoporous silicas by binary nanoparticle assembly. *Langmuir*. **30**, 11802–11811 (2014).

10. S. Asakura, F. Oosawa, On Interaction between Two Bodies Immersed in a Solution of Macromolecules. *J. Chem. Phys.* **22**, 1255 (1954).

11. E. V Shevchenko, D. V Talapin, N. a Kotov, S. O'Brien, C. B. Murray, Structural diversity in binary nanoparticle superlattices. *Nature*. **439**, 55–9 (2006).

12. M. E. Leunissen *et al.*, Ionic colloidal crystals of oppositely charged particles. *Nature*. **437**, 235–240 (2005).

13. L. Cademartiri, K. J. M. Bishop, Programmable self-assembly. *Nat. Mater.* **14**, 2–9 (2015).

14. M. Grzelczak, J. Vermant, E. M. Furst, L. M. Liz-Marzán, Directed self-assembly of nanoparticles. *ACS Nano*. **4**, 3591–3605 (2010).

15. B. a. Grzybowski, C. E. Wilmer, J. Kim, K. P. Browne, K. J. M. Bishop, Self-assembly: from crystals to cells. *Soft Matter*. **5**, 1110 (2009).

16. W. Shenton, S. A. Davis, S. Mann, Directed Self-Assembly of Nanoparticles into Macroscopic Materials Using Antibody–Antigen Recognition. *Adv. Mater.* **11**, 449–

452 (1999).

17. A. L. Hiddessen *et al.*, Assembly of Binary Colloidal Structures via Specific Biological Adhesion. *Langmuir*. **16**, 9744–9753 (2000).

18. E. Winfree, F. Liu, L. a Wenzler, N. C. Seeman, Design and self-assembly of two-dimensional DNA crystals. *Nature*. **394**, 539–544 (1998).

19. J. D. Watson, F. H. C. Crick, Molecular structure of nucleic acids. *Nature*. **171** (1953), pp. 737–738.

20. N. Geerts, E. Eiser, DNA-functionalized colloids: Physical properties and applications. *Soft Matter*. **6**, 4647 (2010).

21. M. R. Jones, N. C. Seeman, C. A. Mirkin, Programmable materials and the nature of the DNA bond. *Science (80-.).* **347**, 1260901–1260901 (2015).

22. B. Yurke, A. J. Turberfield, A. P. Mills, F. C. Simmel, J. L. Neumann, A DNA-fuelled molecular machine made of DNA. *Nature*. **406**, 605–608 (2000).

23. W. B. Sherman, N. C. Seeman, A precisely controlled DNA biped walking device. *Nano Lett.* **4**, 1203–1207 (2004).

24. H. Gu, J. Chao, S.-J. Xiao, N. C. Seeman, A proximity-based programmable DNA nanoscale assembly line. *Nature*. **465**, 202–205 (2010).

25. F. Wang, C.-H. Lu, I. Willner, From cascaded catalytic nucleic acids to enzyme-DNA nanostructures: controlling reactivity, sensing, logic operations, and assembly of complex structures. *Chem. Rev.* **114**, 2881–2941 (2014).

26. A. V Tkachenko, Morphological diversity of DNA-colloidal self-assembly. *Phys. Rev. Lett.* **89**, 148303 (2002).

27. L. Di Michele, E. Eiser, Developments in understanding and controlling self assembly of DNA-functionalized colloids. *Phys. Chem. Chem. Phys.* **15**, 3115–29 (2013).

28. S. Hurst, A. Lytton-Jean, C. Mirkin, Maximizing DNA loading on a range of gold nanoparticle sizes. *Anal. Chem.* **78**, 8313–8318 (2006).

29. R. Jin, G. Wu, Z. Li, C. A. Mirkin, G. C. Schatz, What Controls the Melting Properties of DNA-Linked Gold Nanoparticle Assemblies? *J. Am. Chem. Soc.* **125**, 1643–1654 (2003).

30. J. Storhoff, R. Elghanian, C. Mirkin, R. Letsinger, Sequence-dependent stability of DNA-modified gold nanoparticles. *Langmuir*, 8916–8920 (2002).

31. L. Demers, C. Mirkin, A fluorescence-based method for determining the surface coverage and hybridization efficiency of thiol-capped oligonucleotides bound to gold thin films and. *Anal. Chem.* **72**, 5535–5541 (2000).

32. D. Nykypanchuk, M. M. Maye, D. van der Lelie, O. Gang, DNA-guided crystallization of colloidal nanoparticles. *Nature*. **451**, 549–552 (2008).

33. F. Lu, K. G. Yager, Y. Zhang, H. Xin, O. Gang, Superlattices assembled through shape-induced directional binding. *Nat. Commun.* **6**, 6912 (2015).

34. Y. Wang *et al.*, Crystallization of DNA-coated colloids. *Nat. Commun.* **6**, 7253 (2015).

35. M.-P. Valignat, O. Theodoly, J. C. Crocker, W. B. Russel, P. M. Chaikin, Reversible self-assembly and directed assembly of DNA-linked micrometer-sized colloids. *Proc. Natl. Acad. Sci. U. S. A.* **102**, 4225–4229 (2005).

36. M. E. Leunissen *et al.*, Switchable self-protected attractions in DNA-functionalized colloids. *Nat. Mater.* **8**, 590–5 (2009).

37. R. Dreyfus *et al.*, Simple Quantitative Model for the Reversible Association of DNA Coated Colloids. *Phys. Rev. Lett.* **102**, 048301 (2009).

38. R. Dreyfus *et al.*, Aggregation-disaggregation transition of DNA-coated colloids: Experiments and theory. *Phys. Rev. E.* **81**, 041404 (2010).

39. D. Nykypanchuk, M. M. Maye, D. van der Lelie, O. Gang, DNA-based approach for interparticle interaction control. *Langmuir*. **23**, 6305–14 (2007).

40. M. T. Casey *et al.*, Driving diffusionless transformations in colloidal crystals using DNA handshaking. *Nat. Commun.* **3**, 1209 (2012).

41. V. T. Milam, A. L. Hiddessen, J. C. Crocker, D. J. Graves, D. A. Hammer, DNA-Driven Assembly of Bidisperse, Micron-Sized Colloids. *Langmuir*. **19**, 10317–10323 (2003).

42. S. A. J. van der Meulen, M. E. Leunissen, Solid colloids with surface-mobile DNA linkers. *J. Am. Chem. Soc.* **135**, 15129–15134 (2013).

43. W. B. Rogers, V. N. Manoharan, Programming colloidal phase transitions with DNA strand displacement. *Science (80-.).* **347**, 639–642 (2015).

44. R. J. Macfarlane *et al.*, Nanoparticle superlattice engineering with DNA. *Science (80-.).* **334**, 204–208 (2011).

45. S. Y. Park *et al.*, DNA-programmable nanoparticle crystallization. *Nature*. **451**, 553–556 (2008).

46. A. P. Alivisatos *et al.*, Organization of "nanocrystal molecules" using DNA. *Nature*. **382**, 609–611 (1996).

47. C. A. Mirkin, R. L. Letsinger, R. C. Mucic, J. J. Storhoff, A DNA-based method for rationally assembling nanoparticles into macroscopic materials. *Nature*. **382**, 607–609 (1996).

48. M. M. Maye, M. T. Kumara, D. Nykypanchuk, W. B. Sherman, O. Gang, Switching binary states of nanoparticle superlattices and dimer clusters by DNA strands. *Nat. Nanotechnol.* **5**, 116–120 (2010).

49. M. M. Maye, D. Nykypanchuk, D. van der Lelie, O. Gang, DNA-regulated micro-

and nanoparticle assembly. *Small*. **3**, 1678–1682 (2007).

50. S. Park, A. Lazarides, The structural characterization of oligonucleotide-modified gold nanoparticle networks formed by DNA hybridization. *J. Phys. Chem. B*, 12375–12380 (2004).

51. S. Park, A. Lazarides, Directed Assembly of Periodic Materials from Protein and Oligonucleotide-Modified Nanoparticle Building Blocks. *Angew. Chem. Int. Ed. Engl.* **40**, 2909–2912 (2001).

52. S. Y. Park, J.-S. Lee, D. Georganopoulou, C. a Mirkin, G. C. Schatz, Structures of DNA-linked nanoparticle aggregates. *J. Phys. Chem. B*. **110**, 12673–81 (2006).

53. S. Park, D. Stroud, Structure formation, melting, and optical properties of gold/DNA nanocomposites: Effects of relaxation time. *Phys. Rev. B*. **68**, 224201 (2003).

54. S. Phan *et al.*, Phase transition, equation of state, and limiting shear viscosities of hard sphere dispersions. *Phys. Rev. E. Stat. Phys. Plasmas. Fluids. Relat. Interdiscip. Topics*. **54**, 6633–6645 (1996).

55. E. Strable, J. E. Johnson, M. G. Finn, Natural Nanochemical Building Blocks: Icosahedral Virus Particles Organized by Attached Oligonucleotides. *Nano Lett.* **4**, 1385–1389 (2004).

56. O. D. Velev, Materials science. Self-assembly of unusual nanoparticle crystals. *Science*. **312**, 376–7 (2006).

57. J. M. Gibbs-Davis, G. C. Schatz, S. T. Nguyen, Sharp melting transitions in DNA hybrids without aggregate dissolution: Proof of neighboring-duplex cooperativity. *J. Am. Chem. Soc.* **129**, 15535–15540 (2007).

58. D. B. Lukatsky, D. Frenkel, Phase behavior and selectivity of DNA-linked nanoparticle assemblies. *Phys. Rev. Lett.* **92**, 068302 (2004).

59. M. R. Jones *et al.*, DNA-nanoparticle superlattices formed from anisotropic building blocks. *Nat. Mater.* **9**, 913–917 (2010).

60. C. Zhang *et al.*, A general approach to DNA-programmable atom equivalents. *Nat. Mater.* **12**, 741–6 (2013).

61. H. Hill, R. Macfarlane, A. Senesi, B. Lee, Controlling the lattice parameters of gold nanoparticle FCC crystals with duplex DNA linkers. *Nano Lett.* **58** (2008) (available at http://pubs.acs.org/doi/abs/10.1021/nl8011787).

62. R. J. Macfarlane *et al.*, Assembly and organization processes in DNA-directed colloidal crystallization. *Proc. Natl. Acad. Sci. U. S. A.* **106**, 10493–10498 (2009).

63. H. Xiong, D. van der Lelie, O. Gang, Phase Behavior of Nanoparticles Assembled by DNA Linkers. *Phys. Rev. Lett.* **102**, 015504 (2009).

64. R. Macfarlane, M. Jones, Establishing the Design Rules for DNA-Mediated Programmable Colloidal Crystallization. *Angew. Chemie*, 4589–4592 (2010).

65. S. Srivastava, D. Nykypanchuk, M. M. Maye, A. V. Tkachenko, O. Gang, Super-compressible DNA nanoparticle lattices. *Soft Matter*. **9**, 10452 (2013).

66. P. H. Rogers *et al.*, Selective, controllable, and reversible aggregation of polystyrene latex microspheres via DNA hybridization. *Langmuir*. **21**, 5562–9 (2005).

67. P. L. Biancaniello, J. C. Crocker, D. a Hammer, V. T. Milam, DNA-mediated phase behavior of microsphere suspensions. *Langmuir*. **23**, 2688 (2007).

68. M. E. Leunissen, R. Dreyfus, R. Sha, N. C. Seeman, P. M. Chaikin, Quantitative study of the association thermodynamics and kinetics of DNA-coated particles for different functionalization schemes. *J. Am. Chem. Soc.* **132**, 1903–1913 (2010).

69. K.-T. Wu *et al.*, Polygamous particles. *Proc. Natl. Acad. Sci. U. S. A.* **109**, 18731–6 (2012).

70. W. B. Rogers, J. C. Crocker, Direct measurements of DNA-mediated colloidal interactions and their quantitative modeling. *Proc. Natl. Acad. Sci. U. S. A.* **108**, 15687–15692 (2011).

71. P. L. Biancaniello, A. J. Kim, J. C. Crocker, Colloidal Interactions and Self-Assembly Using DNA Hybridization. *Phys. Rev. Lett.* **94**, 058302 (2005).

72. A. J. Kim, P. L. Biancaniello, J. C. Crocker, Engineering DNA-mediated colloidal crystallization. *Langmuir*. **22**, 1991–2001 (2006).

73. A. J. Kim, R. Scarlett, P. L. Biancaniello, T. Sinno, J. C. Crocker, Probing interfacial equilibration in microsphere crystals formed by DNA-directed assembly. *Nat. Mater.* **8**, 52–5 (2009).

74. A. J. Kim, V. N. Manoharan, J. C. Crocker, Swelling-based method for preparing stable, functionalized polymer colloids. *J. Am. Chem. Soc.* **127**, 1592–3 (2005).

75. S. Angioletti-Uberti, B. M. Mognetti, D. Frenkel, Re-entrant melting as a design principle for DNA-coated colloids. *Nat. Mater.* **11**, 518–522 (2012).

76. D. M. Hartmann, M. Heller, S. C. Esener, D. Schwartz, G. Tu, Selective DNA attachment of micro- and nanoscale particles to substrates. *J. Mater. Res.* **17**, 473–478 (2002).

77. E. M. Puchner, S. K. Kufer, M. Strackharn, S. W. Stahl, H. E. Gaub, Nanoparticle Self-Assembly on a DNA-Scaffold Written by Single-Molecule Cut-and-Paste. *Nano Lett.* **8**, 3692–3695 (2008).

78. M. H. S. Shyr, D. P. Wernette, P. Wiltzius, Y. Lu, P. V Braun, DNA and DNAzyme-mediated 2D colloidal assembly. *J. Am. Chem. Soc.* **130**, 8234–40 (2008).

79. B. Zou, B. Ceyhan, U. Simon, C. M. Niemeyer, Self-assembly of crosslinked DNA-gold nanoparticle layers visualized by In-Situ scanning force microscopy. *Adv. Mater.* **17**, 1643–1647 (2005).

80. W. Cheng *et al.*, Free-standing nanoparticle superlattice sheets controlled by DNA. *Nat. Mater.* **8**, 519–525 (2009).

81. N. Geerts, E. Eiser, Flying colloidal carpets. *Soft Matter*. **6**, 664 (2010).

82. S. Srivastava *et al.*, Two-dimensional DNA-programmable assembly of nanoparticles at liquid interfaces. *J. Am. Chem. Soc.* **136**, 8323–8332 (2014).

83. B. a Grzybowski, A. Winkleman, J. a Wiles, Y. Brumer, G. M. Whitesides, Electrostatic self-assembly of macroscopic crystals using contact electrification. *Nat. Mater.* **2**, 241–245 (2003).

84. K. S. Khalil *et al.*, Binary colloidal structures assembled through Ising interactions. *Nat. Commun.* **3**, 794 (2012).

85. W. Fan *et al.*, Hierarchical nanofabrication of microporous crystals with ordered mesoporosity. *Nat. Mater.* **7**, 984–91 (2008).

86. W. Stöber, A. Fink, E. Bohn, Controlled growth of monodisperse silica spheres in the micron size range. *J. Colloid Interface Sci.* **69**, 62–69 (1968).

87. L. Wang, W. Zhao, W. Tan, Bioconjugated silica nanoparticles: Development and applications. *Nano Res.* **1**, 99–115 (2008).

88. G. Steinberg, K. Stromsborg, L. Thomas, D. Barker, C. Zhao, Strategies for covalent attachment of DNA to beads. *Biopolymers*. **73**, 597–605 (2004).

89. E. Soto-Cantu, R. Cueto, J. Koch, P. S. Russo, Synthesis and Rapid Characterization of Amine-Functionalized Silica. *Langmuir*. **28**, 5562–5569 (2012).

90. R. K. Iler, *The Chemistry of Silica: Solubility, Polymerization, Colloid and Surface Properties and Biochemistry of Silica* (Wiley-Interscience, 1979).

91. S. Y. Choi, Y. Lee, Y. S. Park, K. Ha, K. B. Yoon, Monolayer Assembly of Zeolite Crystals on Glass with Fullerene as the Covalent Linker. *J. Am. Chem. Soc.* **122**, 5201–5209 (2000).

92. H. Hill, J. Millstone, M. Banholzer, C. Mirkin, The role radius of curvature plays in thiolated oligonucleotide loading on gold nanoparticles. *ACS Nano*. **3**, 418–424 (2009).

93. L. Di Michele *et al.*, Multistep kinetic self-assembly of DNA-coated colloids. *Nat. Commun.* **4**, 2007 (2013).

94. R. Macfarlane, M. Jones, B. Lee, Topotactic interconversion of nanoparticle superlattices. *Science (80-.).* **341**, 1222–1225 (2013).

95. Y. Ding, J. Mittal, Insights into DNA-mediated interparticle interactions from a coarse-grained model. *J. Chem. Phys.* **141**, 184901 (2014).

96. X. Liang, G. Mao, K. Y. S. Ng, Effect of chain lengths of PEO-PPO-PEO on small unilamellar liposome morphology and stability: an AFM investigation. *J. Colloid Interface Sci.* **285**, 360–72 (2005).

97. P. Alexandridis, J. F. Holzwarthf, T. A. Hatton, Micellization of Poly (ethylene oxide) -Poly (propylene oxide) -Poly (ethylene oxide) Triblock Copolymers in

Aqueous Solutions : Thermodynamics of Copolymer Association. *Macromolecules*. **27**, 2414–2425 (1994).

98. W. Brown, K. Schillln, M. Almgren, Micelle and Gel Formation in a Poly (ethylene oxide)/Poly (propylene oxlde)/Poly (ethylene oxide) Triblock Copolymer in Water Solution. Dynamic and Static Light Scattering and Oscillatory Shear Measurements. *J. Phys. Chem.*, 1850–1858 (1991).

99. K. Mortensen, J. Pedersen, Structural study on the micelle formation of poly (ethylene oxide)-poly (propylene oxide)-poly (ethylene oxide) triblock copolymer in aqueous solution. *Macromolecules*. **26**, 805–812 (1993).

100. J. C. Crocker, D. G. Grier, Methods of digital video microscopy for colloidal studies. *J. Colloid Interface Sci.* **310**, 298–310 (1996).

101. Y. Gao, M. L. Kilfoil, Accurate detection and complete tracking of large populations of features in three dimentions. *Opt. Express*. **17**, 4685–4704 (2009).

102. K. Sun, S. R. Raghavan, Thermogelling aqueous fluids containing low concentrations of pluronic F127 and laponite nanoparticles. *Langmuir*. **26**, 8015–8020 (2010).

103. C. N. Likos, Effective interactions in soft condensed matter physics. *Phys. Rep.* **348**, 267–439 (2001).

104. S. Kumar, M. J. Lee, V. K. Aswal, S. M. Choi, Block-copolymer-induced long-range depletion interaction and clustering of silica nanoparticles in aqueous solution. *Phys. Rev. E*. **87**, 1–8 (2013).

105. P. Richetti, P. Kékicheff, Direct Measurement of Depletion and Structural Forces in a Micellar System. *Phys. Rev. Lett.* **68**, 1951–1954 (1992).

106. D. Ray, V. K. Aswal, Observation of adsorption versus depletion interaction for charged silica nanoparticles in the presence of non-ionic surfactant. *J. Phys. Condens. Matter*. **26**, 035102 (2014).

107. J. R. Savage, D. W. Blair, a J. Levine, R. a Guyer, a D. Dinsmore, Imaging the sublimation dynamics of colloidal crystallites. *Science (80-.)*. **314**, 795–798 (2006).

108. D. Sober, Measurement of long range depletion energies between a colloidal particle and a flat surface in micellar solutions. *Langmuir*, 2352–2356 (1995).

109. S. Srivastava, D. Nykypanchuk, M. M. Maye, A. V. Tkachenko, O. Gang, Super-compressible DNA nanoparticle lattices. *Soft Matter*. **9**, 10452 (2013).

110. C. J. Kiely, J. Fink, M. Brust, D. Bethell, D. J. Schiffrin, Spontaneous ordering of bimodal ensembles of nanoscopic gold clusters. *Nature*. **396**, 444–446 (1998).

111. M. I. Bodnarchuk, M. V. Kovalenko, W. Heiss, D. V. Talapin, Energetic and entropic contributions to self-assembly of binary nanocrystal superlattices: Temperature as the structure-directing factor. *J. Am. Chem. Soc.* **132**, 11967–11977 (2010).

112. R. T. Scarlett, M. T. Ung, J. C. Crocker, T. Sinno, A mechanistic view of binary colloidal superlattice formation using DNA-directed interactions. *Soft Matter*. **7**, 1912 (2011).

113. Y. Zhang *et al.*, Selective transformations between nanoparticle superlattices via the reprogramming of DNA-mediated interactions. *Nat. Mater.* **14**, 840–847 (2015).

114. X. Zhang, R. Wang, G. Xue, Programming macro-materials from DNA-directed self-assembly. *Soft Matter*. **00**, 1–9 (2015).

115. M. E. Leunissen, D. Frenkel, Numerical study of DNA-functionalized microparticles and nanoparticles: Explicit pair potentials and their implications for phase behavior. *J. Chem. Phys.* **134**, 1–18 (2011).

116. S. Dhakal, K. L. Kohlstedt, G. C. Schatz, C. A. Mirkin, Growth Dynamics for DNA-Guided Nanoparticle Crystallization, 10948–10959 (2013).

117. T. Vo *et al.*, Stoichiometric control of DNA-grafted colloid, 1–6 (2015).

118. D. Frenkel, A. J. C. Ladd, New Monte Carlo method to compute the free energy of arbitrary solids. Application to the fcc and hcp phases of hard spheres. *J. Chem. Phys.* **81**, 3188–3193 (1984).

119. J. L. Aragones, C. Valeriani, C. Vega, Note: Free energy calculations for atomic solids through the Einstein crystal/molecule methodology using GROMACS and LAMMPS. *J. Chem. Phys.* **137**, 146101 (2012).

120. C. Vega, E. Sanz, J. L. F. Abascal, E. G. Noya, Determination of phase diagrams via computer simulation: methodology and applications to water, electrolytes and proteins. *J. Phys. Condens. Matter*. **20**, 153101 (2008).

121. I. C. Jenkins, M. T. Casey, J. T. McGinley, J. C. Crocker, T. Sinno, Hydrodynamics selects the pathway for displacive transformations in DNA-linked colloidal crystallites. *Proc. Natl. Acad. Sci.* **111**, 4803–4808 (2014).

122. P. R. Ten Wolde, M. J. Ruiz-Montero, D. Frenkel, Numerical evidence for bcc ordering at the surface of a critical fcc nucleus. *Phys. Rev. Lett.* **75**, 2714–2717 (1995).

123. P. Rein ten Wolde, M. J. Ruiz-Montero, D. Frenkel, Numerical calculation of the rate of crystal nucleation in a Lennard-Jones system at moderate undercooling. *J. Chem. Phys.* **104**, 9932 (1996).

124. H. R. Braig *et al.*, Correction for Kirkness et al., Genome sequences of the human body louse and its primary endosymbiont provide insights into the permanent parasitic lifestyle. *Proc. Natl. Acad. Sci.* **108**, 6335–6335 (2011).

125. E. Auyeung *et al.*, DNA-mediated nanoparticle crystallization into Wulff polyhedra. *Nature*. **505**, 73–7 (2014).

126. Y. Peng *et al.*, Two-step nucleation mechanism in solid–solid phase transitions. *Nat. Mater.* **14**, 101–108 (2014).

127. A. Jain, J. R. Errington, T. M. Truskett, Dimensionality and design of isotropic interactions that stabilize honeycomb, square, simple cubic, and diamond lattices. *Phys. Rev. X*. **4**, 31049 (2014).

128. A. Stukowski, Structure identification methods for atomistic simulations of crystalline materials. *Model. Simul. Mater. Sci. Eng.* **20**, 45021 (2012).

129. H. S. Sözüer, J. W. Haus, Photonic bands: simple-cubic lattice. *J. Opt. Soc. Am. B*. **10**, 296 (1993).

130. K. M. Ho, C. T. Chan, C. M. Soukoulis, Existence of a Photonic Gap in Periodic Dielectric Structures. *Phys. Rev. Lett.* **65**, 3152 (1990).

131. A. M. Kalsin, Electrostatic Self-Assembly of Binary Nanoparticle Crystals with a Diamond-Like Lattice. *Science (80-.).* **312**, 420–424 (2006).

132. X. Cheng, J. H. McCoy, J. N. Israelachvili, I. Cohen, Imaging the microscopic structure of shear thinning and thickening colloidal suspensions. *Science (80-.).* **333**, 1276–9 (2011).

133. T. Muangnapoh, A. L. Weldon, J. F. Gilchrist, Enhanced colloidal monolayer assembly via vibration-assisted convective deposition. *Appl. Phys. Lett.* **103**, 181603 (2013).

134. X. Cheng, X. Xu, S. a Rice, A. R. Dinner, I. Cohen, Assembly of vorticity-aligned hard-sphere colloidal strings in a simple shear flow. *Proc. Natl. Acad. Sci. U. S. A.* **109**, 63–7 (2012).

135. S. Majumdar, R. Krishnaswamy, A. K. Sood, Discontinuous shear thickening in confined dilute carbon nanotube suspensions. *Proc. Natl. Acad. Sci. U. S. A.* **108**, 8996–9001 (2011).

136. M. E. Helgeson, M. D. Reichert, Y. T. Hu, N. J. Wagner, Relating shear banding, structure, and phase behavior in wormlike micellar solutions. *Soft Matter*. **5**, 3858 (2009).

137. A. Chremos, P. M. Chaikin, R. a. Register, A. Z. Panagiotopoulos, Shear-induced alignment of lamellae in thin films of diblock copolymers. *Soft Matter*. **8**, 7803 (2012).

138. L. B. Chen, B. J. Ackerson, C. F. Zukoski, Rheological consequences of microstructural transitions in colloidal crystals. *J. Rheol. (N. Y. N. Y).* **38**, 193 (1994).

139. B. Ackerson, N. Clark, Shear-induced melting. *Phys. Rev. Lett.* **46**, 123 (1981).

140. K. Jo, Y.-L. Chen, J. J. de Pablo, D. C. Schwartz, Elongation and migration of single DNA molecules in microchannels using oscillatory shear flows. *Lab Chip*. **9**, 2348–55 (2009).

141. Y.-L. Chen *et al.*, Conformation and dynamics of single DNA molecules in parallel-plate slit microchannels. *Phys. Rev. E*. **70**, 060901 (2004).

142. G. Petekidis, a. Moussaïd, P. Pusey, Rearrangements in hard-sphere glasses under

oscillatory shear strain. *Phys. Rev. E*. **66**, 051402 (2002).

143. O. Pouliquen, M. Nicolas, P. Weidman, Crystallization of non-Brownian Spheres under Horizontal Shaking. *Phys. Rev. Lett.* **79**, 3640–3643 (1997).

Appendix

Attached, for reference, is a published paper reflecting early work from my Ph.D. that is unrelated to the work described here.

Molecular Physics, 2014
http://dx.doi.org/10.1080/00268976.2014.903578

Taylor & Francis
Taylor & Francis Group

RESEARCH ARTICLE

Effect of molecular structure on fluid transport through carbon nanotubes

Minseok Song, Mark A. Snyder* and Jeetain Mittal*

Department of Chemical Engineering, Lehigh University, Bethlehem, PA, USA

(*Received 28 January 2014; accepted 3 March 2014*)

We perform molecular dynamics simulations to study the transport of geometrically modified water models through channels of carbon nanotube (CNT) membranes. We use two modifications to an existing water model (extended simple point charge SPC/E) as representative surrogates of molecular fluids: (1) bent model (model B) in which the HOH angle is varied while keeping the dipole moment constant by adjusting the OH bond length and (2) modified bent model (model MB) in which the HOH angle changes without any change in OH bond length thereby changing the dipole moment. Interestingly, we find that the fluid transport is a nonmonotonic function of the bond angle for both fluid models. This observed trend is not anticipated based on the fluid density as a function of the bond angle inside and outside of the nanotube channel. However, the average residence time of transmitted molecules through the channel provides an approximately inverse linear correlation with the observed flux, independent of the fluid model. Based on these correlations, we have developed an empirical design parameter connecting fluid transport through CNTs as a function of average occupancy (number of fluid molecules inside the nanotube) and the average residence time. Our results suggest that transport through carbon nanotubes can be sensitive to small changes in the structure of fluid molecules that can potentially be utilised for mixture separation.

Keywords: nanoscale transport; confined water; molecular simulation

1. Introduction

Fluid transport across carbon nanotube (CNT) membranes has received significant scientific interest due to unexpectedly high flux [1] and the potential applications [2–10] that can result from it such as water desalination and purification, nanofiltration, and gas separation. It was first reported that water can spontaneously fill and remain within the hydrophobic channel of a small diameter (0.6 nm) CNT for simulated periods as long as 66 ns [1]. The identification of the greatly enhanced fluid transport through nonpolar and nanosized CNTs relative to macroscopic expectations has led to significant effort to identify mechanistic aspects of such enhancement. A subsequent study attributed the rapid water transport to molecular ordering within a 0.8-nm diameter CNT channel under the influence of an osmotic gradient [6]. In addition to chain-like water structuring, the unusually low friction of the nanotube surface is believed to enable this fast transport [11–13].

Experimental validation of these predictions was first achieved by Hinds *et al.* through fabrication of a membrane consisting of aligned multiwall CNTs with large pore diameter (7 nm) spanning a polymer thin film [14]. Laboratory water permeation measurements confirmed that the flow rate through these membranes exceeded the predictions of macroscopic hydrodynamics by 4–5 orders of magnitude [15]. Membranes with sub 2-nm diameter CNTs were first made by Holt *et al.*, and both fluid and gas flow were found to be enhanced (by several orders of magnitude) relative to the predictions of classical hydrodynamics and Knudsen diffusion, respectively [16]. These laboratory demonstrations of fast fluid transport through membranes comprised of nanosized CNTs underscore the potential for high-permeability membrane applications.

In addition, water flow through CNTs can be employed as a simplified model to probe transport properties of biological and nanoscopic channels [17–19]. Namely, various studies have modified the CNT atoms to explore the sensitivity of water transport to changes in the nanotube polarity [20], nanotube–water interaction parameter [21,22], nanotube flexibility [23], and lattice structure. Sholl and co-workers previously employed various fluid molecules, such as Ar, Ne, H_2, CH_4, and their mixtures, to understand their transport behaviour through single-walled carbon nanotubes [24–26]. However, there is limited understanding of fluid transport through nanotubes and sensitivity of flow to molecular structure. While the continuum theory formalism is independent of the specific nature of the molecular structure of the fluid, it is essential for microscopic theories to account for the dependence of transport on this geometric structure [27].

As an example, Lynden-Bell and co-workers have used modified water models to better understand water behaviour

*Corresponding authors. Email: jeetain@lehigh.edu, snyder@lehigh.edu

and its solvation properties [28–31]. Specifically, by altering atomic charges, Lennard-Jones (LJ) contribution to intermolecular potential, and geometric structure, various modified water-like fluid models have been defined with systematic perturbations of the extended simple point charge (SPC/E) model. Bergman and Lynden-Bell used two types of modified water models, one in which the electrostatic interactions are modified and another in which the molecular geometry is altered, to understand the hydrophobic effect [28]. These modifications caused changes in the number and strength of hydrogen bonding and network structure in comparison to the SPC/E water model. Through the comparison among modified water models, it was found that the hydrophobic effect was closely related to hydrogen bonding and other strong intermolecular interactions, and did not depend on the presence of a three-dimensional network.

Subsequently, Lynden-Bell and Head-Gordon also used modified water models to understand solvation of apolar solutes [29]. In this study, they defined two types of models in order to separate the effects of hydrogen bonds and the local structure. The first was called the hybrid model for which the strength of hydrogen bonds can be controlled depending on the relative strength of the Coulombic and dispersive contributions to the pair potential. The second was called the bent model in which the HOH angle in the SPC/E water model was altered. The resulting molecules in a fluid were found to still form strong hydrogen bonds but to lack a local tetrahedral network, so the observed properties can be used to understand the role of fluid network structure. It was found that as the dispersive contribution increases in the hybrid models, the structure of the liquid becomes more close packed, and, thus, hydrophobic solutes cannot move inside liquid structure easily. However, the reduced structuring for bent models allowed the solute particles to penetrate easily. This study showed that the spatial correlations of the liquid are a better indicator than energetics of the solvation properties of a given liquid.

Recent work by Chatterjee *et al.* has used a broader range of bent models in which the HOH angle was varied from 60° to 120° to study the thermodynamics, translational dynamics, liquid structure, and solvation thermodynamics of apolar solutes [31]. It was shown that the liquid structure transitions from chain-like arrangement to water-like tetrahedral arrangement as HOH bond angle increases. A decrease in translation mobility with increasing HOH angle was reported to result from the monotonic increase in density and concomitant increase in tetrahedral structural order. Such models can be very helpful in elucidating a molecular understanding of fluid flow through CNTs.

In this paper, we investigate fluid transport through carbon nanotubes by using various modified water models to probe the effect of molecular structure. The modified water models used in this study are termed the B model and MB model. In both models, the HOH bond angle is varied, with differences between models deriving from their specific treatment of the OH bond length. Namely, the OH bond lengths in the B model are chosen so that the molecular dipole moment does not change, whereas in the MB model the OH bond length is fixed according to the SPC/E model, and increases with decreasing bond angle. First, we present our simulation data on fluid permeation through carbon nanotube membranes for both models; faster transport than that observed for the SPC/E water model and nonmonotonic fluid flux as a function of bond angle is observed. Insight into the nonmonotonic trend in fluid flux is achieved through investigation of density profiles inside and outside the CNT membrane. Finally, we assess how well this data is captured by our previously proposed correlation [21] between water flux through CNTs and an equilibrium-derived measure of water occupancy in CNT channels normalised by the average residence time.

2. Simulation model and methods

All of the simulations are performed using the molecular simulation package NAMD [32] for 15 ns after an initial equilibration period of 200 ps. Periodic boundary conditions are used in all directions as in our previous study [21]. We use 12 hexagonally packed armchair type (9,9) CNTs each of length 13.4 Å as shown in Figure 1. Preliminary investigations on (6,6) and (12,12) CNTs revealed qualitatively similar results as (9,9) CNT (see Supplementary Information (SI) Figure S3). Therefore, in this paper we only focus on (9,9) CNT results. The nanotubes and the carbon atoms are allowed to move during the simulation (as dictated by bonded and nonbonded interaction potentials). We find that the membrane structure is maintained during the whole simulation. The well depth of the Lennard-Jones (LJ) potential between CNT atoms and modified water molecules, $\epsilon_{\text{NT-OW}}$, is fixed at 0.115 kcal/mol and a characteristic distance of 3.283 Å is used [3]. All the simulations are carried out at a temperature of 300 K and pressure of 1 atm. A Langevin thermostat with a damping coefficient of 0.5 ps^{-1} is used to maintain constant temperature and a Langevin piston method is applied to maintain constant pressure that allows independent adjustment of all dimensions of the periodic cell [33]. For long-range electrostatic interactions, we use the particle mesh Ewald method [34]. For short-range LJ interactions, we use a 12 Å cutoff distance with a smoothing function applied at a 9 Å distance. The neighbour lists are maintained for each particle with radii 14 Å, and a rebuilding frequency of 10 steps is used.

The SPC/E water model [35] is used as a reference fluid (for comparison) and modifications to HOH bond angle are made to change molecular structure. Figure 1(b) and 1(c) shows representative snapshots for these modified water models. In the case of the bent model (B model), the HOH bond angle is systematically varied from 45° to 120° (B45–B120) while varying the OH bond length to keep the dipole

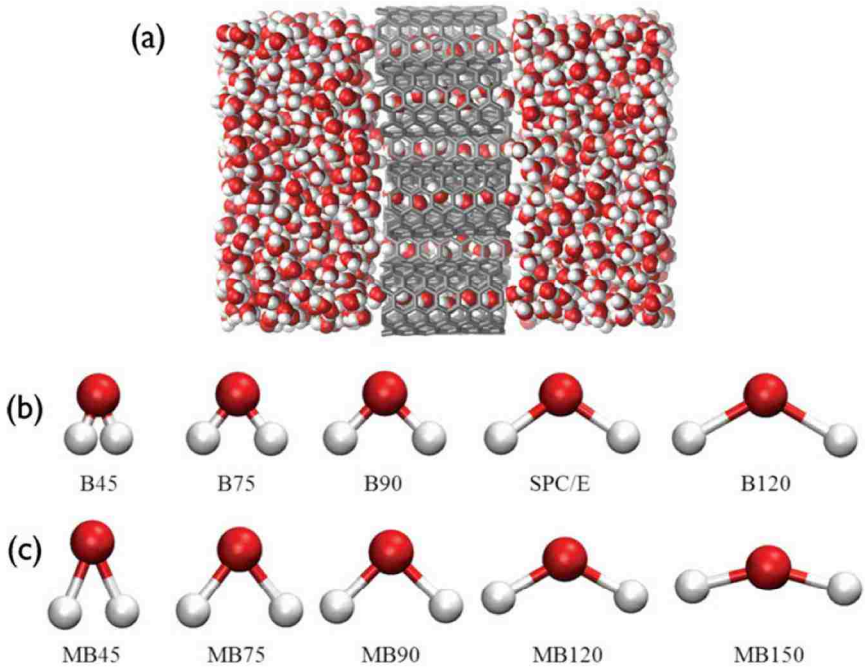

Figure 1. Simulation set-up and models. (a) The representative structures for the bent model (B model) with constant dipole moment. (b) The representative structure for the modified bent model (MB model) with constant bond length.

moment constant as shown in Figure 1(b). For the modified bent model (MB model), bond angle adjustment with a fixed bond length changes the dipole moment as shown in Figure 1(c).

3. Results and discussion

To gain insight into how molecular structure influences permeation through CNT membranes, we have simulated equilibrium flow of water-like fluids with both B and MB models (see Figure 1).

We define fluid flux (or permeation events) to be the total number of molecules permeating across the membrane per nanosecond normalised by the total number of CNTs in the membrane (12 in this case). Here, one permeation event is defined as a fluid molecule entering either end of the CNT and leaving from the opposite side. The fluid molecules that enter and leave through the same side of the CNT are not counted toward permeation. Figure 2 shows that the geometry of the fluid molecules can significantly influence their permeation through CNTs. Namely, Figure 2(a) shows that the fluid flux for the B model relative to that for the SPC/E water model varies nonmonotonically as a function of HOH bond angle. With decreasing HOH bond angle from SPC/E (109.5°) to B100 (100°), the observed permeation events increase sharply. A maximum in permeation is observed for an HOH bond angle of 90°, which is followed by a more gradual decay in permeation with further decrease in the bond angle. We do not observe any permeation events for fluids with HOH bond angles greater than 112.5°. This lack of permeation is consistent with previously observed bulk fluid behaviour showing a pronounced dynamical slowdown of diffusivity with increasing bond angle due to higher fluid density and increased structural order at 1 atm pressure [31].

Figure 2(b) shows that the fluid flux for the MB model also varies nonmonotonically as a function of HOH bond angle. In this case, where OH bond length is fixed and thus dipole moment varies, lower flux is observed for small bond angles, with a minimum flux observed for a bond angle of 75° in contrast to the B model. In the case of the MB model, permeation decreases with respect to SPC/E water with decreasing HOH angle, and increases for HOH angles above the SPC/E angle of 109.5°.

In order to understand this permeation behaviour for the modified water models, especially the nonmonotonic fluid flux dependence as a function of bond angle, we calculate the change in fluid density with bond angle at 300 K and 1 atm. Figure 3 shows the average density inside (open symbols) and outside (closed symbols) of the CNTs as a function of HOH bond angle for both B and MB models. While the fluid density is suppressed relative to the bulk

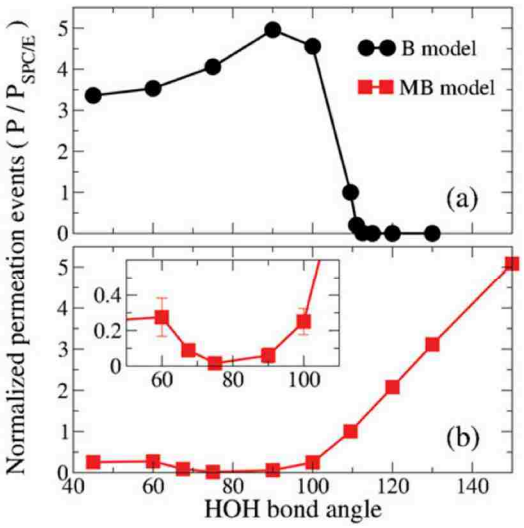

Figure 2. Permeation events for various modified water models normalised to the value for SPC/E water model ($P_{SPC/E}$). (a) The permeation events for the bent models (B) with constant dipole moments. (b) The permeation events for the modified bent models (MB) with constant bond lengths. The inset shows the magnified view to highlight nonmonotonic dependence. Standard deviations based on data from 12 nanotubes are also shown, and in most cases are smaller than the symbol size.

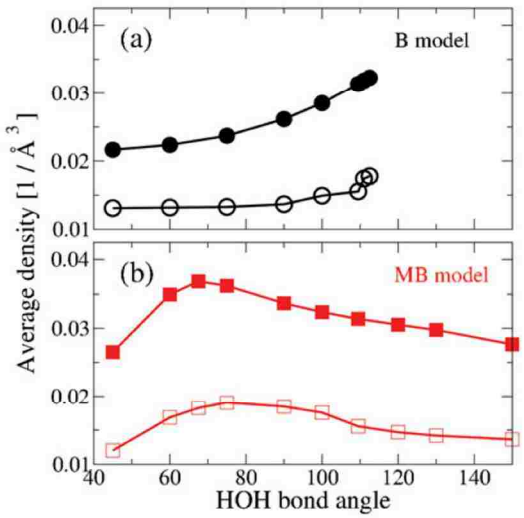

Figure 3. Average bulk (solid symbols) and CNT-confined (open symbols) fluid density as a function of HOH bond angle for various modified water models. Fluid density, which is qualitatively comparable between bulk and CNT-confined states, varies with HOH bond angle (a) monotonically for the bent (B) models and (b) nonmonotonically for the modified bent (MB) models.

by confinement within the CNTs, we find that the change in density as a function of HOH bond angle shows qualitatively similar trends inside and outside the CNT for a given fluid model. Therefore, beyond a subtle shift in the maximum density to higher HOH bond angles for the MB model under CNT confinement, the density of fluid confined within a CNT does not appear to dramatically deviate from the observed trend in bulk density (in this case outside the CNT is considered bulk) at constant pressure. Interestingly, the density changes monotonically in the case of the B model (Figure 3(a)) whereas a nonmonotonic density change with HOH bond angle is observed for the MB model (Figure 3(b)). While the nonmonotonic change in fluid flux in the case of the MB model at bond angles around 75° (Figure 2(b)) may be attributed, at least in part, to the corresponding maximum in fluid density at these bond angles, it is clear that the density alone cannot explain the observed behaviour. Specifically, very different fluid flux is observed for fluid models with similar average density in the case of the MB model (e.g., MB45 versus MB150). Also, nonmonotonic flux for the B model is not captured by the average density.

To assess if local structuring inside the CNTs may help explain some of these trends (see SI Figure S2 for simulation snapshots), we also calculate local density profiles in both axial and radial directions. Figure 4 shows density profiles for B (panels (a) and (c)) and MB models (panels (b) and (d)) as a function of axial (Z) or radial distance. For axial density profiles, $|Z| < 6.7$ Å corresponds to fluid within the CNT, while $|Z| > 6.7$ Å refers to bulk fluid outside of the CNT. According to the axial density profiles in Figure 4(a), the fluid density for the B model increases as the HOH bond angle increases as expected from the average density (Figure 3(a)). For HOH bond angles of 111° and larger, the fluid inside the CNT is quite structured as seen from the large periodic variations in the density profile. As shown in SI Figure S1, we do not observe complete nanotube filling for models B120 and B130 during the entire simulation time. This significant slowdown in diffusion for these models is related to the fluid–solid transition. Several previous studies have provided detailed information on freezing of water inside carbon nanotubes as a function of temperature and pressure [36–39]. The corresponding fluid flux is negligible for these nanotube-confined frozen molecules over the 15 ns simulated time.

Figure 4(b) shows the axial density profiles in the case of the MB model. Here, the changes in the HOH bond angle are also accompanied by changes in the dipole moment of the fluid. Unlike the B model, MB fluids confined within CNTs show a maximum in density for a bond angle of 75°, while a decrease in density with both increasing and decreasing bond angle corresponds to the observed enhancement in fluid flux (Figure 2(b)). In this MB model, fluid structuring (periodic density profile) is observed for intermediate HOH bond angles (60° –100°) for which permeation is very low

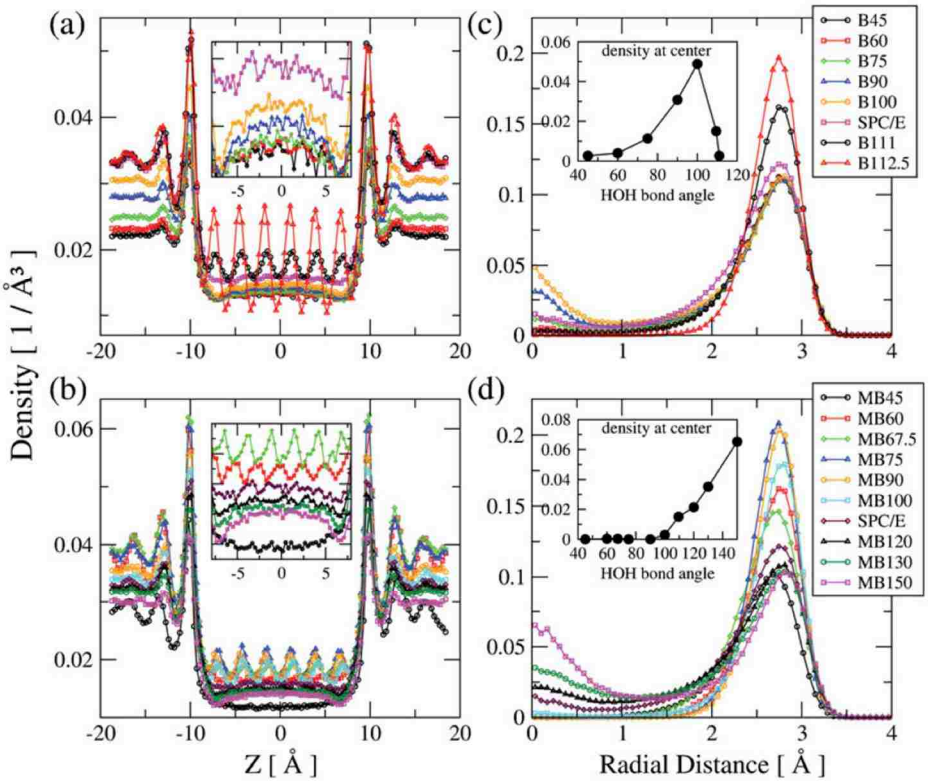

Figure 4. Axial (a, b) and radial (c, d) density of modified water molecules. Axial density for (a) B series and (b) MB series inside (−6.7 to 6.7 Å) and outside CNT (−20 to −6.7 and 6.7–20 Å) as a function of HOH bond angle. Insets in (a) and (b) show magnified views of axial density profiles within the CNT. Radial density for (c) B series and (d) MB series molecules inside CNTs of 6.1 Å radius. Insets in (c) and (d) show density at the centre of the CNT as a function of HOH bond angle.

or negligible. However, while MB45 has the lowest average density among all cases, it does not have the highest permeation. In that case, the dipole moment is the highest, and, therefore, this suggests that the dipole moment, in addition to molecular geometry, can play an important role in fluid transport within CNTs.

Figure 4(c) and 4(d) show the sensitivity of radial density profiles to the HOH bond angle for both B and MB models, respectively. For the B model, HOH bond angles greater than that of the SPC/E water results in the localisation of molecules closer to the nanotube walls. As HOH bond angle is decreased below that of the SPC/E water, radial density near the walls is maintained while the density at the nanotube centre increases. A similar influence of HOH bond angle on radial density is also observed for the MB model (Figure 4(d)). Interestingly, the modified models with fluid molecules located at the centre of the nanotube show higher permeation. This may be due to the fact that water molecules transmitting through the centre take less time on average, or more water molecules can transmit through the channel with similar average residence time. However, the maximum in radial density at the nanotube centre does not correspond to the maximum in fluid flux in terms of the HOH bond angle for the B model.

The above analysis of the density profiles reveals that fluid permeation through CNTs does not have a simple dependence on density. This is unlike bulk fluid density for which fluid mobility correlates directly with density [31]. The observed behaviour appears instead to be a combination of several factors including, but not limited to, average density, local structuring inside the nanotube, and fluid dipole moment.

In our previous work, we have shown that water flux through nanotubes is related to the average occupancy of the nanotube channel and the average residence time of the molecules permeated [21]. Figure 5(a) first assesses the relationship between average number of molecules inside the CNT and permeation events. The average number of molecules (as expected based on fluid density) varies non-monotonically with permeation events for both B and MB

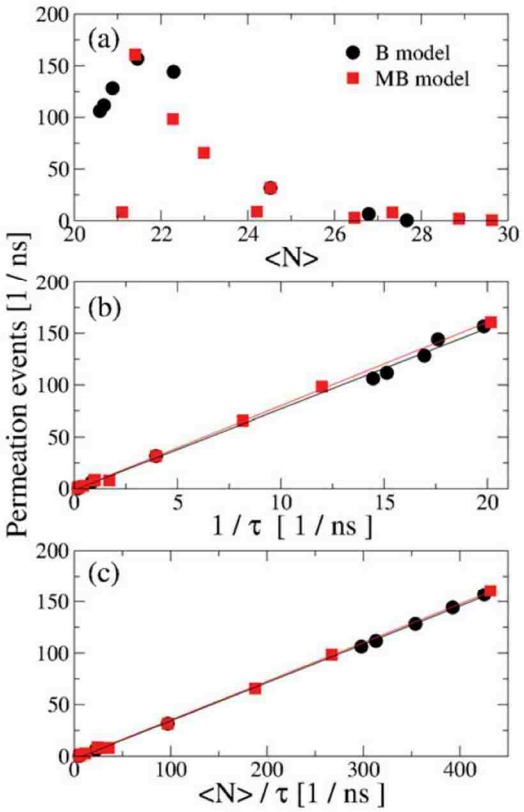

Figure 5. (a) Average number of modified water molecules occupying a nanotube, $\langle N \rangle$, versus permeation events. (b) Inverse average residence time, $1/\tau$, versus permeation events. (c) $\langle N \rangle/\tau$ versus permeation events for various modified water models; B series and MB series.

models. The highest permeation is observed for an average occupancy of about 21.4 fluid molecules irrespective of the type of modified water model (B or MB); B90 and MB150 have average occupancy of 21.45 and 21.40, respectively. Below and above this average occupancy level, the permeation events start to decrease gradually.

Next, we turn our attention to the average residence time of molecules that permeate through the CNT membrane. Figure 5(b) shows permeation events versus inverse residence time and an approximately linear proportionality is observed for both B and MB models. This suggests that the primary effect of HOH bond angle on fluid transport through CNTs is exerted by modulating the residence time. In our previous study, we had found it necessary to consider both the average occupancy and inverse residence time to account for water flux through nanotubes with varying water-nanotube attraction strengths. As shown in Figure 5(c), accounting for both of these factors indeed improves the correlation and captures the observed permeation behaviour for all the cases. This means that fluid models with an average occupancy of more than $\approx$ 21 molecules have higher residence time due to high fluid density inside the nanotube, and, therefore, lower flux dominated by this term. On the other hand, below the average fluid occupancy of 21 molecules, the $\langle N \rangle$ term is also important together with the residence time. What is most striking is that this simple correlation is capable of capturing predicted transport properties for a range of disparate molecular fluids based upon equilibrium measures. As such, it provides a potential design rule for empirical studies aimed at harnessing CNT-mediated transport of molecular fluids of a range of characteristic molecular geometries.

4. Conclusions

In an effort to probe flow of nonaqueous fluids through CNTs via simulations, we have employed bond-angle and dipole moment modifications of two existing water models as representative surrogates for a range of molecular fluids. Permeation simulations were carried out for modified water models in which HOH bond angle is systematically varied while either (1) allowing OH bond length to vary in order to maintain an SPC/E dipole moment or (2) holding OH bond length fixed to study the role of changing dipole moment. Dramatic and nonmonotonic changes in permeation flux relative to SPC/E water through a model CNT-based membrane were observed as HOH bond angle was varied. Unlike bulk fluid behaviour, however, the nonmonotonic flux could not be simply linked to fluid density variations within the nanotube despite qualitative agreement in the trends of fluid density in the bulk and under CNT confinement. Rather, we show that the fluid behaviour under CNT confinement seems to be sensitive to numerous factors including, at least in part, average density within the CNT, local structuring, and the fluid dipole moment. Despite the variations in permeation among the modified water models and across bond angles studied, we identify a simple design rule suggesting that permeation flux can be linearly correlated with equilibrium measures of average CNT occupancy normalised by average residence behaviour at the molecular level. We tried to verify the relationship between flux and molecular structure by using two types of modified water models. B-type showed that the fluid structure varied from chain-like to a tetrahedral network with increasing H–O–H angle. Also, MB-type showed that dipole moment increased as bond angle decreased. Based on these results, not only interaction between fluids and CNTs, but also intermolecular interaction among fluids as well as fluid molecular structure inside the nanotubes play an important role in modulating permeation. Thus, proper control for these variables could produce the fastest permeation events. The simple design

parameter linking flow properties within specific nanotubes with fluid occupancy and residence time showed linear correlation between permeation and $\langle N \rangle$.

Funding

This work was supported by the National Science Foundation [grant number CBET-1120399]; use of the high-performance computing capabilities of the Extreme Science and Engineering Discovery Environment (XSEDE), which is supported by the National Science Foundation (J.M.) [grant no. MCB-120014].

Supplemental data

Supplemental data for this article can be accessed here.

References

[1] G. Hummer, J. Rasaiah, and J. Noworyta, Nature **414**, 188 (2001).
[2] J. Rasaiah, S. Garde, and G. Hummer, Annu. Rev. Phys. Chem. **59**, 713 (2007).
[3] A. Alexiadis and S. Kassinos, Chem. Rev. **108**, 5014 (2008).
[4] A. Noy, H. Park, F. Fornasiero, J. Holt, C. Grigoropoulos, and O. Bakajin, Nano Today **2**, 22 (2007).
[5] M. Whitby and N. Quirke, Nat. Nano. **2**, 87 (2007).
[6] A. Kalra, S. Garde, and G. Hummer, Proc. Natl. Acad. Sci. U.S.A. **100**, 10175 (2003).
[7] F. Fornasiero, H. Park, J. Holt, M. Stadermann, C. Grigoropoulos, A. Noy, and O. Bakajin, Proc. Natl. Acad. Sci. U.S.A. **105**, 17250 (2008).
[8] B. Corry, J. Phys. Chem. B **112**, 1427 (2008).
[9] M. Yu, H.H. Funke, J.L. Falconer, and R.D. Noble, J. Am. Chem. Soc. **132**, 8285 (2010).
[10] J. Lee and N. Aluru, Appl. Phys. Lett. **96**, 133108 (2010).
[11] A. Striolo, Nano Lett. **6**, 633 (2006).
[12] S. Joseph and N. Aluru, Nano Lett. **8**, 452 (2008).
[13] K. Falk, F. Sedlmeier, L. Joly, R.R. Netz, and L. Bocquet, Nano Lett. **10**, 4067 (2010).
[14] B. Hinds, N. Chopra, T. Rantell, R. Andrews, V. Gavalas, and L. Bachas, Science **303**, 62 (2004).
[15] M. Majumder, N. Chopra, R. Andrews, and B. Hinds, Nature **438**, 44 (2005).
[16] J. Holt, H. Park, Y. Wang, and M. Stadermann, Science **132**, 1034 (2006).
[17] F. Zhu and K. Schulten, Biophys. J. **85**, 236 (2003).
[18] B. Liu, X. Li, B. Li, B. Xu, and Y. Zhao, Nano Lett. **9**, 1386 (2009).
[19] C.-J. Tsai, J. Zheng, and R. Nussinov, PLoS Comput. Biol. **2**, 311 (2006).
[20] G. Portella and B. de Groot, Biophys. J. **96**, 925 (2009).
[21] M. Melillo, F. Zhu, M.A. Snyder, and J. Mittal, J. Phys. Chem. Lett. **2**, 2978 (2011).
[22] T. Werder, J.H. Walther, R.L. Jaffe, T. Halicioglu, and P. Koumoutsakos, J. Phys. Chem. B **107**, 1345 (2003).
[23] S. Andreev, D. Reichman, and G. Hummer, J. Chem. Phys. **123**, 194502 (2005).
[24] H. Chen and D.S. Sholl, J. Am. Chem. Soc. **126**, 7778 (2004).
[25] S.K. Bhatia, H. Chen, and D.S. Sholl, Mol. Sim. **31**, 643 (2005).
[26] D.M. Ackerman, A.I. Skoulidas, D.S. Sholl, and J. Karl Johnson, Mol. Simulation **29**, 677 (2003).
[27] J. Thomas and A. McGaughey, Phys. Rev. Lett. **102**, 184502 (2009).
[28] D.L. Bergman and R. Lynden-Bell, Mol. Phys. **99**, 1011 (2001).
[29] R.M. Lynden-Bell and T. Head-Gordon, Mol. Phys. **104**, 3593 (2006).
[30] J. Alejandre and R.M. Lynden-Bell, Mol. Phys. **23**, 3029 (2007).
[31] S. Chatterjee, P.G. Debenedetti, F.H. Stillinger, and R.M. Lynden-Bell, J. Chem. Phys. **128**, 124511 (2008).
[32] J. Phillips, R. Braun, W. Wang, J. Gumbart, E. Tajkhorshid, E. Villa, C. Chipot, R. Skeel, L. Kale, and K. Schulten, J. Comput. Chem. **26**, 1781 (2005).
[33] S.E. Feller, Y. Zhang, R.W. Pastor, and B.R. Brooks, J. Chem. Phys. **103**, 4613 (1995).
[34] U. Essmann, L. Perera, M. Berkowitz, T. Darden, H. Lee, and L. Pedersen, J. Chem. Phys. **103**, 8577 (1995).
[35] H.J.C. Berendsen, J.R. Grigera, and T.P. Straatsma, J. Phys. Chem. **91**, 6269 (1987).
[36] K. Koga, G. Gao, H. Tanaka, and X.C. Zeng, Physica A **314**, 462 (2002).
[37] R.J. Mashl, S. Joseph, N. Aluru, and E. Jakobsson, Nano Lett. **3**, 589 (2003).
[38] D. Takaiwa, I. Hatano, K. Koga, and H. Tanaka, Proc. Natl. Acad. Sci. U.S.A. **105**, 39 (2008).
[39] M. Sliwinska-Bartkowiak, M. Jazdzewska, L. Huang, and K. Gubbins, Phys. Chem. Chem. Phys. **10**, 4909 (2008).

VITAE

SONG, MINSEOK

EDUCATION AND WORK EXPERIENCE

- **Lehigh University, Bethlehem, Pennsylvania** Aug. 2011 – present
  Ph.D., Department of Chemical and Biomolecular Engineering
  Advisor: Prof. Jeetain Mittal and Prof. Mark A. Snyder
  Thesis: Self-Assembly of DNA-coated Particles: Experiment, Simulation and Theory
- **LG Hausys, Ltd., Anyang, Gyeonggi-do, South Korea** Apr. 2009 – Jul. 2011
  Research Scientist, R&D Center
- **LG Chem, Ltd., Daejeon, South Korea** Jan. 2005 – Mar. 2009
  Research Scientist, Research Park
- **POSTECH, Pohang, Gyeongsangbuk-do, South Korea** Mar. 2003 – Jan. 2005
  M.S., Department of Chemical Engineering
  Advisor: Prof. Jin Kon Kim
  Thesis: Water-soluble Binder for Large Sized Injection Molded Articles
- **Pusan National University, Pusan, South Korea** Mar. 1996 – Feb. 2003
  B.S., Polymer Science & Engineering

PUBLICATION LISTS

1. **M. Song**, H. Zerze, Y. Ding, and J. Mittal, "Asymmetric design of DNA-mediated interparticle interactions in three dimensional lattice", in preparation
2. **M. Song**, Y. Ding, M. A. Snyder, and J. Mittal, "Two-Dimensional colloidal assembly using multiflavored DNA-functionalized microparticles", in preparation
3. Y. Ding*, **M. Song***, and J. Mittal, "Tuning DNA-mediated interparticle interaction to guide lattice selection", in preparation, *Equal contribution
4. **M. Song**, M. A. Snyder, and J. Mittal, "Effect of Nonionic Surfactant on Association/Dissociation Transition of DNA-functionalized Colloids", in preparation
5. **M. Song**, M. A. Snyder, and J. Mittal, "Effect of molecular structure on fluid transport through carbon nanotubes", *Mol. Phys*. **112**, 20, 2658-2664 (2014).
6. J. K. Kim, J. W. Kim, M. I. Kim, and **M. Song**, "Thermal Conductivity and Adhesion Properties of Thermally Conductive Pressure-Sensitive Adhesives", *Macromolecular Research*, **14**, 517-523 (2006)
7. **M. Song,** M. S. Park, and J. K. Kim. "Water-soluble binder with high flexural modulus for powder injection molding", *J. Mater. Sci*., **40**, 1105-1109 (2005)

SELECTED CONFERENCE PRESENTATION

1. **M. Song**, Y. Ding, M. A. Snyder, J. Mittal*, "Self-Assembly of Multiflavored DNA-Coated Particles: Experiment, Simulation, and Theory", 2015 AIChE Annual Meeting, November 8-13, 2015, Salt Lake City, UT (*Presenter)
2. **M. Song**, Y. Ding, M. A. Snyder, J. Mittal, "Experimental Investigation of DNA-mediated Assembly:, 2015 Emulsion Polymers Institute Industrial Liaison Program (Annual Review Meeting), May 5-6, 2015, Bethlehem, PA (*Oral presentation*)
3. **M. Song**, M. A. Snyder, J. Mittal, "Exploiting Tunable Association/Dissociation Transitions for Rational Control of DNA-mediated Particle Assembly", 2014 AIChE Annual Meeting, November 16-21, 2014, Atlanta, Georgia (*Oral presentation*)
4. **M. Song**, M. A. Snyder, J. Mittal, "The effect of PEO_{99}-PPO_{65}-PEO_{99} block copolymer on association/dissociation transitions of DNA-coated colloids", ACS 2014 Colloid & Surface Science Symposium, June 22-25, 2014, Philadelphia, Pennsylvania (*Oral presentation*)
5. **M. Song**, M. A. Snyder, J. Mittal, "Water transport through carbon nanotubes with modified water models", 2012 AIChE Annal Meeting, October 28-November 2, 2012, Pittsburgh, PA (*Oral presentation*)
6. **M. Song**, M. A. Snyder, J. Mittal, "Water transport through carbon nanotubes with modified water models", 244th ACS National Meeting & Exposition August 19-23, 2012, Philadelphia, Pennsylvania (*Oral presentation*)
7. **M. Song**, M.S. Park, I.B. Cho, H.J. Sung, S. Ahn, and J.K. Kim, "Water-soluble binder system controlled rheological properties in powder injection molding", Polymer Processing Society Asia/Australia Meeting, Gyeongju, Korea, p. 45, 2004082
8. **M. Song**, M.S. Park, I.B. Cho, H.J. Sung, S. Ahn, and J.K. Kim, "Water-soluble binder system controlled rheological properties in powder injection molding", The XIVth International Congress on Rheology, Seoul, Korea, p. 41, 200408

HONORS AND AWARDS

1. The Kenneth Earhart Award, Lehigh's Emulsion Polymers Institute (EPI) (2015)
2. The Excellence Prize in "Happy Change Contest", LG Hausys, Ltd (2009)
3. The Grand Prize of Research and Development, LG Hausys, Ltd. (2009)
4. The Best Colleague Prize, Functional Material Division, LG Hausys, Ltd. (2009)
5. The Best Colleague Prize, Living Solution Division, LG Chem, Ltd. (2008)
6. JeongAm Scholarship, JeongAm Scholarship Foundation. (2002)
7. Excellent Undergraduate Students Scholarship, Pusan National University. (2000, 2001)